

PVDF SENSOR BASED WIRELESS MONITORING OF MILLING PROCESS

A Dissertation
Presented to
The Academic Faculty

by

Lei Ma

In Partial Fulfillment
of the Requirements for the Degree
Doctor of Philosophy in the
School of Mechanical Engineering

Georgia Institute of Technology
May 2013

PVDF SENSOR BASED WIRELESS MONITORING OF MILLING PROCESS

Approved by:

Dr. Shreyes Melkote, Advisor
School of Mechanical Engineering
Georgia Institute of Technology

Dr. Steven Danyluk
School of Mechanical Engineering
Georgia Institute of Technology

Dr. Steven Liang
School of Mechanical Engineering
Georgia Institute of Technology

Dr. Jianjun (Jan) Shi
School of Industrial and System
Engineering
Georgia Institute of Technology

Dr. Henrik Christensen
Robotics and Intelligent Machines
Georgia Institute of Technology

Date Approved: February 4th, 2013

DEDICATION

To my parents:

Airong Yan

Yaozong Ma

To my wife:

Xiaoling Dong

ACKNOWLEDGMENTS

I would like to express my sincere gratitude to my advisor, Dr. Shreyes Melkote for being encouraging and patient with me in the past four years. My work could not have been finished without his guidance and support. Besides, I would like to extend my appreciation to all my committee members, Dr. Steven Danyluk, Dr. Steven Liang, Dr. Jan Shi and Dr. Henrik Christensen, for helping me improve the quality of my work. I would also like to thank my wife, my parents and all the other family members for supporting me and bearing with me in the past four years. Special thanks are also due to Mr. Anh Nguyen, Mr. Kyle French, Mr. Steven Sheffield, Mr. John Morehouse, Dr. James Castle, Dr. James Fonda and Mrs. Pamela Rountree for their help and/or contribution to this project. I would also like to thank all my friends, fellow students and labmates for making my stay at Georgia Tech more enjoyable. Last but not least, I would like to acknowledge the Boeing Company for funding this project.

TABLE OF CONTENTS

	Page
ACKNOWLEDGMENTS.....	iv
LIST OF TABLES.....	viii
LIST OF FIGURES.....	ix
NOMENCLATURE.....	xiv
SUMMARY.....	xvii
CHAPTER 1 INTRODUCTION.....	1
Motivation and Problem Statement.....	1
PVDF Sensor.....	3
Research Objectives.....	3
Proposed Approaches.....	4
Thesis Outline.....	5
CHAPTER 2 LITERATURE REVIEW.....	7
Wireless Machining Process Monitoring.....	7
PVDF Based Sensing Applications.....	8
Monitoring of Cutting Forces/Torque in Milling.....	9
On-line Recognition of Chatter in Milling: Sensors and Algorithms.....	10
Summary.....	15
CHAPTER 3 PVDF SENSOR BASED CUTTING FORCE MEASUREMENT.....	17
Introduction.....	17
Background.....	17

Force Measurement System Modeling.....	20
Experimental Verification.....	36
Summary.....	47
CHAPTER 4 DESIGN OF PVDF SENSOR ROSETTE FOR STRAIN ISOLATION...	50
Introduction.....	50
Modeling of PVDF Sensor Rosettes.....	50
Experimental Validation.....	71
Summary.....	76
CHAPTER 5 CHATTER DETECTION AND FREQUENCY ESTIMATION.....	78
Introduction.....	78
Methodology.....	79
Experiments and Results.....	101
Computational Complexity Analysis.....	113
Summary.....	116
CHAPTER 6 PVDF SENSOR BASED CUTTING TORQUE MEASUREMENT AND CHATTER DETECTION.....	117
Introduction.....	117
Theory and Approach.....	117
Experimental Validation.....	118
Characterization of Different Sensors for Chatter Detection.....	127
Chatter Experiments and Results.....	133
Summary.....	146
CHAPTER 7 CONCLUSIONS AND RECOMMENDATIONS.....	147
Original Contributions.....	147

Main Conclusions.....	147
Future Work and Recommendations.....	150
REFERENCES.....	152

LIST OF TABLES

	Page
Table 1. Cutting conditions for experimental tests for in-plane force measurement.....	37
Table 2. Estimation of K_s	39
Table 3. Computational complexity analysis of the proposed algorithm.	115
Table 4. Cutting conditions for cutting torque measurement.	123
Table 5. Cutting conditions for chatter test with PVDF sensor.	134

LIST OF FIGURES

	Page
Figure. 1. Overall approach to wireless milling process monitoring.....	5
Figure. 2. Force measurement system setup for peripheral end milling.	18
Figure. 3. Signal flow of the force measurement system.....	19
Figure. 4. Schematic of PVDF sensor deployment in peripheral end milling process.	21
Figure. 5. Frequency response function of the cutting tool/tool holder/spindle/machine tool system used in the study (see Figure. 2).	25
Figure. 6. Schematic of a PVDF sensor element.	28
Figure. 7. Angular span of the PVDF sensor on the cutting tool shank.	31
Figure. 8. Diagram for the signal conditioning circuit.....	33
Figure. 9. Bode plot of the transfer function of signal conditioning circuitry.	35
Figure. 10. Backward comparison between the reference signal and the in-situ measured PVDF sensor signal (Cutting Test No. 1).	40
Figure. 11. Backward comparison between the reference signal and the in-situ measured PVDF sensor signal (Cutting Test No. 10).	40
Figure. 12. Backward comparison between the reference signal and the in-situ measured PVDF sensor signal (Cutting Test No. 15).	41
Figure. 13. Backward comparison between the reference signal and the in-situ measured PVDF sensor signal (Cutting Test No. 17).	41
Figure. 14. Discrete time compensation of attenuation and distortion introduced by the signal conditioning circuitry.	43
Figure. 15. Forward comparison between the forces calculated from the PVDF sensor signals and the dynamometer measurements (Cutting Test No. 1: tool entry stage of cutting).	44
Figure. 16. Forward comparison between the forces calculated from the PVDF sensor signal and the dynamometer measurements (Cutting Test No. 1: stable cutting stage). ..	45

Figure. 17 Comparison of the Dynamometer Force (F_x) and PVDF Sensor Based Force (F_x) in Frequency Domain.....	47
Figure. 18. Schematic of a PVDF sensor element.	51
Figure. 19. PVDF sensor rosette for isolation of bending strain on a rectangular beam. .	56
Figure. 20. Two bending strain PVDF rosette configurations on a circular beam.	59
Figure. 21. PVDF sensor rosette for isolation of shear strain on a circular shaft.	61
Figure. 22. Mohr's strain circle for shear strain transformation.....	62
Figure. 23. PVDF sensor rosette for isolation of shear strain.	64
Figure. 24. PVDF sensor rosette for isolation of axial strain.....	65
Figure. 25. Schematic of an unbalanced Wheatstone full bridge.	66
Figure. 26. General purpose PVDF rosette configuration.	69
Figure. 27. Condition number of the coefficient matrix.	71
Figure. 28. Experimental setup for PVDF rosette and MFSG rosette.	72
Figure. 29. Bending strain rosette tests.	73
Figure. 30. Shear strain rosette tests.	74
Figure. 31. Axial strain rosette tests.....	74
Figure. 32. FFT of a bending rosette test result (corresponding to subplot1 in Figure 12).	75
Figure. 33. Chip regeneration in milling.....	80
Figure. 34. Ideal Differentiator and its finite order approximations.....	85
Figure. 35. Global trend and local variation in x_k	88
Figure. 36. Relationship between the pole location and the spectrum of the signal.....	100
Figure. 37. Flow chart of the chatter detection and chatter frequency estimation method.	101

Figure. 38. Inputs and outputs of the chatter detection algorithms for test 1 (a) (Cutting conditions: four flute 6.35mm carbide tool, 1018 steel workpiece, 3400 RPM, 0.0254 mm feed/tooth, 50% radial immersion, 2.54 mm depth of cut at beginning).	103
Figure. 39. Inputs and outputs of the chatter detection algorithms for test 1 (b).....	103
Figure. 40. Inputs and outputs of the chatter detection algorithms for test 2 (a) (two flute 25.4 mm carbide tool, 1018 steel workpiece, 1200 RPM, 0.0381mm feed/tooth, 25% radial immersion, 2.54 mm axial depth of cut).....	104
Figure. 41. Inputs and outputs of the chatter detection algorithms for test 2 (b).....	105
Figure. 42. Workpiece geometries and toolpaths for cutting tests 3 and 4.	106
Figure. 43. Inputs and outputs of the chatter detection algorithms for test 3 (a) (two flute 12.7mm carbide tool, aluminum 7050 workpiece, 2400 RPM, 50%-100% radial immersion, 2.54 mm axial depth of cut, 0.016 mm feed/tooth).	107
Figure. 44. Inputs and outputs of the chatter detection algorithms for test 3 (b).....	107
Figure. 45. Inputs and outputs of the chatter detection algorithms for test 4 (a) (two flute 12.7mm carbide tool, aluminum 7050 workpiece, 2400 RPM, 50%-100% radial immersion, 1.905 mm axial depth of cut, 0.0254 mm feed/tooth).....	108
Figure. 46. Inputs and outputs of the chatter detection algorithms for test 4 (b).....	108
Figure. 47. Workpiece geometry and toolpath for cutting test 5.	109
Figure. 48. Inputs and outputs of the chatter detection algorithms for test 5 (a) (four flute 6.35 mm High Speed Steel tool, aluminum 7050 workpiece, 2400 RPM, 50% radial immersion, 3.81 mm – 11.43 mm axial depth of cut, 0.0381 mm feed/tooth).	110
Figure. 49. Inputs and outputs of the chatter detection algorithms for test 5 (b).....	110
Figure. 50. Comparison of the FFT of $f(t)$ (top) and $F(t)$ (bottom).	112
Figure. 51. Dominant chatter frequency estimated by proposed algorithm (top) and FFT (bottom) (data is from test 1).	113
Figure. 52. Dominant chatter frequency estimated by proposed algorithm (top) and FFT (bottom) (data is from test 2).	113
Figure. 53. PVDF sensor based cutting torque measurement prototype.....	118
Figure. 54. Cutting forces in workpiece coordinate system and tool coordinate system.	119

Figure. 55. Backward comparison of PVDF sensor signal with reference signal (cutting conditions: two flute 25.4 mm carbide tool, Aluminum 7050 workpiece, 1500 RPM, 0.0254 mm feed/tooth, 50% radial immersion, 1.905 mm depth of cut).....	124
Figure. 56. Backward comparison of PVDF sensor signal with reference signal (cutting conditions: two flute 25.4 mm carbide tool, Aluminum 7050 workpiece, 1800 RPM, 0.0254 mm feed/tooth, 50% radial immersion, 1.905 mm depth of cut).....	125
Figure. 57. Backward comparison of PVDF sensor signal with reference signal (cutting conditions: two flute 25.4 mm carbide tool, Aluminum 7050 workpiece, 2100 RPM, 0.0254 mm feed/tooth, 50% radial immersion, 1.905 mm depth of cut).....	125
Figure. 58. Backward comparison of PVDF sensor signal with reference signal (cutting conditions: two flute 25.4 mm carbide tool, Aluminum 7050 workpiece, 1800 RPM, 0.0254 mm feed/tooth, 25% radial immersion, 2.540 mm depth of cut).....	126
Figure. 59. Backward comparison of PVDF sensor signal with reference signal (cutting conditions: two flute 25.4 mm carbide tool, 1018 Steel workpiece, 1200 RPM, 0.0254 mm feed/tooth, 25% radial immersion, 3.81 mm depth of cut).....	126
Figure. 60. Experimental set-up of the piezoelectric microphone.	128
Figure. 61. Schematic of the signal conditioning circuit for the microphone.....	128
Figure. 62. Frequency response function of the piezoelectric microphone [133].	129
Figure. 63. Experimental set-up of the piezoelectric dynamometer.	130
Figure. 64. Frequency Response Functions of the workpiece-mounted dynamometer in the X and Y directions.	131
Figure. 65. Experimental set-up of workpiece mounted accelerometers.....	132
Figure. 66. Frequency response functions of the workpiece-mounted accelerometer in the X and Y directions.	133
Figure. 67. Spurious peaks in the PVDF sensor torque signal.	135
Figure. 68. Frequency decomposition of the PVDF sensor signal (Test 1).....	136
Figure. 69. Frequency decomposition of the dynamometer force signal (Test1, force in X direction).....	137
Figure. 70. Frequency decomposition of the accelerometer signal (Test1, the acceleration in X direction).....	138
Figure. 71. Frequency decomposition of the microphone signal (Test1).	139

Figure. 72. Frequency decomposition of the PVDF sensor signal (Test 2).....	140
Figure. 73. Frequency decomposition of the dynamometer force signal (Test 2, the force in X direction).....	141
Figure. 74. Frequency decomposition of the accelerometer signal (Test 2, the acceleration in the X direction).....	142
Figure. 75. Frequency decomposition of the microphone signal (Test 2).....	142
Figure. 76. Frequency decomposition of the PVDF sensor signal (Test 3).....	143
Figure. 77. Frequency decomposition of the dynamometer force signal (Test 3, the force in the X direction).....	144
Figure. 78. Frequency decomposition of the accelerometer signal (Test 3, the acceleration in the X direction).....	144
Figure. 79. Frequency decomposition of the microphone signal (Test 3).....	145

NOMENCLATURE

A_i = Area of the PVDF sensor electrodes whose surface normal is parallel to the corresponding component i of the electric displacement field vector (m^2)

C_F = Capacitance of the capacitor in the charge amplifier feedback loop (Farad)

d = Piezoelectric stress coefficient matrix (C/N)

D_0 = Shank diameter of the end mill (m)

D = Electric displacement field vector (3 by 1) (C/m^2)

D_i = The i^{th} component of the electric displacement field vector D (C/m^2) ($i = 1, 2, 3$)

E = Electric field vector (3 by 1) (V/m)

E_i = Young's modulus of the PVDF sensor along the i^{th} axis (N/m^2)

E_t = Young's modulus of the end mill (N/m^2)

E_o = Voltage output of a unbalanced Wheatstone bridge (V)

E_{EX} = Excitation voltage of a Wheatstone bridge (V)

F_x = Transverse force (N)

F_y = Feed force (N)

F_z = Axial force (N)

F_r = Radial force (N)

F_t = Tangential cutting force (N)

$\underline{\underline{G}}(s)$ = Continuous time transfer function matrix between cutting forces and strain at the location of the PVDF sensor

$\underline{\underline{G}}_{AA}(s)$ = Continuous time transfer function matrix of the anti-aliasing filter

$\underline{\underline{G}}_{AA}(z)$ = Discretized version of $\underline{\underline{G}}_{AA}(s)$

$\underline{\underline{G}}_C(s)$ = Continuous time transfer function matrix of the charge amplifier circuitry

$\underline{G}_C(z)$ = Discretized version of $G_C(s)$

$\underline{G}_{COMP}(z)$ = Discrete transfer function of the FIR compensation filter

$\underline{G}_{PVDF}(s)$ = Transfer function matrix between the strain picked up by the PVDF sensor and the charges generated on the electrodes of the PVDF sensor

H_{xi} = The distance from the center of PVDF sensor i to the neutral axis with respect to bending moment created by F_x (m)

H_{yi} = The distance from the center of PVDF sensor i to the neutral axis with respect to bending moment created by F_y (m)

K = Gage factor of a metal foil strain gauge

L = Distance from the idealized concentrated feed/transverse force to the center of the PVDF sensor (m)

e^σ = Dielectric permittivity matrix at a constant stress field (Farad/m)

p^σ = pyroelectric coefficient vector at a constant stress field σ (3 by 1) (C/m²/K)

p^σ_i = The i^{th} component of the pyroelectric coefficient vector p^σ (C/m²/K) ($i = 1, 2, 3$)

q = Electric charge generated in the electrodes of a PVDF sensor (C)

q_i = Electric charge generated at the electrodes of PVDF sensor i (C)

s^E = Elastic compliance matrix at a constant electric field (m²/N)

t = Elapsed time since the start of tool rotation (s)

ΔT = Average temperature rise in a PVDF sensor (K)

ΔT_i = Average temperature rise in the i th PVDF sensor (K)

V = Voltage output of a PVDF sensor or a PVDF sensor rosette (V)

V_i = Voltage generated between the electrodes of PVDF sensor i (V)

Y_i = Young's modulus of the PVDF sensor along the i^{th} axis ($i = 1, 2, 3$)

α = Thermal expansion coefficient vector for a PVDF sensor (6 by 1)

α_h = Coefficient of thermal expansion of the host structure

α_i = The i^{th} component of the thermal expansion coefficient vector α ($i = 1, 2, 3, 4, 5, 6$)

ε = Strain vector in vogit notation (6 by 1) (m/m)

ε_h = Strain component of interest in the host structure (m/m)

ε_{ia} = Axial strain in end mill at the location of PVDF sensor i

ε_i = Axial strain in the i^{th} axis of the PVDF sensor

ε_{it} = Transverse strain in end mill at the location of PVDF sensor i

θ = angular position of the PVDF sensor with respect to the machine-centered coordinate system (radian)

κ = Strain transfer coefficient of the adhesive

σ = Stress vector in vogit notation (6 by 1) (N/m^2)

σ_i = The i^{th} component of the stress vector σ (N/m^2) ($i = 1, 2, 3, 4, 5, 6$)

ν_t = Poisson's ratio of the end mill

ν_h = Poisson's ratio of the host structure

φ_0 = Initial angular position of tool with respect to the machine centered coordinate system (radian)

ω_0 = Angular velocity of the cutting tool (radian/s)

SUMMARY

Analytical force and dynamic models for material removal processes such as end and face milling do not account for material and process related uncertainties such as tool wear, tool breakage and material inhomogeneity. Optimization of material removal processes thus requires not only optimal process planning using analytical models but also on-line monitoring of the process so that adjustments, if needed, can be initiated to maximize the productivity or to avoid damaging expensive parts. In this thesis, a Polyvinylidene Fluoride (PVDF) sensor based process monitoring method that is independent of the cutting conditions and workpiece material is developed for measuring the cutting forces and/or torque in milling. The research includes the development of methods and hardware for wireless acquisition of time-varying strain signals from PVDF sensor-instrumented milling tools rotating at high speeds and transformation of the strains into the measurand of interest using quantitative physics-based models of the measurement system. Very good agreement between the measurements from the low cost PVDF sensors and the current industry standard, piezoelectric dynamometer, has been achieved. Three PVDF sensor rosettes are proposed for measuring various strain components of interest and are shown to outperform their metal foil strain gauge counterparts with significantly higher sensitivity and signal to noise ratio. In addition, a computationally efficient algorithm for milling chatter recognition that can adapt to different cutting conditions and workpiece geometry variations based on the measured cutting forces/torque signals is proposed and evaluated. A novel complex exponential model based chatter frequency estimation algorithm is also developed and validated. The

chatter detection algorithm can detect chatter before chatter marks appear on the workpiece and the chatter frequency estimation algorithm is shown to capture the chatter frequency with the same accuracy as the Fast Fourier Transform (FFT). The computational cost of the chatter detection algorithm increases linearly with data size and the chatter frequency estimation algorithm, with properly chosen parameters, is shown to perform 10 times faster than the FFT. Both the cutting forces/torque measurement methodology and the chatter detection algorithm have great potential for shop floor application. The cutting forces/torque measurement system can be integrated with adaptive feedback controllers for process optimization and can also be extended to the measurement of other physical phenomena.

CHAPTER 1 INTRODUCTION

Motivation and Problem Statement

Material removal processes such as end milling and face milling (henceforth referred to as milling) are used extensively in a wide range of industries including aerospace and automotive. One example is the production of large structurally critical monolithic airframe components [1]. Analytical models of the milling process do not account for various process and material uncertainties such as tool wear, tool breakage, and material inhomogeneity. Therefore, optimization of the milling process requires not only optimal process planning using analytical models, but also real-time monitoring of the cutting process to ensure that high quality parts are produced at the highest possible rate while minimizing defects and scrap.

The cutting forces and torque in milling are key process responses that can be used to monitor the state of the process, since they can be used as a proxy for tool wear, tool breakage, material abnormalities, chatter, etc. While several researchers have developed mechanistic cutting force models for milling [2-4] with the ultimate goal of understanding the process, their models do not account for material and process related uncertainties. The current *de facto* industry standard for cutting force measurement, piezoelectric dynamometers, and other cutting force measurement approaches reported in the literature suffer from at least one of the following drawbacks: 1) high cost, 2) limited bandwidth, 3) intrusiveness, 4) dependency on workpiece material, and 5) low sensitivity due to long transmission path between the signal source and the sensor(s). A low cost,

nonintrusive way of measuring milling forces and torque with high fidelity is therefore needed.

A key limitation in the end milling of airframe structures is chatter vibration, which negatively impacts productivity and often causes irreparable damage to the part and the machine tool spindle. While researchers have developed analytical models for the prediction of chatter vibration based on structural dynamics models and cutting conditions [5-8], they do not account for a wide range of uncertainties such as tool run out, material inhomogeneity, nonlinearity in the cutting force-chip thickness models [9], etc. In addition, reliable structural dynamics models of the workpiece/tool/fixture/machine tool system needed for chatter prediction are not available. Therefore, on-line detection and suppression of chatter via real-time process monitoring is still necessary.

Although a lot of work on on-line chatter detection in milling has been reported, they suffer from at least one of the following drawbacks: 1) the sensing units used to monitor the process response are either intrusive or prohibitively expensive (such as piezoelectric dynamometers), 2) the reported chatter detection algorithms are expected to work only in research labs since they fail to take into account various events that may occur during the machining process such as varying cutting conditions, geometric discontinuities in the workpiece, tool wear, tool chipping/breakage, etc., and 3) the reported chatter monitoring methodologies do not lend themselves to networked monitoring and control of machining processes and remote decision making. Therefore, a minimally intrusive, adaptable and industry-friendly chatter detection methodology that facilitates intelligent information retrieval is still highly desirable.

To summarize, the needs of low cost, adaptable and industry-friendly solutions for real time monitoring and optimization of the milling process form the motivation for this research. New technologies and approaches that are different from the traditional workpiece or machine tool structure based measurement/monitoring systems need to be explored.

PVDF Sensor

Thin film sensors have been proposed as a promising candidate for surface strain and temperature measurement [10]. They can be either sputtered onto the specimen or simply attached to the specimen using adhesives. In order for the sensor to be mounted on a specimen of irregular shape, it has to be sufficiently flexible. Thin film Polyvinylidene Fluoride (PVDF) piezoelectric sensors possess this characteristic. In addition, they are low cost (~\$5 per sensor) and offer a unique combination of wide bandwidth (with resonant frequency above 10 MHz), fast response, high dynamic range (up to 2% strain) and high strain sensitivity (around $10 \text{ mV}/\mu\epsilon^1$) [11]. Examples of using PVDF sensors in strain sensing in non-machining applications can be found in the literature [12, 13].

Research Objectives

In light of the motivations and problems stated in the beginning of this chapter, this research aims to create novel, low-cost and non-intrusive wireless sensor systems for measuring the cutting forces and torque in milling and to establish computationally

¹ $\mu\epsilon$ stands for micro strain

efficient algorithms for milling chatter detection and chatter frequency estimation. The specific objectives of this research are as follows:

1. Develop quantitative physics-based models for PVDF sensor based measurements.
2. Demonstrate high fidelity, real-time measurement of cutting force and torque in milling using PVDF sensors and quantitative physics-based models.
3. Establish a computationally efficient milling chatter detection method.

The research objectives of this thesis are accomplished through a comprehensive literature review of the prior work followed by scientific studies and rigorous experimental validation of the proposed approaches.

Proposed Approaches

A brief overview of the PVDF sensor based wireless measuring and monitoring approach is given here. The cutting forces/torque in milling will be obtained in real-time by measuring the dynamic strains induced in the tool during cutting using a thin piezoelectric PVDF film attached to the tool shank and transforming the strains to cutting forces/torque using quantitative physics-based models. The sensor can be coupled with low-profile electronics with embedded intelligence for detecting the onset of chatter and pinpointing the dominant chatter frequency. Chatter alarms, if present, can be wirelessly transmitted to a nearby base station, where corrective measures can be initiated. The overall approach is illustrated in Figure. 1.

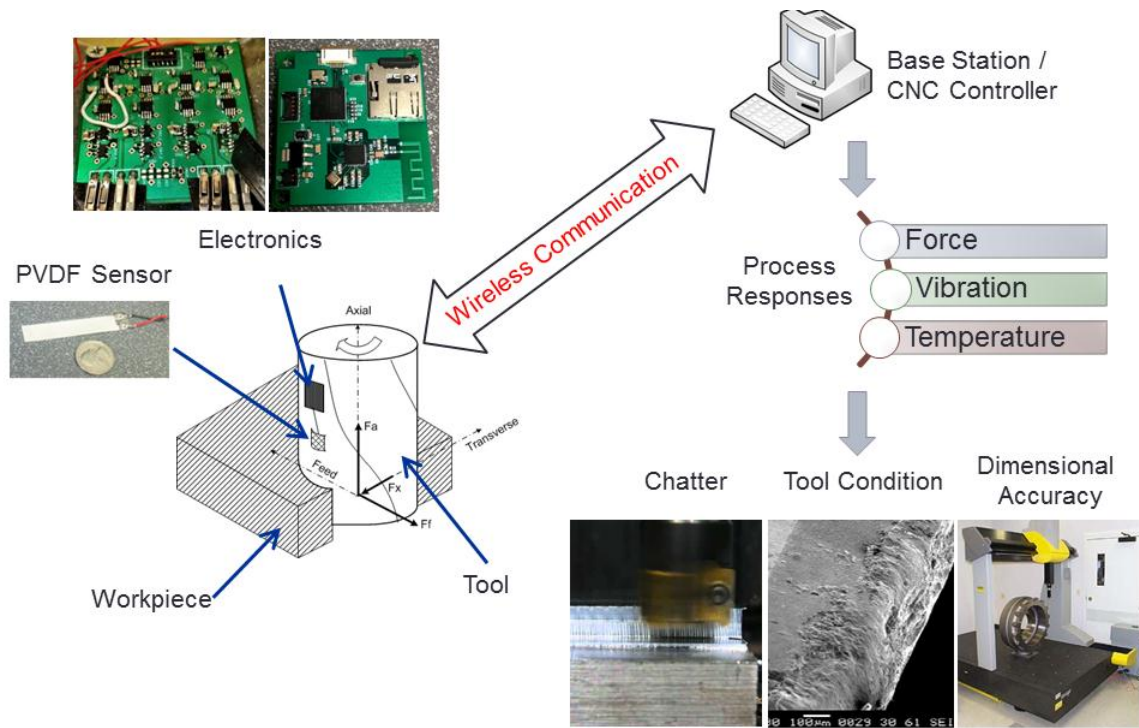


Figure. 1. Overall approach to wireless milling process monitoring.

Thesis Outline

The remainder of this thesis is organized as follows. Chapter 2 contains a comprehensive review of the prior work and existing methods. Chapter 3 introduces a novel PVDF piezoelectric strain sensor based method for monitoring of in-plane cutting forces in end milling and experimental validation of the proposed method. Chapter 4 presents new arrangements of PVDF sensors to maximize their sensitivity to a particular cutting force component of interest and to minimize their sensitivity to irrelevant components. The design of a general purpose PVDF rosette is also proposed and investigated. Chapter 5 covers a computationally efficient algorithm for on-line chatter detection and chatter frequency estimation and experimental validation of the proposed algorithm. In Chapter 6, the PVDF torque sensor based on the shear strain rosette

presented in Chapter 4 is prototyped and experimentally validated in milling. The performance of the PVDF torque sensor is also compared with three popular sensors for chatter detection, namely, piezoelectric dynamometer, accelerometer, and acoustic microphone. Finally, the conclusions and future recommendations of this work are given in Chapter 7.

CHAPTER 2 LITERATURE REVIEW

A critical review of the relevant work available in the literature is presented in this Chapter. The review is divided into four areas: 1) prior work in machining process monitoring, especially wireless machining process monitoring, 2) PVDF based sensing applications, 3) monitoring of cutting forces/torque in milling, and 4) on-line recognition of chatter in milling.

Wireless Machining Process Monitoring

Machining process monitoring is a critical aspect of machining process automation and has long been pursued by researchers [14-16]. Different types of sensors such as piezoelectric ZnO films [15, 17, 18], acoustic emission sensors [19], resistance thermometers [20], thin film thermocouples [21] and thin film strain gauges [22] have been used for monitoring of machining processes including milling, turning, grinding, lapping and chemical mechanical polishing. Recently, the application of wireless sensing in machining process monitoring has attracted the interest of the research community. It has been demonstrated that tool temperature and spindle vibration data can be acquired wirelessly by embedding low profile sensors and wireless transmitters into the cutting tool and spindle housing [23, 24]. Attempts have also been made to wirelessly detect the onset of chatter [25], predict the chatter frequency [26], measure the cutting torque [27], predict the cutting forces and monitor tool wear [28] in the milling process using an instrumented end mill. Wireless acquisition of cutting temperature using a thermal sensor embedded in the rake face of a PCBN insert was also demonstrated [29, 30]. The method, however, adds significantly to the cost of tool production.

PVDF Based Sensing Applications

Piezoelectric sensors made from PVDF polymers are promising alternatives to metal foil strain gauges (MFSGs) for structural sensing applications where only the dynamic or quasistatic signals are of interest. Compared to MFSGs, PVDF sensors feature high sensitivity, high dynamic range and broad frequency bandwidth. In addition, it is possible to acquire voltage signals directly from PVDF sensors without external power supply, making them ideal for remote sensing solutions. Compared with piezoelectric ceramics such as Lead Zirconate Titanate (PZT), PVDF polymers feature smaller thickness, higher flexibility and deformability, and lower Young's modulus, thereby minimizing the impact of sensor instrumentation on the dynamics of the host structure. This is particularly important for host structures that have complex shapes (e.g. weld joints) or possess low stiffness (e.g. plastics). More importantly, the PVDF polymer shows different sensitivities to strains along the two in-plane axes, facilitating the decoupling of strain components in a general strain field.

Previous studies on PVDF sensors either employ them as a qualitative measuring unit [31, 32], or use them in simple loading conditions such as uniaxial bending or uniaxial tension/compression [12, 33, 34]. Little effort has been devoted to isolating a particular strain component of interest using multiple PVDF sensors when the host structure is under complex loading. The method proposed by [13] necessitates two exact host structures with different sensor configurations, which limits its practical value. The study by [35] isolates the uniaxial strain by taking advantage of the low Poisson's ratio of the host structure material. Thus, it is not generally applicable to other materials. Among the limited attempts to calibrate the measured sensor signal with actual strains, the

models reported in different studies contradict each other. For example, the model reported by Sirohi and Chopra [34] ignored the contribution of lateral strain in the host structure to the longitudinal stress in the piezoelectric sensor, while the constitutive relation between stress and strain given in Zhang et al. [33] was incorrect. The models reported by [36] and [37] avoid these drawbacks but are limited to the special case of bending strain. Besides, none of the previous studies compensate for thermal strains and the pyroelectric effect of the PVDF material.

Monitoring of Cutting Forces/Torque in Milling

Among the large number of machining process responses, the feed and transverse forces are of paramount practical significance since they can be used as a proxy for the detection of tool wear, tool breakage, material abnormalities and chatter [16, 38]. Current state-of-the-art for accurate measurement of forces in milling consists of platform or rotating piezoelectric force dynamometers. However, these force sensing systems suffer from several limiting drawbacks including: (1) large size, fragility and intrusiveness to the process, (2) lowering of dynamic stiffness of the cutting tool/workpiece/spindle/machine tool system, (3) limited bandwidth (typically 2~4 KHz), (4) high cost, and (5) dependence on workpiece mass and geometry (for platform dynamometers).

Several attempts have been made to measure the cutting forces and torque in milling with forces/torque sensors integrated into the spindle housing [39-42]. These methods usually require significant installation effort and the signal is usually corrupted by the spindle dynamics and inertial forces. Also, the sensitivity of such a measurement system is typically low because of the long transmitting path between the signal source,

i.e., cutting zone, and the signal pick-up location(s). The novel method of correlating forces with the control signals of active electro-magnetic spindle bearings [43] is not applicable when other types of bearings are used. Other methods such as correlating the feed motor current with the cutting force [44], indirect force measurement via the acceleration signal [45], and strain gauge based platform dynamometers [46] suffer from the drawback of narrow bandwidth. Although the force measurement system proposed in [47] is capable of measuring the cutting forces acting on each individual cutting insert, the high cost and intrusiveness of the system limits its practical usefulness.

All of these drawbacks severely inhibit the widespread adoption of piezoelectric dynamometers and point to the need for a non-intrusive and relatively low-cost measurement system for use in real time monitoring of forces/torque in production milling processes as well as in research and development environments.

With the capability of data retrieval from rotating tools, strain gauge rosettes are installed on the cutting tool to measure the cutting forces in [28] and milling torque in [27, 48]. The signal-to-noise ratio of the sensor is improved due to the shortened transmitting path between the cutting zone and the sensor. However, the low sensitivity of metal foil strain gauges still poses a problem and necessitates stringent signal conditioning of the sensor signal. In addition, the mechanistic model used in [28] suffers from the drawback that the model coefficients depend on the workpiece and cutting tool materials. If either material is changed, the model needs to be recalibrated.

On-line Recognition of Chatter in Milling: Sensors and Algorithms

Various sensing methods have been used for chatter monitoring in various machining processes (mostly turning, milling, boring, grinding and drilling). They include accelerometers [49-69], force sensors [49, 51-55, 64, 67, 70-88], acoustic microphones [89-94], cutting torque sensors [49, 79, 95-98], mechanical stylus profiler [99], acoustic emission sensors [49, 100-102], ultrasound [103], spindle motor current sensor [104], electrical power sensor [49], eddy current sensor [65, 105], and workpiece surface image sensor [106]. An acceptable sensor must have adequate sensitivity and a wide bandwidth (since chatter frequencies typically range from 200 Hz to as high as 4,000 Hz [89]), be non-intrusive, low-cost and easy to use. Review of past work indicates that force dynamometers, acceleration sensors and acoustic microphones are the most commonly used sensors for chatter detection. The pros and cons of these three types of sensors are summarized in [89].

In this work, the use of a thin-Film PVDF sensor for chatter detection is proposed because of its wide range of favorable features including low cost, high sensitivity, high flexibility and broad bandwidth. When deployed on the tool shank, unprecedented signal to noise ratio (SNR) can be achieved due to the shortened path between the cutting zone and the sensor. Preliminary work carried out as part of this thesis [36] reveals that signals acquired by the PVDF sensors has the same fidelity as those acquired by piezoelectric dynamometers, especially when dynamic frequency content is involved. Another important advantage of the PVDF sensor is its versatility. PVDF sensors can be configured into various types of rosettes so that only the force component of interest is measured.

In addition to choosing a suitable source signal, a high performance signal processing algorithm is needed for detecting chatter in its incipient stages. The ideal algorithm should be physically meaningful, computationally efficient and independent of the cutting conditions. In addition to recognizing the onset of chatter, it should supply other useful information such as the dominant chatter frequency to help suppress the emerging chatter. Past work on chatter detection generally employs three types of signal processing methods, including: (i) transform domain analysis such as the Fourier transform, power spectrum, short time Fourier transform (STFT) [49, 65, 83, 84, 88, 89, 92, 93, 98, 105, 107, 108] and wavelet transform [53, 57, 58, 74, 77, 79, 99, 103], (ii) time domain analysis [50-52, 54, 67, 68, 70, 72, 75, 76, 78, 82, 86, 94, 96, 97, 104], and (iii) pattern recognition [55] and classification algorithms such as artificial neural networks [63, 69, 85, 87, 102, 103, 109, 110], fuzzy logic [91], hidden Markov model [66, 111], support vector machine [58, 66] and index based reasoner [95].

Traditional Fourier Transform and power spectrum analysis techniques are not suited for on-line chatter detection. Fourier Transforms of the chatter signal can reveal the existence of chatter frequencies but not their “time of arrival” due to the infinite support of the eigenfunctions used in the Fourier Transform. Due to their computational efficiency, linear time-frequency analysis methods such as STFT and Wavelet Transform have been studied extensively by researchers for chatter detection. STFT suffers from the inherent limitation that good time domain and frequency domain resolution cannot be achieved simultaneously. The frequency resolution of the STFT was identified as the primary performance bottleneck of the classic audio signal based chatter suppression system developed in [93]. The wavelet transform provides a better time-frequency

resolution in the low frequency band, however, resolution in the high frequency band is inadequate. Furthermore, when the chatter frequency is not known a priori, it is difficult to identify the number of levels of decomposition needed and the specific level(s) that is (are) sensitive to the onset of chatter. Therefore, chatter detection algorithms based on the wavelet transform [53, 58, 79, 103] may not be able to effectively detect chatter when the cutting conditions change. The choice of the mother wavelet function can also have a major impact on performance of the algorithm, which further complicates the application of wavelet-based methods. Finally, wavelet transform based algorithms for chatter detection proposed in the literature [53, 57, 58, 74, 77, 79, 99, 103] cannot pinpoint the chatter frequency accurately.

Chatter detection methods based on advanced pattern recognition and classification algorithms suffer from the drawback that extensive training is needed before they can work. Also, decisions made by the classification algorithms are not physically meaningful and some of the methods cannot identify the chatter frequency [58, 95].

Time series features such as coherence [56], coarse-grain entropy rate [75], permutation entropy [90], singular values of a Toeplitz matrix of the third order cumulants of acceleration measurements [54], and statistical modeling [78] have been used to recognize chatter in turning. However, the existence of forced vibrations at the tooth passing frequency and its harmonics limits the applicability of these methods in milling.

Descriptive statistical analysis of the cutting force [70] and audio signal [94] was used to detect chatter in milling. The assumption made in [70] that the cutting force

approaches a Gaussian distribution when chatter occurs is questionable. The once-per-revolution sampling method proposed in [94] is computationally very efficient but sensitive to the measurement errors and various transients events in the cutting process. Furthermore, most time series analysis methods [50, 51, 54, 70, 72, 75, 78, 82, 94, 104] cannot identify the chatter frequency.

In the early work by Braun [65] the phase information of the complex demodulated acceleration signal acquired from turning was found to be sensitive to the state transition of the cutting process dynamics. The time domain method obviates the difficulties associated with frequency domain methods when non-stationary signals are involved. However, the phase computed using a regular arctangent subroutine is, in general, discontinuous and unwrapping of the phase can be difficult [112].

Choi and Shin [77] proposed a cutting condition independent and computationally inexpensive chatter index that is inversely related to the dimension of the cutting process dynamics. However, it is not clear whether the reduction in dimension occurs before or after chatter is fully developed.

Al-Regib and Ni [50] suggested using the ratio of the high-frequency band energy to the total energy in a signal as an indicator of chatter. While this normalized index is process and cutting condition independent, its performance in milling is questionable because, in the incipient stages of chatter, the energy around the chatter frequencies is smaller than at the spindle speed related frequencies. Also, it is hard to define what a high frequency band is when the chatter frequencies are unknown.

Dijk et al. [59] proposed an interesting method, which decomposes the signal acquired from a spindle mounted accelerometer into two parts: periodic part due to tool

rotation and perturbation part due to tool deflection and chip regeneration. The former part was modeled as a moving average (MA) process and the latter as an autoregressive (AR) process, which is recursively estimated and used for chatter detection. However, the assignment of an AR model to the chip regeneration part of the signal is not supported by cutting force models. In addition, significant estimation errors may occur if the order of the AR model is not chosen properly.

The multi-sensor and multi-index chatter detection approach developed by Kuljanić et al. [49, 109] effectively improves the reliability of the chatter detection system and reduces false alarm rate. However, the method is computationally expensive and significant instrumentation effort is needed.

Finally, since most of the above methods are only validated in simple straight line cutting experiments, it is unclear whether they would still work if the toolpath is curvilinear or if the workpiece geometry has discontinuities (such as holes, slots, pockets, etc.) that can cause transient dynamic behavior during cutting.

Summary

It can be seen from the literature survey that all past applications of PVDF sensors involve qualitative instead of quantitative measurements. In addition, existing methods for monitoring of cutting force and/or torque in milling are intrusive, prohibitively expensive for widespread adoption, possess limited bandwidth, have low sensitivity, or are dependent on the workpiece material. The reported methods for on-line chatter detection suffer from at least one of the following drawbacks: 1) difficulty with processing non-stationary signals, 2) high computational cost, and 3) possible sensitivity to transient events in milling other than chatter vibrations.

The rest of this thesis describes the analysis, development and experimental validation of low cost, PVDF sensor based wireless cutting force and cutting torque measurement systems and a computationally efficient algorithm for on-line chatter detection and chatter frequency estimation.

CHAPTER 3 PVDF SENSOR BASED CUTTING FORCE MEASUREMENT

Introduction

In this chapter, a novel, low cost and non-intrusive method of monitoring the feed and transverse forces in the peripheral end milling process is described. This work is an extension of the authors' prior work on slot end milling process [36], where wireless on-line monitoring of the feed force was demonstrated while neglecting the contribution of the axial force to the elastic deformation of the tool. This work has also been reported in another authors' paper [113]. Although wireless functionality is not incorporated into the peripheral end milling work presented in this chapter, a wireless transmitter can be easily integrated into the described hardware for real time data acquisition. In the following sections of the chapter, the overall methodology and approach is described, followed by experimental validation, discussion of results and conclusions.

Background

A brief description of the force measurement system shown in Figure. 2 is given in this section. The PVDF sensor(s) mounted on the shank of the end mill are wired to the signal conditioning and data logging electronics designed and built in-house, which are mounted on the tool holder in a polyurethane housing built using stereolithography. The

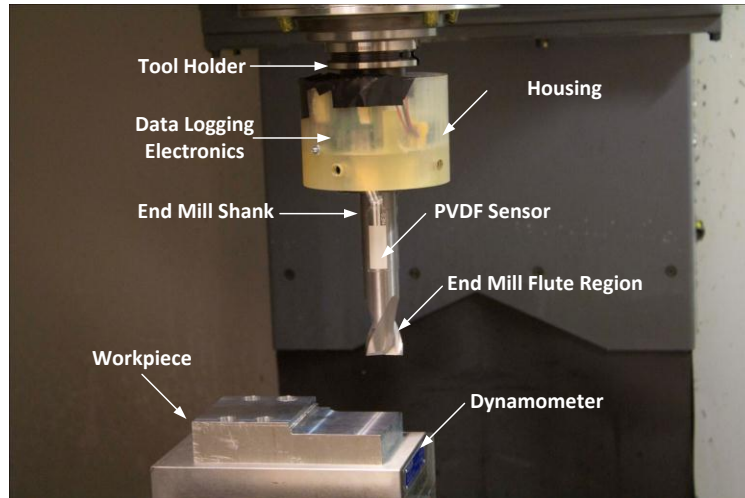


Figure. 2. Force measurement system setup for peripheral end milling.

cutting forces acting on the end will elastically deform the tool. The elastic strain produced in the tool at the PVDF sensor location then gives rise to electric charges at the PVDF sensor electrodes due to the piezoelectric effect. The charges are converted into voltage signals using an on-board charge amplifier, whose output is passed through an anti-aliasing filter before being sampled by the embedded microcontroller unit (MCU), which logs the sampled signal into an on-board Secure Digital (SD) card. The signal flow just described is summarized block-diagrammatically in Figure. 3.

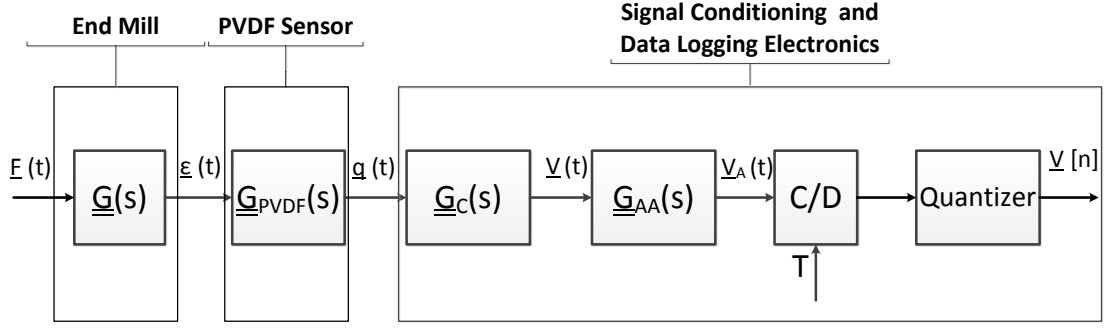


Figure. 3. Signal flow of the force measurement system.

In Figure. 3, $\underline{F}(t)$, $\underline{\varepsilon}(t)$, $\underline{q}(t)$, $\underline{V}(t)$, $\underline{V}_A(t)$, $\underline{V}[n]$ and T denote the cutting force component vector, the strain response at the PVDF sensor location, the charges generated at the sensor electrodes, the voltage signal produced by the charge amplifier, the voltage signal output by the anti-aliasing filter, the digital voltage samples collected by the data logging unit and the sampling period, respectively. The single underline notation used for the variables denotes that there are multiple force components (i.e. F_x , F_y , F_z) and multiple PVDF sensors (e.g. ε_1 , ε_2 , ε_3) involved. Accordingly, the double underline notation is used to denote the transfer function blocks (i.e. $\underline{G}(s)$, $\underline{G}_{PVDF}(s)$, $\underline{G}_C(s)$, $\underline{G}_{AA}(s)$) which are, in general, matrices.

To accurately measure the input cutting force signals, the transfer function of each block in the signal flow chain needs to be modeled so that the overall transfer function between the discrete time voltage sample and the continuous time series forces can be found.

Force Measurement System Modeling

Mechanical transfer function between cutting forces and strain

To measure the feed and transverse forces in peripheral end milling, at least two PVDF sensors are needed because each sensor will provide one equation relating the feed force and transverse force and two equations are needed to solve for the two force components. In this work, as shown in Figure. 4, a strain gauge rosette design consisting of three PVDF sensors which are mounted 120° apart from each other on the tool shank is used. Robustness of the measurement system is increased by using one more than the minimum required number (2) of sensors.

Consider the schematic of the peripheral end milling process shown in Figure. 4, which establishes two major coordinate systems: 1) the machine centered coordinate system representing the feed (Y), transverse (X) and axial (Z) force directions, and 2) the tool centered coordinate system that corresponds to the tangential (T), radial (R) and axial force (Z) directions. In the following model development it is assumed that the tangential and radial forces, which are in reality distributed forces, can be approximated by two concentrated loads acting on the tool at a distance equal to half the axial depth of cut (denoted L in Figure. 4). With this assumption, the tool, which is actually subjected to

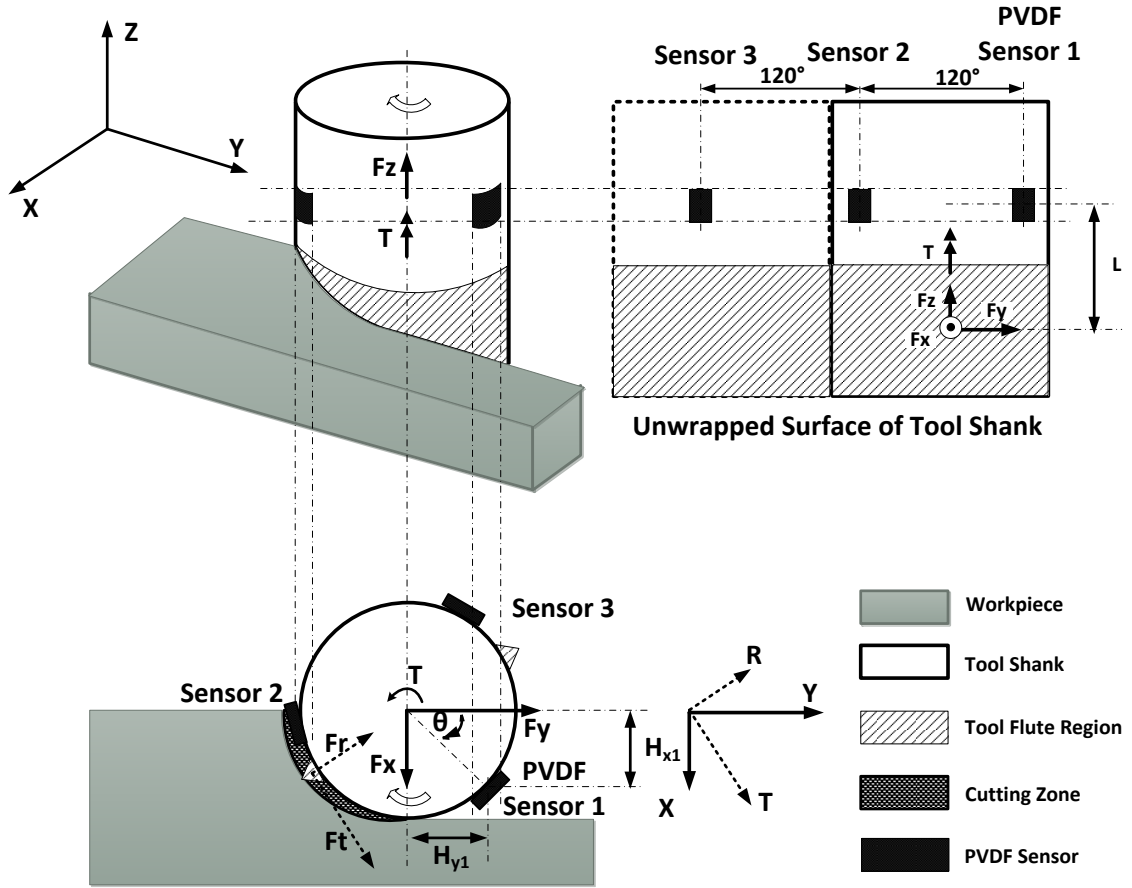


Figure. 4. Schematic of PVDF sensor deployment in peripheral end milling process.

complex loading during cutting, can be treated with simplified loading conditions, namely, biaxial bending in the feed and transverse directions and torsion about the tool axis. Of these two deformation modes, bending is considered to be more critical in this work since it can cause the tool to be pushed away from or pulled into the workpiece, thereby altering the effective axial and radial depth of cut, while the shear strain caused by torsion is neglected here since the PVDF sensor is insensitive to the in-plane shear strain for reasons to be discussed later. A final modeling assumption is that the tool deformation is such that small strain theory of elasticity is applicable.

Treating the end mill as a cantilever beam clamped in the tool holder and assuming the Euler-Bernoulli beam theory applies, the bending strain induced in the tool at the location of the PVDF sensor i ($i = 1,2,3$) can be found using the bending formula²:

$$\varepsilon_{ia} = -\frac{F_y LH_{yi} + F_x LH_{xi}}{E_t I_{zz}} = -\frac{64L(F_y H_{yi} + F_x H_{xi})}{E_t \pi D_0^4} \quad (i = 1, 2, 3) \quad (1)$$

Please note that the flutes of the cutting tool should have minimal impact on the strain in the tool at the location of the PVDF sensors, provided that the sensors are located sufficiently far away from the transition region between the flutes and tool shank.

Transverse strain due to the Poisson effect is then

$$\varepsilon_{it} = -\nu_t \varepsilon_{ia} \quad (i = 1, 2, 3) \quad (2)$$

It can be shown that the axial normal strain caused by the axial force F_z is usually one to two orders of magnitude lower than the bending strain obtained from Eq. (1) when the axial and feed forces are comparable in magnitude. To see this, consider the ratio of the bending strain ε_x caused by F_x to the axial strain ε_z caused by F_z (let H_x be $D_0/2$)

² The sign convention indicated in Figure. 4 is used

$$\frac{\varepsilon_x}{\varepsilon_z} = \frac{\frac{32F_x L}{\pi D_0^3}}{\frac{4F_z}{\pi D_0^2}} = \frac{F_x}{F_z} \frac{8L}{D_0} \quad (3)$$

Considering the fact that the axial forces are usually smaller in magnitude than the in-plane forces in end milling process, the axial normal strain is not considered in the remainder of the model development. More rigorously, it is possible to eliminate the contribution of axial normal strain by employing a four-piece PVDF sensor rosette design, which is described in detail in Chapter 4.

As the tool rotates, H_{yi} and H_{xi} vary constantly as described by Eqs. (4) and (5):

$$H_{yi} = \frac{D_0}{2} \cos(\theta + \theta_i) \quad (i = 1, 2, 3) \quad (4)$$

$$H_{xi} = \frac{D_0}{2} \sin(\theta + \theta_i) \quad (i = 1, 2, 3) \quad (5)$$

where $\theta_1 = 0^\circ$, $\theta_2 = 120^\circ$ and $\theta_3 = 240^\circ$. Combining Eqs. (1), (4) and (5), the bending strain at the i^{th} sensor is

$$\varepsilon_{ia} = -\frac{32L(F_y \cos(\theta + \theta_i) + F_x \sin(\theta + \theta_i))}{E_t \pi D_0^3} \quad (i = 1, 2, 3) \quad (6)$$

where θ is given by

$$\theta = \omega_o t + \phi_o \quad (7)$$

where ω_o and ϕ_o are the angular velocity of the end mill and the initial angular position(s) of the sensor(s), respectively.

Note that a static model is used here to relate the strain at the PVDF sensor location to the dynamic cutting forces. The static model is sufficient when the tooth passing frequency is below the lowest natural frequency of the cutting tool/ workpiece /machine tool system. A stationary impact hammer test was performed to find the lowest natural frequency of the system used in this study (as shown in Figure. 2) in the feed (Y) and transverse directions (X). The test was repeated 25 times for each direction and a least squares based H_1 algorithm [114] was used to find the frequency response function (FRF). The accelerance form of the FRF is shown in Figure. 5. It can be seen that the 1st stationary modes of the X and Y directions are nearby (410 Hz and 390 Hz, respectively). Since rotating FRFs can be assumed to have higher stiffness than stationary ones owing to the bearing stiffness [115], the first rotating modes in the X and Y directions are expected to be higher than 410 Hz and 390 Hz, respectively. This justifies the assumption

that a static strain-force model is applicable as long as the excitation frequency due to the cutting force is below 390 Hz. Above 390Hz, a frequency-dependent transfer function is needed to relate the strain response to the cutting force. It is worth mentioning that the impact hammer test was conducted when the tool tip was free of constraints. During cutting, the tool tip will be in contact with the workpiece and the effect of this change in the boundary condition on the first natural mode of the system remains to be studied. However, some insights may be gained by assuming that the cutting tool behaves like a fixed-free beam (i.e. cantilever beam) when the tool tip is free and a fixed-pinned beam when the tool tip is supported by the workpiece; the first natural mode of the system will be higher in the case of the simply supported beam [116].

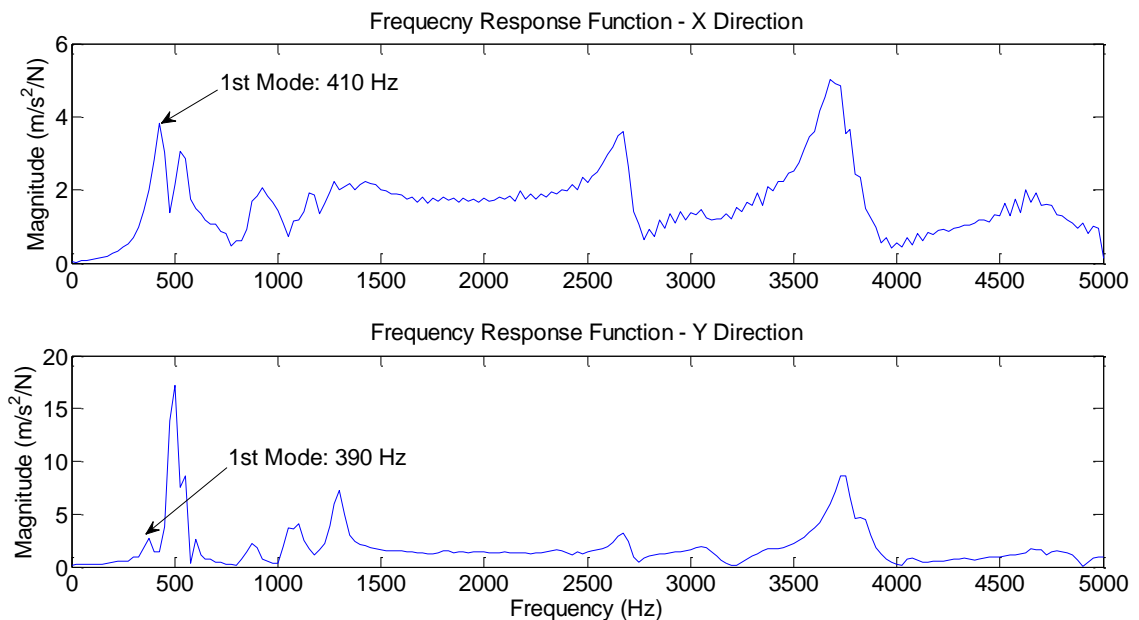


Figure. 5. Frequency response function of the cutting tool/tool holder/spindle/machine tool system used in the study (see Figure. 2).

Modeling of PVDF sensor strain-charge relation

Given that the PVDF sensors are bonded to the tool shank using commercially available adhesives such as epoxy glue or double-sided tape, the potential impact of shear lag on the sensor signal must be considered. While the temperature dependence of the adhesive damping may pose a problem under drastic temperature change, it is neglected in this study. If the temperature rise at the sensor location is a concern, either the temperature dependent damping effect needs to be modeled or a temperature-insensitive way of bonding the sensor to the tool shank needs to be used. In this work, the possible influence of shear lag on the measurement is accounted for by assuming that only a certain amount of bending strain is transmitted to the sensor through the adhesive. Therefore, the bending strain induced in sensor i is given by

$$\varepsilon_{ip} = \kappa \varepsilon_{ia} \quad (i = 1, 2, 3) \quad (8)$$

where

$$0 \leq \kappa \leq 1 \quad (9)$$

Note that in most cases it is safe to assume $\kappa = 1$.

In order to relate the strain to the electric charge generated in the PVDF sensor electrodes, the constitutive model of the PVDF sensor needs to be considered. The linear constitutive model given in Eq. (10) will suffice since only small strains are considered.

$$\begin{bmatrix} D \\ \varepsilon \end{bmatrix} = \begin{bmatrix} e^\sigma & d \\ d^T & s^E \end{bmatrix} \begin{bmatrix} E \\ \sigma \end{bmatrix} \quad (10)$$

The constitutive equations of the PVDF sensor in Eq. (10) are referred to as the strain-charge form. Alternative constitutive equations are also available [117]. In Eq. (10) the Voigt notations of the stress vector σ and the strain vector ε are used, s^E is a 6 x 6 elastic compliance matrix, and the piezoelectric stress coefficient matrix d has the following form:

$$d = \begin{bmatrix} 0 & 0 & 0 & 0 & d_{15} & 0 \\ 0 & 0 & 0 & d_{24} & 0 & 0 \\ d_{31} & d_{32} & d_{33} & 0 & 0 & 0 \end{bmatrix} \quad (11)$$

The index i in d_{ij} references the electric axis while index j refers to the mechanical axis, i.e., it relates the electric displacement generated in the i^{th} direction to the mechanical stress applied in the j^{th} direction. For a thin film piezoelectric sheet, the poling is typically in the thickness direction, denoted as axis 3 in

Figure. 6. Axes 1 and 2 refer to the two in-plane axes.

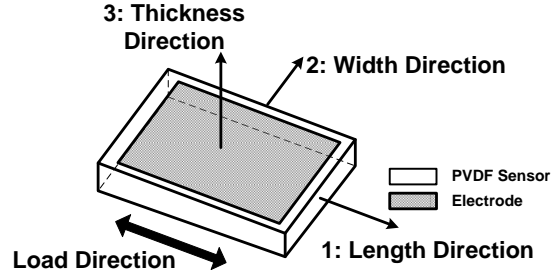


Figure. 6. Schematic of a PVDF sensor element.

When the PVDF piezoelectric element is used as a sensor, there is no externally applied electric field ($E = 0$), consequently,

$$\begin{bmatrix} D_1 \\ D_2 \\ D_3 \end{bmatrix} = \begin{bmatrix} 0 & 0 & 0 & 0 & d_{15} & 0 \\ 0 & 0 & 0 & d_{24} & 0 & 0 \\ d_{31} & d_{32} & d_{33} & 0 & 0 & 0 \end{bmatrix} \begin{bmatrix} \sigma_1 \\ \sigma_2 \\ \sigma_3 \\ \sigma_4 \\ \sigma_5 \\ \sigma_6 \end{bmatrix} \quad (12)$$

It is clear from Eq. (12) that the in-plane shear stress σ_6 does not contribute to the electric displacement component because d_{k6} ($k=1,2,3$) is zero, hence supporting the argument that the PVDF sensor is not sensitive to in-plane shear strains when the PVDF sensor is mounted properly with respect to the tool, i.e., when axis 1 of the PVDF sensor is parallel to the end mill axis.

To compute the electric charges generated by the mechanical strains, the electric displacements need to be integrated over the electrode areas whose surface normals are parallel to the electric displacement components as follows:

$$q = \int D^T dA = \int (D_1 dA_1 + D_2 dA_2 + D_3 dA_3) \quad (13)$$

The PVDF element can be treated as an orthotropic material after being poled, with the symmetry axes coincident with the geometric axes shown in

Figure. 6. Owing to small thickness of the PVDF sensor, it can be assumed that the sensor is in a state of plane stress, i.e., $\sigma_3=\sigma_4=\sigma_5=0$. Consequently, the constitutive equations of the PVDF sensor material in a plane stress state can be written as (with externally applied electric field $E = 0$):

$$\begin{bmatrix} \varepsilon_1 \\ \varepsilon_2 \\ \varepsilon_6 \end{bmatrix} = \begin{bmatrix} \frac{1}{E_1} & \frac{-\nu_{21}}{E_2} & 0 \\ \frac{-\nu_{12}}{E_1} & \frac{1}{E_2} & 0 \\ 0 & 0 & \frac{1}{E_6} \end{bmatrix} \begin{bmatrix} \sigma_1 \\ \sigma_2 \\ \sigma_6 \end{bmatrix} \quad (14)$$

where ν_{lm} is the Poisson's ratio between axes l and m , i.e., the contribution to the normal axial strain along axis m by the normal stress along axis l . Due to symmetry, $\nu_{21}/E_2 = \nu_{12}/E_1$. Using Eq. (8), we have

$$\begin{aligned}\varepsilon_{i1} &= \kappa \varepsilon_{ia} \\ \varepsilon_{i2} &= -\nu_t \kappa \varepsilon_{ia} \quad (i = 1, 2, 3)\end{aligned}\tag{15}$$

Combining Eqs. (14) and (15), σ_1 and σ_2 can be found as:

$$\sigma_{i1} = \frac{E_1 \kappa \varepsilon_{ia} (1 - \nu_{21} \nu_t)}{1 - \nu_{21} \nu_{12}} \quad (i = 1, 2, 3)\tag{16}$$

and

$$\sigma_{i2} = \frac{E_2 \kappa \varepsilon_{ia} (\nu_{12} - \nu_t)}{1 - \nu_{21} \nu_{12}} \quad (i = 1, 2, 3)\tag{17}$$

Combining Eqs. (6), (12), (16) and (17), and integrating according to Eq. (13), the total charge generated in the electrode of the PVDF sensor is given by Eq. (18):

$$q_i = -\frac{32LA_3}{E_t\pi D_0^3} \frac{\kappa}{2\alpha(1-\nu_{21}\nu_{12})} [d_{31}E_1(1-\nu_{21}\nu_t) + d_{32}E_2(\nu_{12}-\nu_t)]$$

$$[F_y(\sin(\theta+\theta_i+\alpha) - \sin(\theta+\theta_i-\alpha)) \quad (18)$$

$$-F_x(\cos(\theta+\theta_i+\alpha) - \cos(\theta+\theta_i-\alpha))] \quad (i=1,2,3)$$

where A_3 is the area of the electrode layer in the PVDF sensor. Note that as α (see Figure. 7) approaches zero,

$$\lim_{\alpha \rightarrow 0} \frac{\sin(\theta+\theta_i+\alpha) - \sin(\theta+\theta_i-\alpha)}{2\alpha} = \cos(\theta+\theta_i) \quad (19)$$

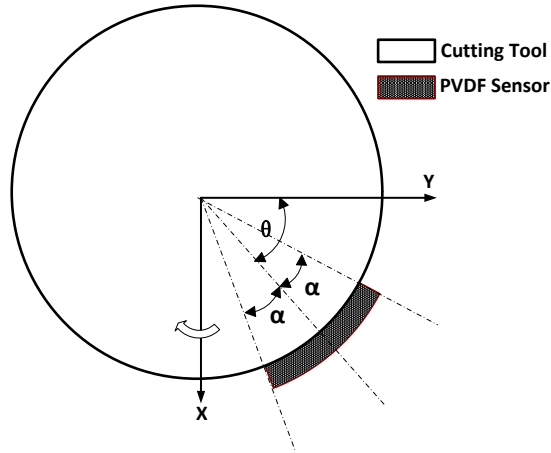


Figure. 7. Angular span of the PVDF sensor on the cutting tool shank.

and

$$\lim_{\alpha \rightarrow 0} \frac{\cos(\theta + \theta_i + \alpha) - \cos(\theta + \theta_i - \alpha)}{2\alpha} = \sin(\theta + \theta_i) \quad (20)$$

which implies that when the sensor is small enough, the strain produced in the PVDF sensors can be assumed to be uniform. Since the materials involved in this study have similar Poisson's ratios ($\nu_i \approx 0.24$ [118], $\nu_{12} \approx \nu_{21} \approx 0.35$, $E_1 \approx E_2$ [119]), we have:

$$(\nu_{12} - \nu_i) \ll (1 - \nu_{21}\nu_i) \quad (21)$$

For the PVDF sensor, $d_{32} \ll d_{31}$ ($d_{32} \approx 10\%-16\%$ of d_{31} [34]). Therefore, the term $d_{32}E_2$ ($\nu_{12} - \nu_i$) can be dropped without significant loss of accuracy and Eq. (18) can be simplified as:

$$q_i = -\frac{32LA_3}{E_i\pi D_0^3} \frac{\kappa d_{31}E_1(1 - \nu_{21}\nu_i)}{1 - \nu_{21}\nu_{12}} \left[F_y \frac{\sin(\theta + \theta_i + \alpha) - \sin(\theta + \theta_i - \alpha)}{2\alpha} - F_x \frac{\cos(\theta + \theta_i + \alpha) - \cos(\theta + \theta_i - \alpha)}{2\alpha} \right]; \quad (i = 1, 2, 3) \quad (22)$$

It is interesting to note that, depending on the relative magnitudes of ν_{12} and ν_i , the term dropped from Eq. (18) can either add to or subtract from the overall sensitivity of the PVDF sensor to the cutting forces. The motivation for performing the foregoing numerical simplification is to rid Eq. (18) from its dependence on d_{32} , which may be of

practical significance when the exact value of d_{32} is not known. In general, since the Possion's ratio of many material is constrained in the range $[0, 0.5]$, it is very likely that Eq. (21) will hold even if another type of tool material is used. However, $d_{32} \ll d_{31}$ is generally not true for other piezoelectric materials. For example, in the case of Lead Zirconate Titanate (PZT), d_{32} is very close to d_{31} . In such cases Eq. (18) must be used.

Modeling of signal conditioning circuits

Before the sensor signal can be sampled by the data logging system, the electric charges generated in the electrodes of the PVDF sensor need to be transformed into a voltage signal via a charge amplifier and filtered so that any frequency content beyond the Nyquist frequency is sufficiently attenuated. The circuitry given in [120] was used as the charge amplifier. For the anti-aliasing filter, a fourth-order Butterworth filter with a cut-off frequency of 400 Hz was designed so that at least 30dB attenuation is achieved at 1KHz or higher. The detailed circuit is given in Figure. 8:

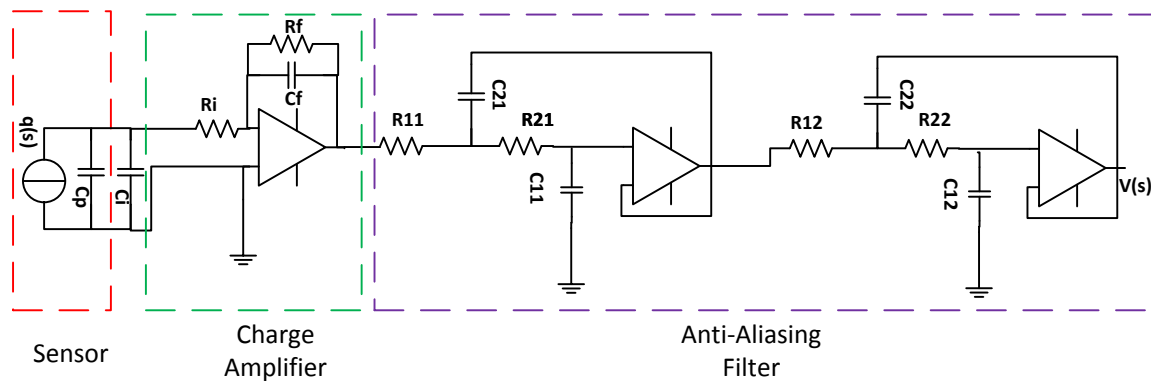


Figure. 8. Diagram for the signal conditioning circuit.

The corresponding transfer function of the signal conditioning circuit can be determined through Laplace domain circuit analysis and given in Eq. (23)

$$V(s) = -\frac{q(s)}{C_F} \cdot \frac{sR_F C_F}{1 + sR_F C_F} \cdot \frac{1}{1 + s(C_p + C_c)} \cdot \frac{1}{1 + sC_{11}(R_{11} + R_{21}) + s^2(C_{11}C_{21}R_{11}R_{21})} \cdot \frac{1}{1 + sC_{12}(R_{12} + R_{22}) + s^2(C_{12}C_{22}R_{12}R_{22})} \quad (23)$$

In the pass band, the amplitude of the voltage signal can be calculated as

$$V_i = -\frac{q_i}{C_F}; \quad (i = 1, 2, 3) \quad (24)$$

where C_F is the capacitance of the capacitor in the feedback loop of the charge amplifier and V_i is the voltage signal generated between the two electrodes of the i^{th} PVDF sensor.

The Bode plot of the transfer function of the signal conditioning circuitry (a charge amplifier and a Butterworth anti-aliasing filter) is shown in Figure. 9. It can be seen that the low frequency content (<15Hz) of the signal is attenuated by the signal conditioning circuitry. The phase of the input signal is distorted since the phase response of the signal conditioning circuitry is slightly nonlinear. Therefore, it is expected that the discrete voltage samples collected by the data logging unit will not capture the magnitude and shape of the cutting force signal exactly. Note that the attenuation of low frequency content is inevitable in signal conditioning of piezoelectric sensors because the charges generated at the sensor electrodes due to mechanical stresses decay over time.

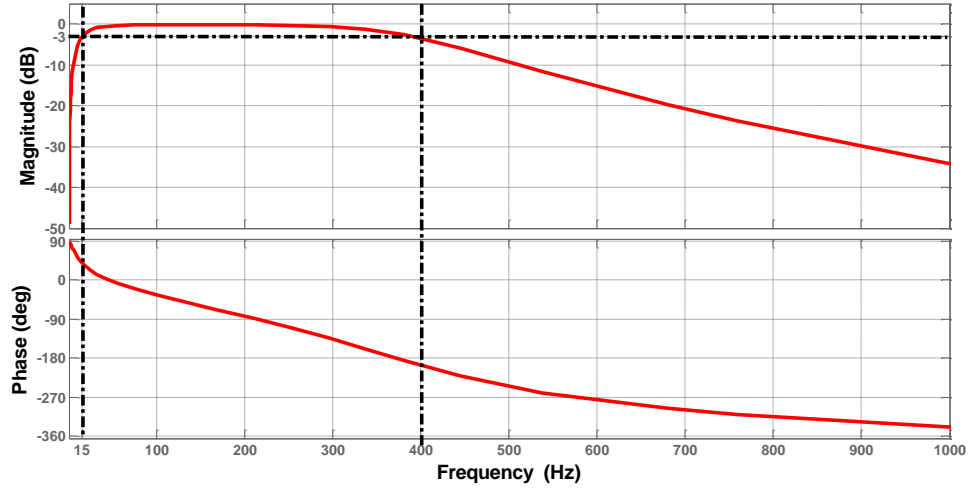


Figure. 9. Bode plot of the transfer function of signal conditioning circuitry.

Determination of cutting force from the PVDF sensor signals

Combining Eqs. (22) and (24), three equations containing two unknowns, F_x and F_y , can be obtained and arranged in matrix form:

$$\begin{bmatrix} V_1 \\ V_2 \\ V_3 \end{bmatrix} = \begin{bmatrix} C_{11}(\theta) & C_{12}(\theta) \\ C_{21}(\theta) & C_{22}(\theta) \\ C_{31}(\theta) & C_{32}(\theta) \end{bmatrix} \begin{bmatrix} F_x \\ F_y \end{bmatrix} \quad (25)$$

C_{ij} in Eq. (25) denotes the element on i^{th} row and j^{th} column. A least squares approach can now be used to solve for F_x and F_y . An alternative approach is to treat θ as an unknown and solve the system of non-linear equations for F_x , F_y and θ . In this work, the former approach is used.

Experimental Verification

To verify the proposed force measurement system, end milling experiments were performed on an Okuma MILLAC 44V CNC milling machine. The experimental setup is shown in Figure. 2. The workpiece materials used were Aluminum 7050-T7451 (AL7050) and AISI 1018 Steel (S1018). A 25.4 diameter two flute tungsten carbide square end mill with a 30 degree helix angle was used. No cutting fluid was used in the tests. All other cutting conditions used in the experiments are listed in Table 1. In addition to the PVDF sensor signal measurement, a 3-component piezoelectric platform dynamometer (Kistler 9257B) was used to measure all three cutting force components produced in the machining tests. This data is used to validate the PVDF strain sensor measurements as described later. A NI DAQ board was used to collect force data from the dynamometer at a rate of 10,000 Hz per channel, while the *in situ* data logging device was programmed to sample the three PVDF sensors mounted on the end mill shank at a rate of 2,000 Hz per channel.

Table 1. Cutting conditions for experimental tests for in-plane force measurement.

Test No.	Spindle Speed (rpm)	Immersion Ratio	Depth of Cut (mm)	Feed per Tooth (mm)	Workpiece Material	Experimentally Obtained K_s (mV/N)
1	750	50%	2.54	0.0508	AL7050	3.90
2	900	50%	2.54	0.0508	AL7050	3.90
3	1050	25%	2.54	0.0635	AL7050	3.64
4	1200	25%	2.54	0.0508	AL7050	3.83
5	1500	50%	2.54	0.0508	AL7050	3.83
6	1650	50%	2.54	0.0508	AL7050	3.83
7	1800	50%	2.54	0.0508	AL7050	3.83
8	1950	50%	2.54	0.0508	AL7050	3.83
9	2100	50%	2.54	0.0508	AL7050	3.83
10	2250	25%	2.54	0.0508	AL7050	3.83
11	2400	30%	2.54	0.0508	AL7050	3.83
12	1050	25%	1.27	0.0254	S 1018	3.75
13	1200	25%	1.27	0.0254	S 1018	3.75
14	1200	38%	1.27	0.0254	S 1018	3.75
15	1350	25%	1.27	0.0254	S 1018	3.75
16	1500	25%	1.27	0.0254	S 1018	3.75
17	1650	25%	1.27	0.0254	S 1018	3.75
18	1800	25%	1.27	0.0254	S 1018	3.75

Calibration of the PVDF sensor signal

In practice, the exact values of some of the constants in Eq. (22) are usually unknown. For example, the Young's modulus of the tool material (E_t), and the piezoelectric stress coefficient (d_{31}) of the PVDF sensors may not be precisely known. In cases where only rough estimates of the constants are available, the PVDF sensor signal must to be calibrated against a reliable signal. In this work, the PVDF sensor signal was calibrated against the dynamometer force signal. To facilitate the calibration, the quantity K_s is defined as follows (see Eqs (22) and (24))

$$K_s = \frac{32LA_3}{E_t\pi D_0^3} \frac{\kappa d_{31}E_1(1-\nu_{21}\nu_t)}{1-\nu_{21}\nu_{12}} \frac{1}{2\alpha C_F} \quad (26)$$

Eq. (24) can now be re-written as:

$$V_i = K_s [F_y(\sin(\theta + \theta_i + \alpha) - \sin(\theta + \theta_i - \alpha)) - F_x(\cos(\theta + \theta_i + \alpha) - \cos(\theta + \theta_i - \alpha))] \quad (27)$$

If the initial angular position of the sensor φ_o and the angular velocity of the tool ω_o are known, the PVDF sensor can be calibrated against the dynamometer force signal simply by finding the scaling factor K_s . When Eq. (21) or $d_{32} \ll d_{31}$ does not hold, K_s is defined as:

$$K_s = \frac{32LA_3}{E_t\pi D_0^3} \frac{\kappa[d_{31}E_1(1-\nu_{21}\nu_t) + d_{32}E_2(\nu_{12} - \nu_t)]}{1-\nu_{21}\nu_{12}} \frac{1}{2\alpha C_F} \quad (28)$$

so that Eq. (27) is still valid. Table 1 lists the values of K_s obtained from calibration against the dynamometer force signal. For the purpose of validation, K_s is calculated from the estimated values of the material constants listed in Table 2. It can be seen that the estimated sensitivity is 5.67 mV/N, which is equivalent to 80 mV/ $\mu\epsilon$ for this particular system or about 4000 times that of a metal foil strain gauge with a gage factor of 2 and an excitation voltage of 10V.

Table 2. Estimation of K_s

E_t	600 GPa
E_1, E_2	5 GPa [34]
ν_t	0.24 [118]
ν_{21}, ν_{12}	0.35 [119]
d_{31}	21E-12 C/N [34]
κ	1
Estimated	5.67 mV/N

Results and discussion

Validation of the PVDF sensor-based force measurement system is performed using two approaches as follows: 1) *Backward Comparison*: the independently measured *dynamometer force signal* is taken as the *true force signal*, which is then fed into the measurement system (see Figure. 3). The output of the system, called the *reference signal*, is the signal expected from the PVDF sensors. If the proposed models for the force measurement system are valid, the *reference signal* should match the magnitude and shape of the *in-situ measured PVDF sensor signal*; 2) *Forward Comparison*: this involves comparing the *dynamometer force signal* directly with *the force signal back calculated from the in-situ measured PVDF sensor signal* using Eq. (25).

Backward comparison

Representative results from the backward comparison are shown in Figure. 10 to Figure.

13.

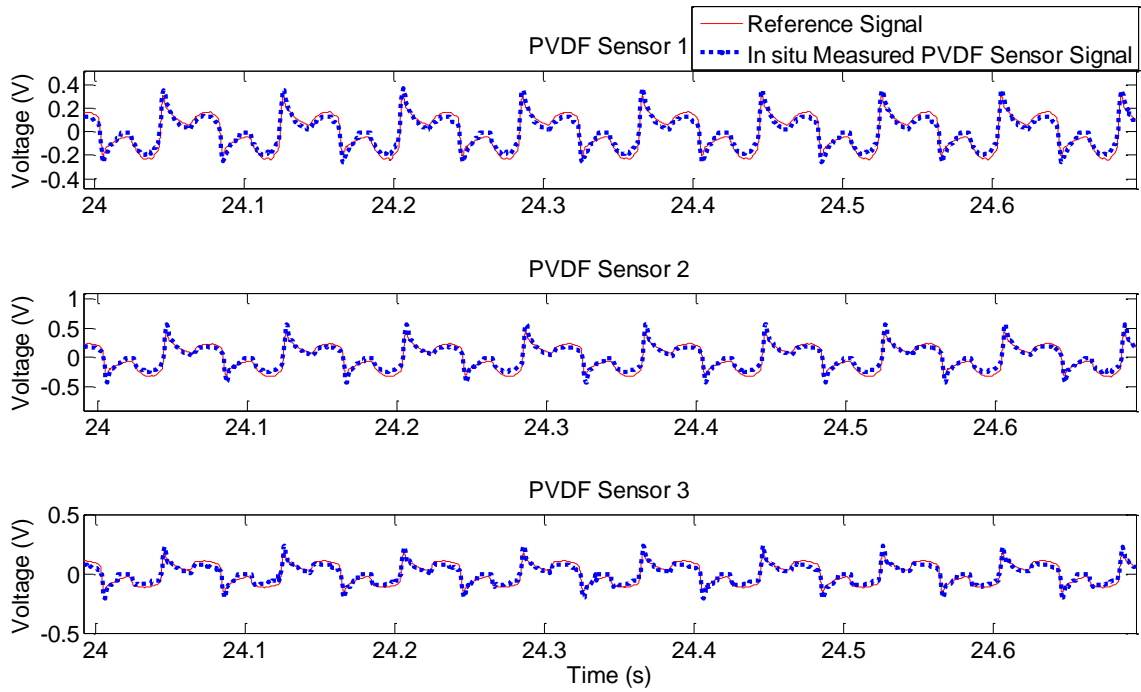


Figure. 10. Backward comparison between the reference signal and the in-situ measured PVDF sensor signal (Cutting Test No. 1).

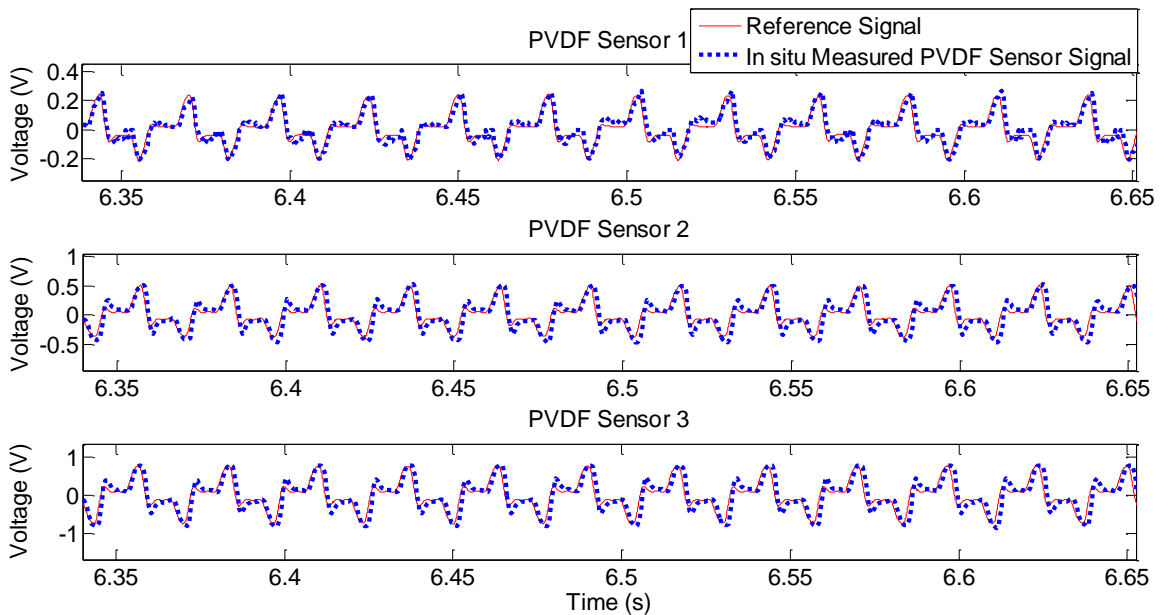


Figure. 11. Backward comparison between the reference signal and the in-situ measured PVDF sensor signal (Cutting Test No. 10).

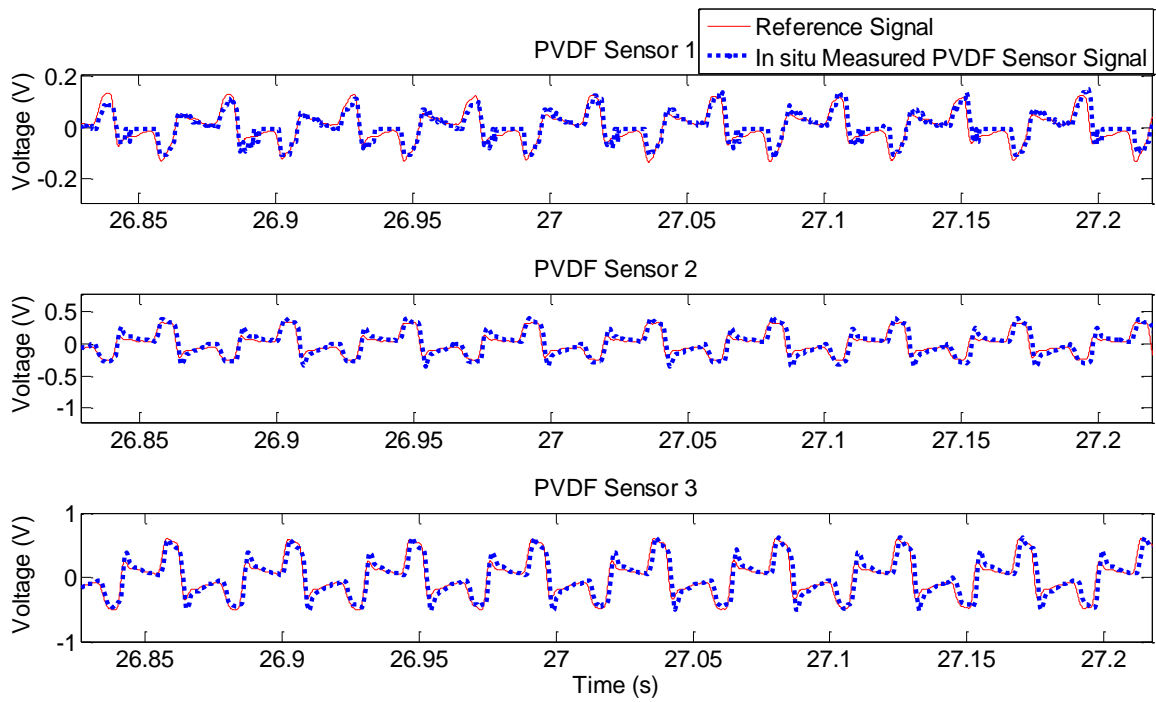


Figure. 12. Backward comparison between the reference signal and the in-situ measured PVDF sensor signal (Cutting Test No. 15).

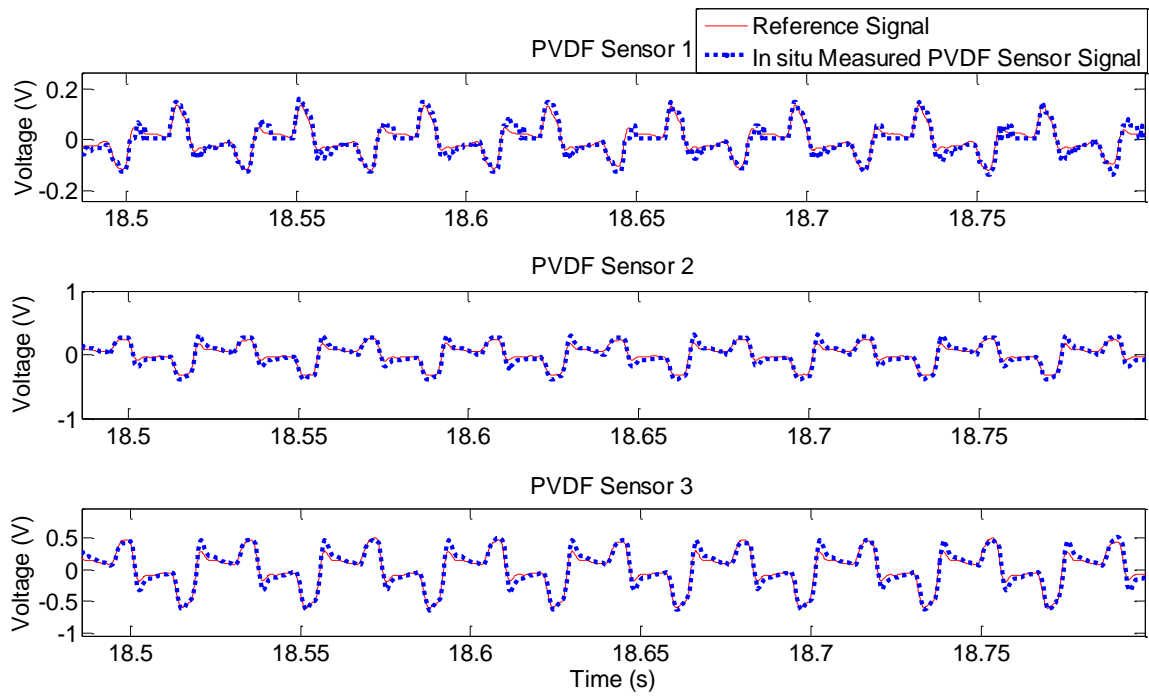


Figure. 13. Backward comparison between the reference signal and the in-situ measured PVDF sensor signal (Cutting Test No. 17).

It can be seen from Figures. 8-11 that there is close agreement in both the shape and magnitude of the *reference signal* and the *in-situ measured PVDF sensor signal*, which validates the models of the measurement system proposed in this chapter. It is also clear that the scaling coefficient K_s (listed in Table 1) is largely unchanged across the different cutting conditions and workpiece materials. This is expected since nothing was assumed about the cutting conditions and the workpiece material in developing the physics based models. It should be noted that, the *in-situ* measured PVDF sensor signal is an attenuated and distorted version of the linear combination of the three cutting force components and should not be confused with a specific force component. In applications where the DC component and the exact shape of a particular force component are not required, the *in-situ measured PVDF sensor signals* are still useful. Examples of such applications include chatter detection, tool wear monitoring and tool breakage detection.

It is also noted that the experimentally obtained K_s (listed in Table 1) is of the same order of magnitude as the estimated value given in Table 2, but is approximately 32% smaller. This again validates the models represented by Eqs. (22) and (24). It is expected that if more reliable values of the material constants are available *a priori*, better agreement between the experimentally determined and the estimated K_s can be achieved.

Forward comparison

In applications where the exact magnitude and shape of the force components are required, the *in-situ* measured PVDF sensor signal is not sufficient. In order to compensate for the distortion introduced by the signal conditioning circuitry and to recover the original magnitude and shape of the force signal, a discrete Finite Impulse Response

(FIR) compensation filter is introduced, as shown in Figure. 14. The continuous time transfer function of the charge amplifier filter ($G_C(s)$) and the anti-aliasing filter ($G_{AA}(s)$), have to be discretized into $G_C(z)$ and $G_{AA}(z)$, respectively, using the zero-order hold transformation method.

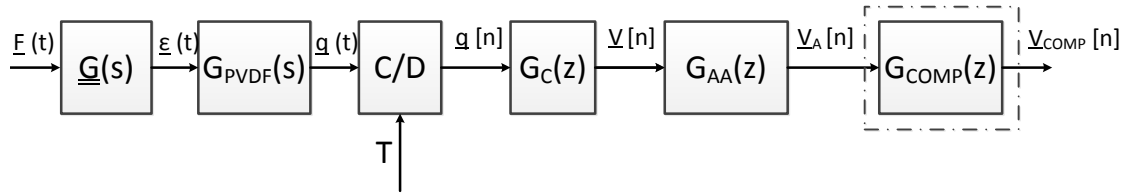


Figure. 14. Discrete time compensation of attenuation and distortion introduced by the signal conditioning circuitry.

If we define

$$G(z) = G_C(z)G_{AA}(z) \quad (29)$$

and let $g(n)$ be the inverse z-transform of $G(z)$, a least squares inverse FIR filter $h(n)$ can be designed [121] such that

$$g(n) * h(n) \approx \delta(n - n_d) \quad (30)$$

where $*$ denotes the convolution operation, $\delta(n)$ is the unit impulse function and n_d is the integer sample delay in the discrete time domain. $G_{COMP}(z)$ is then simply the z -transform of $h(n)$. It is noted here that a simple inversion of $G(z)$ is not possible because $G(z)$ has a zero at 0 Hz. The forward comparison can then be performed between the *force signal calculated from the PVDF sensor signals using Eq. (25)* and the *independently measured dynamometer force signal*. Representative results for the feed (F_y) and transverse (F_x) forces are shown in the Figures. 13-14.

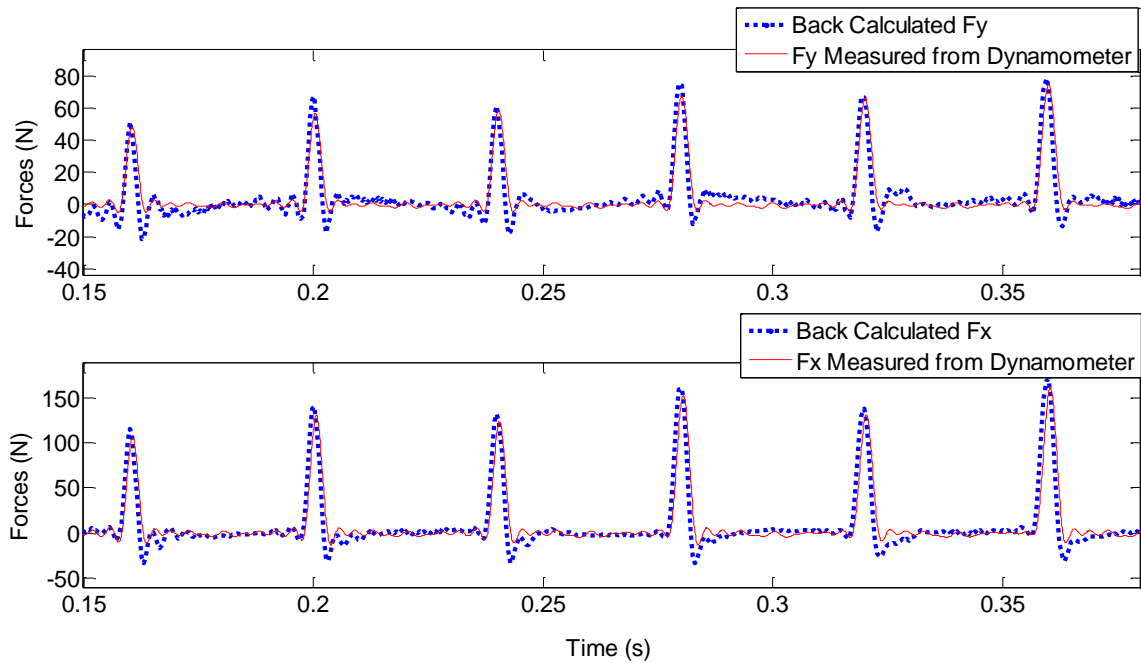


Figure. 15. Forward comparison between the forces calculated from the PVDF sensor signals and the dynamometer measurements (Cutting Test No. 1: tool entry stage of cutting).

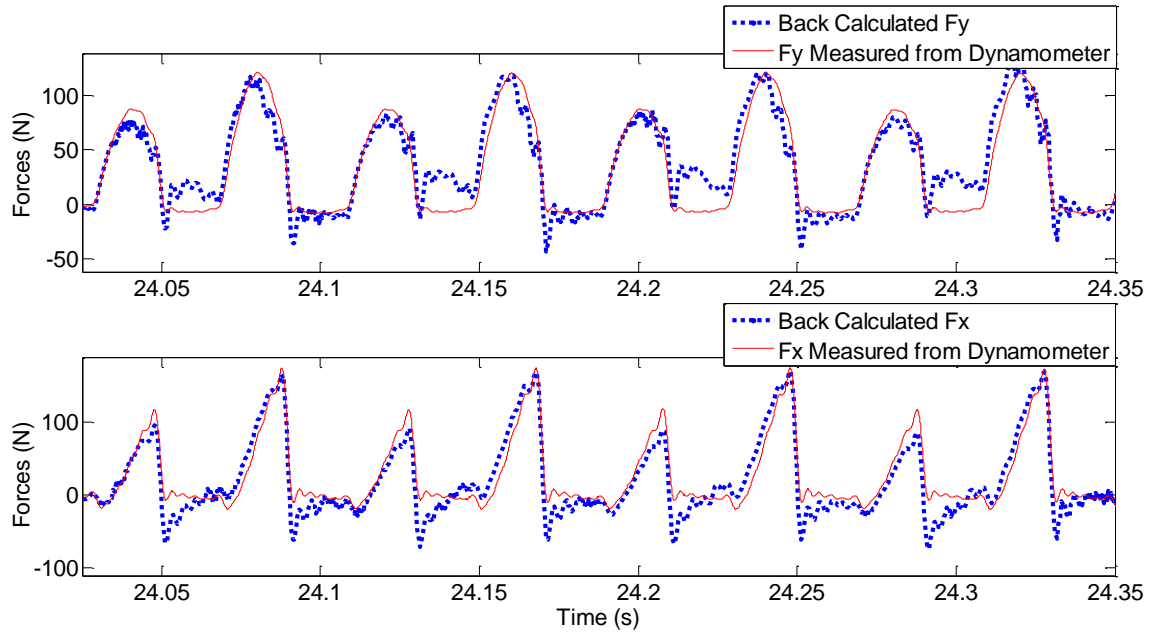


Figure. 16. Forward comparison between the forces calculated from the PVDF sensor signal and the dynamometer measurements (Cutting Test No. 1: stable cutting stage).

It can be seen from Figures 13 and 14 that the FIR compensation filter helped to restore the PVDF sensor signals to their “reference” form at the expense of extra computation and delay (n_d samples) introduced in the discrete time domain. To better compare the *force signal calculated from the PVDF sensor signals* and the *independently measured dynamometer force signals*, the delay is not shown in Figures. 13 and 14. Also, the *dynamometer force signal measured from dynamometer* was downsampled so that its cutoff frequency matches that of the PVDF sensor signal. Reasonable agreement between the forces back calculated from the PVDF sensor signals and the dynamometer measurements is achieved, except where sharp transitions occur in the force signals, e.g. when the cutter enters/exits the workpiece. The oscillations observed in these transition regions can be explained by the Gibbs phenomenon, which can be suppressed by further increasing the sampling rate of the PVDF sensor-based force measurement system to

cover higher order harmonics of the tooth passing frequency. Increasing the signal-to-noise ratio (SNR) of the force measurement system will also help in bringing the two signals closer to each other. The agreement between the two signals is better at the tool entry stage of cutting than in the stable cutting stage. This can be explained by the fact that due to longer engagement time per spindle period, the low frequency content, especially the DC content, contributes more to the cutting force during stable cutting than it does during the tool entry stage. Since the low frequency content is attenuated by the signal conditioning circuitry yet not perfectly compensated, the discrepancy between the two signals is larger at the stable cutting stage.

The systematic discrepancy between the dynamometer force signal and the PVDF sensor signal as seen in Figure. 16 is thought to be due to the imperfect compensation by the FIR filter. To be specific, the FIR filter needs to have a very large magnitude response around 0 Hz to compensate for the attenuation caused by the charge amplifier. Therefore the noise in the PVDF sensor signal and the discrepancy between the two signals in the backward comparison around 0 Hz will be significantly amplified by the FIR filter during compensation, leading to the increased discrepancy in forward comparison. This argument can be seen in Figure. 17 between 0-15Hz and it also explains why the discrepancy is larger when the cutting tool is out of cut, i.e. when the signal to noise ratio is small.

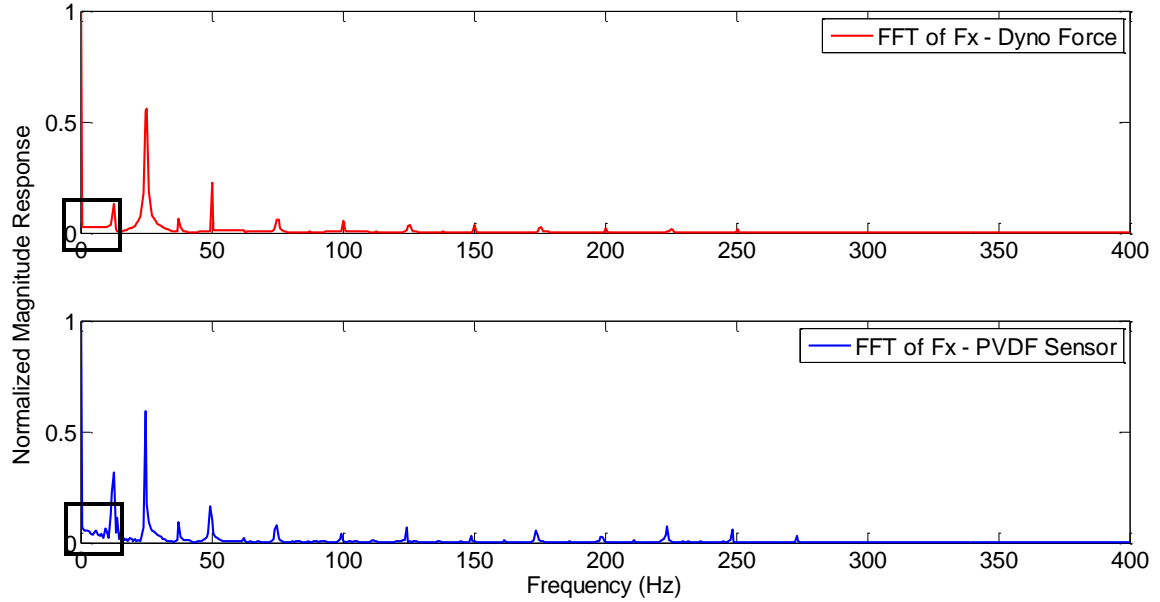


Figure. 17 Comparison of the Dynamometer Force (F_x) and PVDF Sensor Based Force (F_x) in Frequency Domain

Using an Analog-to-Digital Converter (ADC) with a higher number of bits will help reduce the quantization noise (the ADC used in this test has 10 bits). If the behavior of the PVDF sensor noise and backward discrepancy around 0 Hz can be well understood, filters can be designed to attenuate the noise before the compensation. In addition, if the behavior of the after-compensation discrepancy can be shown to be consistent, it can also be removed by filtering. However, the application of additional filters may lead to larger latency.

For off-line data processing, a FIR filter with optimal delay (n_d) can be found to minimize the difference between the two sides of Eq. (30) [121]. For on-line applications, however, n_d is usually bound by the allowable latency.

Summary

A novel, low cost and non-intrusive method for monitoring the cutting forces in

the peripheral end milling process has been proposed, implemented and validated. The methodology takes advantage of a low cost PVDF sensor which offers a unique combination of high flexibility, wide bandwidth, fast response, high dynamic range, high strain sensitivity and differential sensitivity along the different geometric axes. Physics based models have been developed to relate the PVDF sensor signal to the cutting forces in end milling. High fidelity PVDF signals were acquired using an in-house developed data logging unit and were found to compare well with the force signals measured from a piezoelectric platform dynamometer. When the exact values of the material constants of the cutting tool and the PVDF sensor are known, they can be used directly in Eq.(26) to calculate K_s , which can then be used to transform PVDF sensor signals into cutting force signals independently of the workpiece material. In this case, no calibration of K_s is needed for the measurement system to function. In this work, the PVDF sensor signal is calibrated against the dynamometer force signal. The PVDF sensor signal represents a slightly distorted version of the cutting force signal and is useful in applications where only the AC content of the cutting forces is of interest. A least squares FIR filter was introduced in the discrete time domain in order to recover the original form of the cutting force signals. So long as the frequency content of the cutting force signal lies within the bandwidth of the measurement system and the attenuation and distortion introduced by the signal conditioning circuitry in the low frequency range are appropriately compensated, the cutting force can be accurately measured. Future work will include improving the measurement system to better capture the original shape of the force signals, incorporating wireless functionality into the measurement system for real time data acquisition and extending the methodology to other rotating tool machining

processes such as drilling.

CHAPTER 4 DESIGN OF PVDF SENSOR ROSETTE FOR STRAIN ISOLATION

Introduction

In this chapter, three types of PVDF sensor rosettes for isolation of bending strain, shear strain and axial strain are proposed for: (1) isolating the strain component of interest under complex loading, and (2) compensating thermal strains and pyroelectric effect due to changes in temperature. Complete models for the PVDF sensor and rosettes are derived from first principles, incorporating all physical behaviors of a PVDF sensor, namely, electro-mechanical coupling, thermal expansion and pyroelectric effect. Experimental results are then presented for validation of the proposed PVDF rosette designs and the corresponding models and for comparison with their MFSG counterparts. The work presented in this chapter has also been reported in the author's paper [122].

Modeling of PVDF Sensor Rosettes

Output of individual PVDF sensor when subjected to in-plane deformation

The voltage output of a single PVDF sensor when subjected to in-plane deformation is first derived. First, the constitutive model of the PVDF sensor needs to be considered in order to relate the strain to charges generated in the PVDF sensor electrodes. The linear constitutive model shown in Eq. (31) [123] will suffice since only small strains and temperature change are assumed to occur.

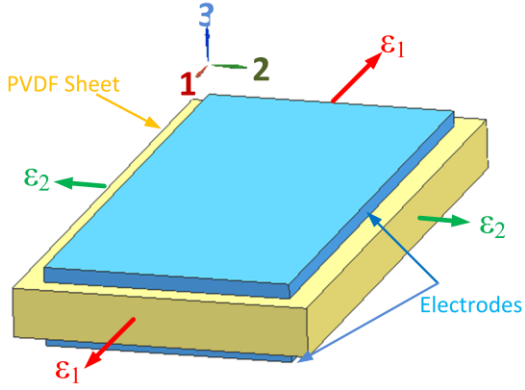


Figure. 18. Schematic of a PVDF sensor element.

$$\begin{bmatrix} D \\ \varepsilon \end{bmatrix} = \begin{bmatrix} e^\sigma & d \\ d^T & s^E \end{bmatrix} \begin{bmatrix} E \\ \sigma \end{bmatrix} + \Delta T \begin{bmatrix} p^\sigma \\ \alpha \end{bmatrix} \quad (31)$$

The piezoelectric modulus matrix, d , has the following form:

$$d = \begin{bmatrix} 0 & 0 & 0 & 0 & d_{15} & 0 \\ 0 & 0 & 0 & d_{24} & 0 & 0 \\ d_{31} & d_{32} & d_{33} & 0 & 0 & 0 \end{bmatrix} \quad (32)$$

where element d_{kj} relates the electric displacement in the k th direction to the mechanical stress in the j th direction. For a thin film piezoelectric sheet, the poling direction is typically in the thickness direction, denoted as axis 3 in Figure. 18. Axes 1 and 2 are referred to the drawn and transverse axes, respectively.

When a PVDF piezoelectric element is used as a sensor, there is no externally applied electric field ($E \approx 0$), consequently

$$\begin{bmatrix} D_1 \\ D_2 \\ D_3 \end{bmatrix} = \begin{bmatrix} 0 & 0 & 0 & 0 & d_{15} & 0 \\ 0 & 0 & 0 & d_{24} & 0 & 0 \\ d_{31} & d_{32} & d_{33} & 0 & 0 & 0 \end{bmatrix} \begin{bmatrix} \sigma_1 \\ \sigma_2 \\ \sigma_3 \\ \sigma_4 \\ \sigma_5 \\ \sigma_6 \end{bmatrix} + \Delta T \begin{bmatrix} p_1^\sigma \\ p_2^\sigma \\ p_3^\sigma \end{bmatrix} \quad (33)$$

It is clear from Eq. (33) that the shear stress in the 1-2 plane, σ_6 , does not contribute to any electric displacement because d_{i6} ($i=1,2,3$) is zero. In the 1-2 plane, the PVDF sensor shows sensitivity to only normal stresses that are aligned with axes 1 and 2 of the PVDF sensor.

The electric charges generated in the electrodes by the mechanical stresses are then found as:

$$q = \int (D_1 dA_1 + D_2 dA_2 + D_3 dA_3) \quad (34)$$

In practice, a PVDF sensor has electrodes only in the 1-2 plane. Therefore, A_1 and A_2 vanish from Eq. (34) to yield:

$$q = \int D_3 dA_3 \quad (35)$$

The PVDF element can be treated as orthotropic material after being poled, with the symmetry axes parallel to the geometric axes 1 and 2 shown in Figure. 18. Owing to the small thickness of the PVDF sensor, it can be assumed that the sensor is in a state of plane stress, i.e., $\sigma_3=\sigma_4=\sigma_5=0$. Consequently, the stress-strain-temperature relations of the PVDF sensor can be written as (with $E = 0$):

$$\begin{bmatrix} \varepsilon_1 \\ \varepsilon_2 \\ \varepsilon_6 \end{bmatrix} = \begin{bmatrix} \frac{1}{Y_1} & \frac{-\nu_{21}}{Y_2} & 0 \\ \frac{-\nu_{12}}{Y_1} & \frac{1}{Y_2} & 0 \\ 0 & 0 & \frac{1}{Y_6} \end{bmatrix} \begin{bmatrix} \sigma_1 \\ \sigma_2 \\ \sigma_6 \end{bmatrix} + \Delta T \begin{bmatrix} \alpha_1 \\ \alpha_2 \\ \alpha_6 \end{bmatrix} \quad (36)$$

where ν_{kj} is the Poisson's ratio between axes k and j and represents the contribution to the normal strain along axis j from the normal strain along axis k ; σ_1 and σ_2 can then be written as:

$$\sigma_1 = \frac{Y_1[(\varepsilon_1 - \alpha_1 \Delta T) + \nu_{21}(\varepsilon_2 - \alpha_2 \Delta T)]}{1 - \nu_{21}\nu_{12}} \quad (37)$$

and

$$\sigma_2 = \frac{Y_2[(\varepsilon_2 - \alpha_2 \Delta T) + \nu_{12}(\varepsilon_1 - \alpha_1 \Delta T)]}{1 - \nu_{21}\nu_{12}} \quad (38)$$

Combining Eqs. (33), (35), (37) and (38), the total charge q generated by the PVDF sensor is given by:

$$q = \frac{\int [(\varepsilon_1 - \alpha_1 \Delta T)(d_{31}Y_1 + \nu_{12}d_{32}Y_2) + (\varepsilon_2 - \alpha_2 \Delta T)(d_{32}Y_2 + \nu_{21}d_{31}Y_1) + p_3^\sigma \Delta T(1 - \nu_{21}\nu_{12})] dA_3}{1 - \nu_{21}\nu_{12}} \quad (39)$$

where A_3 is the area of the electrodes of the PVDF sensor. Finally, the magnitude of the voltage output V is given by

$$V = \frac{q}{C_F} \quad (40)$$

where C_F is the capacitance of the PVDF sensor when a voltage amplifier is used to interface with the PVDF sensor or the feedback capacitance when a charge amplifier is used [124].

If we assume that the PVDF sensor is securely bonded to the host structure, then the strain field in the sensor is the same as that experienced by the host structure. Due to the small thickness ($\sim 30 \mu\text{m}$) and low Young's modulus of the PVDF sensor ($Y_1, Y_2 \approx$

5GPa) [34], it can be assumed that the elastic deformation and thermal expansion of the host structure is unaffected by the sensor. By applying the compatibility condition at the sensor-host structure interface, we get

$$\begin{aligned}\varepsilon_1 &= \varepsilon_{1,h} + \alpha_{1,h}\Delta T_h \\ \varepsilon_2 &= \varepsilon_{2,h} + \alpha_{2,h}\Delta T_h\end{aligned}\tag{41}$$

where $\varepsilon_{i,h}$ and $\alpha_{i,h}$ are the elastic strain seen by the host structure and the coefficient of thermal expansion (CTE) of the host structure along the i^{th} axis ($i = 1, 2$) of the PVDF sensor, respectively. ΔT_h denotes the average temperature change in the host structure.

It is clear from Eq. (39) that when a single PVDF sensor is used, both the axial strain ε_1 and the transverse strain ε_2 contribute to the voltage output. In applications where only a particular strain component is of interest, multiple PVDF sensors or a sensor rosette must be used to separate the desired strain component from the rest. Three sensor rosette designs for isolating the bending strain, shear strain and axial strain, respectively, are discussed in the following sections.

PVDF rosette for isolation of bending strain

To eliminate the sensitivity of the PVDF sensors to axial and shear strains, the bending strain rosette shown in Figure. 19 can be used. The voltage output of the rosette is obtained from the individual sensor outputs as follows:

$$V = V_1 - V_4 + V_3 - V_2 \quad (42)$$

where V_i is the voltage output of the i th sensor. Assuming that the material properties and electrical constants of the four PVDF sensors in the rosette (i.e. d_{31} , d_{32} , ν_{12} , ν_{21} , Y_1 , Y_2 , α_1 , α_2 , p_3^σ , A_3 , C_F) are the same, and letting $\varepsilon_{1,i}$ and $\varepsilon_{2,i}$ denote strains along axis 1 and axis 2 in sensor i , Eq. (42) may be rewritten by substituting in Eqs (39) and (40) for q and V , respectively:

$$V = \frac{1}{(1-\nu_{21}\nu_{12})C_F} \int \left\{ \begin{aligned} &(d_{31}Y_1 + \nu_{12}d_{32}Y_2) \sum_{i=1}^4 (-1)^{i+1} (\varepsilon_{1,i} - \alpha_1 \Delta T_i) + \\ &(d_{32}Y_2 + \nu_{21}d_{31}Y_1) \sum_{i=1}^4 (-1)^{i+1} (\varepsilon_{2,i} - \alpha_2 \Delta T_i) + \sum_{i=1}^4 (-1)^i p_3^\sigma \Delta T_i (1 - \nu_{21}\nu_{12}) \end{aligned} \right\} dA_3 \quad (43)$$

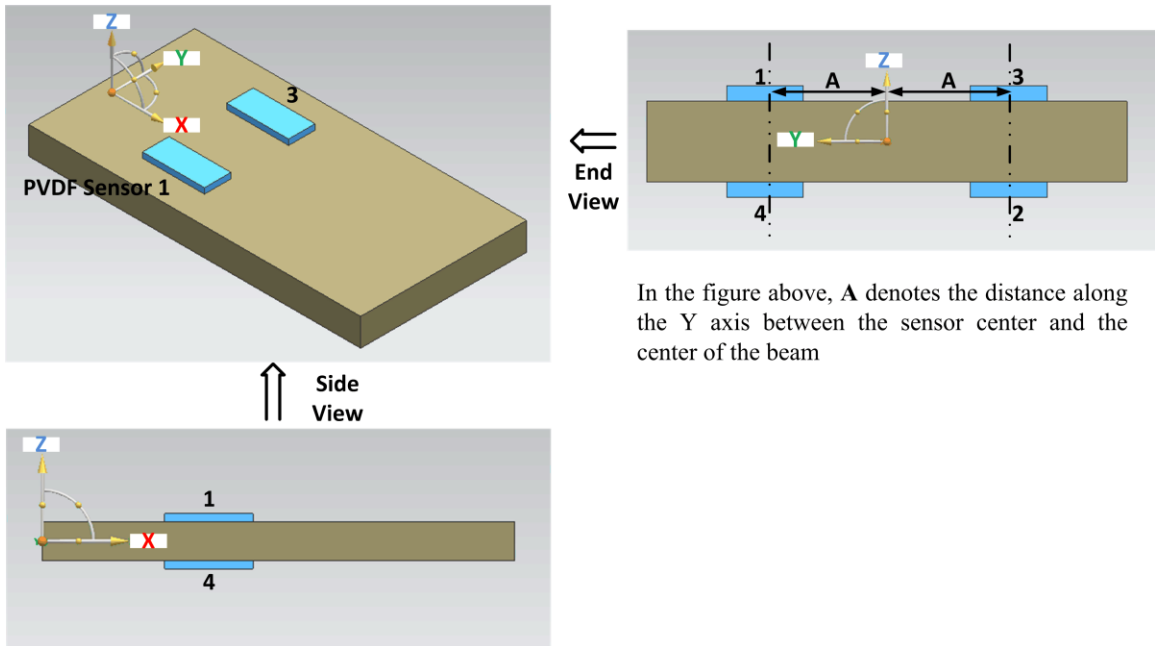


Figure. 19. PVDF sensor rosette for isolation of bending strain on a rectangular beam.

For small deformation, the total strain experienced by a structure is the superposition of strains caused by all deformation modes, i.e., bending, axial deformation, shear deformation and thermal expansion. The shear strain in the XY plane is not picked up by the PVDF sensor due to vanishing of d_{i6} ($i=1,2,3$) and is therefore no longer considered. Due to symmetry, the axial strains in the X/Y direction cancel out when $\varepsilon_{1/2,2}$ and $\varepsilon_{1/2,4}$ are subtracted from $\varepsilon_{1/2,3}$ and $\varepsilon_{1/2,1}$, respectively. The bending strain due to flexure about the neutral plane in XZ vanishes when adding $\varepsilon_{1/2,1}$ and $\varepsilon_{1/2,2}$ to $\varepsilon_{1/2,3}$ and $\varepsilon_{1/2,4}$, respectively. Therefore, only the bending strain caused by flexure about the neutral plane in XY and the thermal strain need to be considered. For these two deformation modes,

$$\begin{aligned}\varepsilon_{1,i} &= \varepsilon_{h,i} + \alpha_{1,h} \Delta T_h \\ \varepsilon_{2,i} &= -\nu_h \varepsilon_{h,i} + \alpha_{2,h} \Delta T_h\end{aligned}\tag{44}$$

where $\varepsilon_{h,i}$ is the bending strain in the host structure at the location of sensor i . Due to symmetry

$$\varepsilon_{h,1} = \varepsilon_{h,3} = -\varepsilon_{h,2} = -\varepsilon_{h,4} = \varepsilon_h\tag{45}$$

With Eqs (44) and (45), and assuming

$$\Delta T_1 = \Delta T_4 \quad \Delta T_2 = \Delta T_3 \quad (46)$$

Eq. (43) reduces to

$$V = \frac{4[d_{31}Y_1(1-\nu_h\nu_{21}) + d_{32}Y_2(\nu_{12} - \nu_h)]}{(1-\nu_{21}\nu_{12})C_F} \varepsilon_h A_3 \quad (47)$$

It is interesting to note that depending on the relative magnitudes of ν_{12} and ν_h , the transverse sensitivity of the PVDF sensor rosette (due to d_{32}) could either increase or decrease the overall sensitivity of the rosette to the bending strain. Also, in cases where ν_{12} and ν_h are very close, Eq. (47) can be further simplified by dropping the $d_{32}Y_2(\nu_{12} - \nu_h)$ term. The pyroelectric effect and the thermal strain do not appear in Eq. (47) under the assumption that the temperature change seen by sensors 1 and 2 are the same as that seen by sensors 4 and 3, respectively. The reasonableness of this assumption depends on the distance between the sensors and the sensor size.

Application of the bending strain rosette is not limited to a rectangular beam. Eq. (47) is applicable for any host structure where the symmetry between sensors 1 and 3, 2 and 4, 1 and 4, 2 and 3 is satisfied. For example, the bending strain in a circular cross section beam can be measured using the two configurations illustrated in Figure. 20. Note that both configurations measure the bending strain due to flexure about the

XZ neutral plane. Configuration (a) maximizes the temperature compensation performance because sensors 1 and 2 are close to sensors 4 and 3, respectively. However, the sensitivity of the rosette is low because all four sensors are close to the neutral plane. On the other hand, configuration (b) maximizes the overall sensitivity to bending strain at the cost of limited temperature compensation since sensors 1 and 2 are far apart from sensors 4 and 3, respectively.

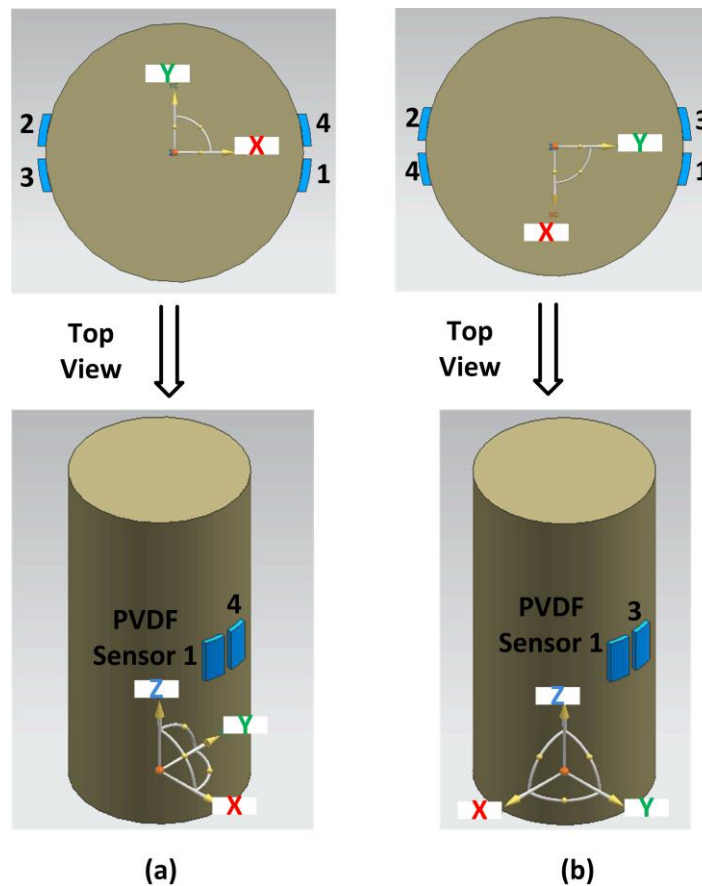


Figure. 20. Two bending strain PVDF rosette configurations on a circular beam.

It is also noted that the bending strain rosette described in this section is not limited to PVDF sensors. Any piezoelectric material could be used instead of the PVDF

polymer, except under the extreme condition: $\nu_h \gg \nu_{I2}$ and $(1 - \nu_h \nu_{I2}) \approx (\nu_h - \nu_{I2})$. In this case, the overall sensitivity is significantly offset by the transverse sensitivity term. However, this is rare for host structures made of isotropic materials whose Poisson's ratio is bound by 0.5.

PVDF rosette for isolation of shear strain

To isolate the shear strain in a circular shaft subjected to complex loading, the PVDF strain gauge rosette shown in Figure. 21 can be used. Individual sensor outputs are combined to form the rosette output according to Eq. (43). Axial strains, if present, cancel out when $\varepsilon_{1/2,2}$ and $\varepsilon_{1/2,4}$ are subtracted from $\varepsilon_{1/2,3}$ and $\varepsilon_{1/2,1}$, respectively. Because sensors 1 and 2 are diametrically opposite to sensors 3 and 4, respectively, bending strains are eliminated when $\varepsilon_{1/2,1}$ and $\varepsilon_{1/2,2}$ are added to $\varepsilon_{1/2,3}$ and $\varepsilon_{1/2,4}$, respectively.

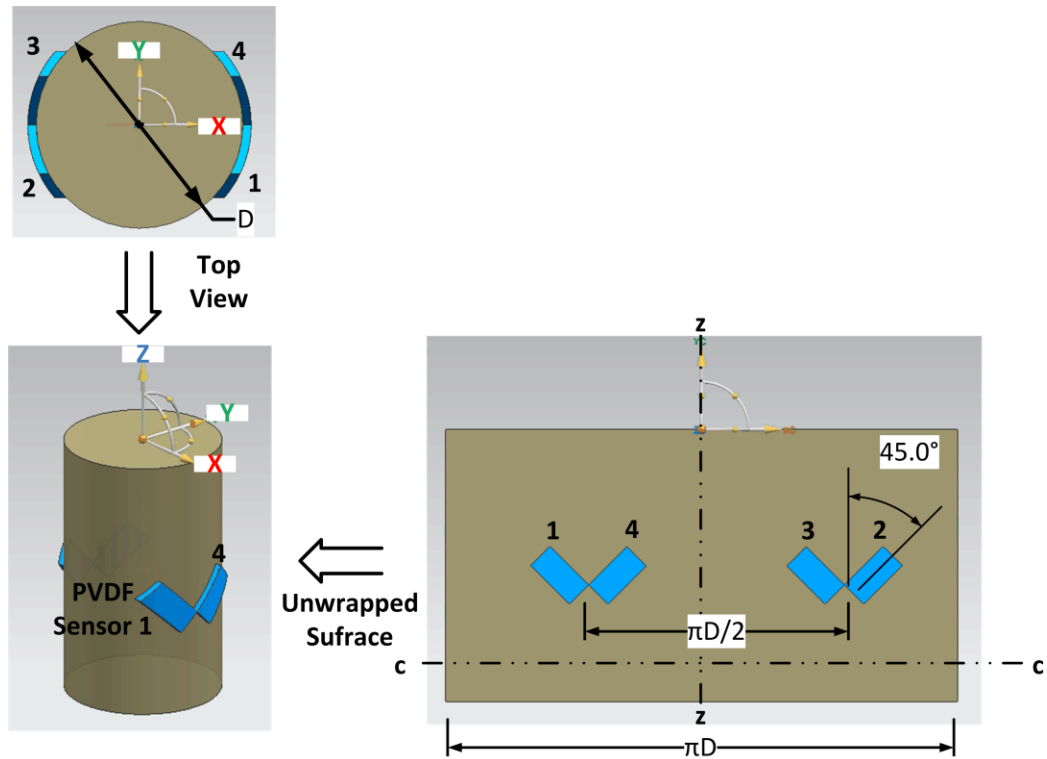


Figure. 21. PVDF sensor rosette for isolation of shear strain on a circular shaft.

The only strain components left to be considered are the shear strain and thermal strains. If the engineering shear strain caused by shear deformation is denoted by γ , the strains along the axes 1 and 2 of the PVDF sensors can be found from Mohr's strain circle (see Figure. 22) as follows:

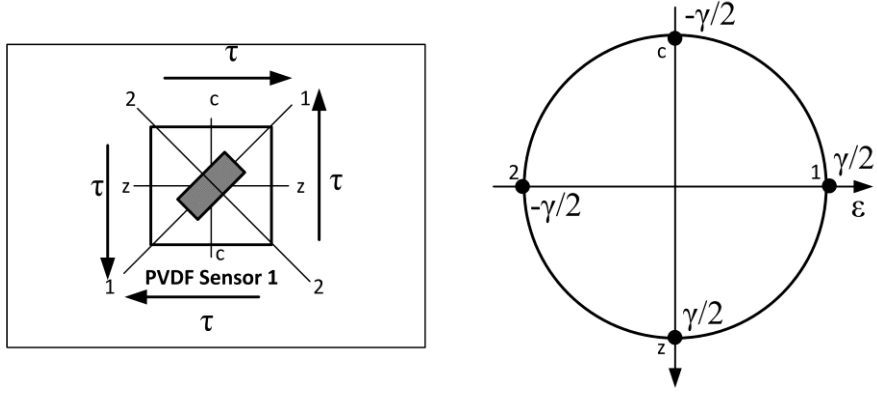


Figure. 22. Mohr's strain circle for shear strain transformation.

$$\begin{aligned}
 \varepsilon_{1,1} = \varepsilon_{1,3} = \varepsilon_{2,2} = \varepsilon_{2,4} &= \gamma/2 + \alpha_{1,h} \Delta T_h \\
 \varepsilon_{2,1} = \varepsilon_{2,3} = \varepsilon_{1,2} = \varepsilon_{1,4} &= -\gamma/2 + \alpha_{2,h} \Delta T_h
 \end{aligned}
 \tag{48}$$

Here $\alpha_{i,h}$ ($i = 1, 2$) stands for the coefficient of thermal expansion (CTE) of the host structure along axis i of sensor 1. With Eq. (48), and assuming Eq. (46) is true, Eq. (43) simplifies to

$$V = \frac{[d_{31}Y_1(1-\nu_{21}) - d_{32}Y_2(1-\nu_{12})]}{(1-\nu_{21}\nu_{12})C_F} [2\gamma + 2\Delta T_h(\alpha_{1,h} - \alpha_{2,h})] A_3 \tag{49}$$

It can be seen that the pyroelectric effect vanishes under the assumption in Eq. (46) (which is reasonable since sensors 1 and 2 are very close to sensors 4 and 3, respectively). The thermal strain, on the other hand, remains in Eq. (49) when the host structure is not homogeneous and isotropic, i.e., the CTE differs between directions 1 and 2. For host

structure materials that are homogeneous and isotropic, $\alpha_{1,h} = \alpha_{2,h}$, the thermal strain term vanishes and only the shear strain γ is left. It can also be seen that the transverse sensitivity of the PVDF sensor (d_{32}) can only decrease the shear strain sensitivity of the rosette. In the extreme case where $d_{31}Y_1(1-\nu_{21})$ equals $d_{32}Y_2(1-\nu_{12})$, the rosette completely loses its sensitivity. Fortunately, in the case of the PVDF sensor, d_{32} is typically one order of magnitude lower than d_{31} [34]. This is not generally true for other piezoelectric sensors. For example, in the case of PZT, d_{32} is almost equal to d_{31} [34], making it inappropriate for shear strain measurement.

The application of the shear strain PVDF rosette is not limited to circular shafts. It is applicable wherever the symmetry between sensor pairs 1, 4 and 2, 3 are satisfied while the antisymmetry between sensor pairs 1, 3 and 2, 4 are maintained. Some examples are given in Figure. 23, where two varieties of shear strain PVDF rosettes are used to measure the torque applied on a cruciform shaft (left) and a square shaft (right), respectively [125].

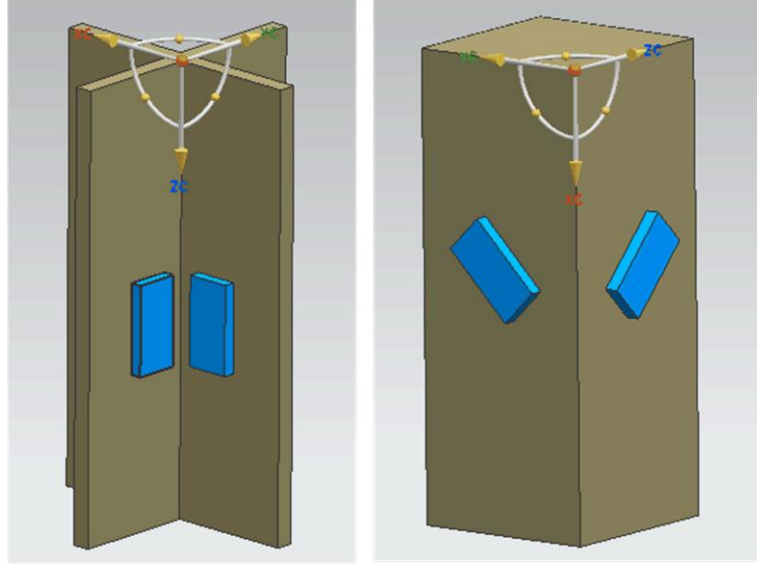


Figure. 23. PVDF sensor rosette for isolation of shear strain.

PVDF rosette for isolation of axial strain

Similar to the previous two scenarios, the axial strain can be isolated from other strain components (i.e. bending strain, shear strain and thermal strain) using the rosette design shown in Figure. 24. Eq. (43) can be applied to relate the voltage output of the rosette to the axial strain experienced by the host structure. Due to symmetry, the bending strains caused by flexure about the neutral plane in XY are canceled by adding $\varepsilon_{1/2,1}$ and $\varepsilon_{1/2,2}$ to $\varepsilon_{1/2,3}$ and $\varepsilon_{1/2,4}$, respectively. The bending effect caused by flexure about the neutral plane in XZ is removed when all four sensors are located on the centerline of the host structure. If the axial strain in the host structure is ε_h , then

$$\begin{aligned} \varepsilon_{1,1} = \varepsilon_{1,3} = \varepsilon_{2,2} = \varepsilon_{2,4} &= \varepsilon_h + \alpha_{1,h} \Delta T_h \\ \varepsilon_{2,1} = \varepsilon_{2,3} = \varepsilon_{1,2} = \varepsilon_{1,4} &= -\varepsilon_h \nu_h + \alpha_{2,h} \Delta T_h \end{aligned} \quad (50)$$

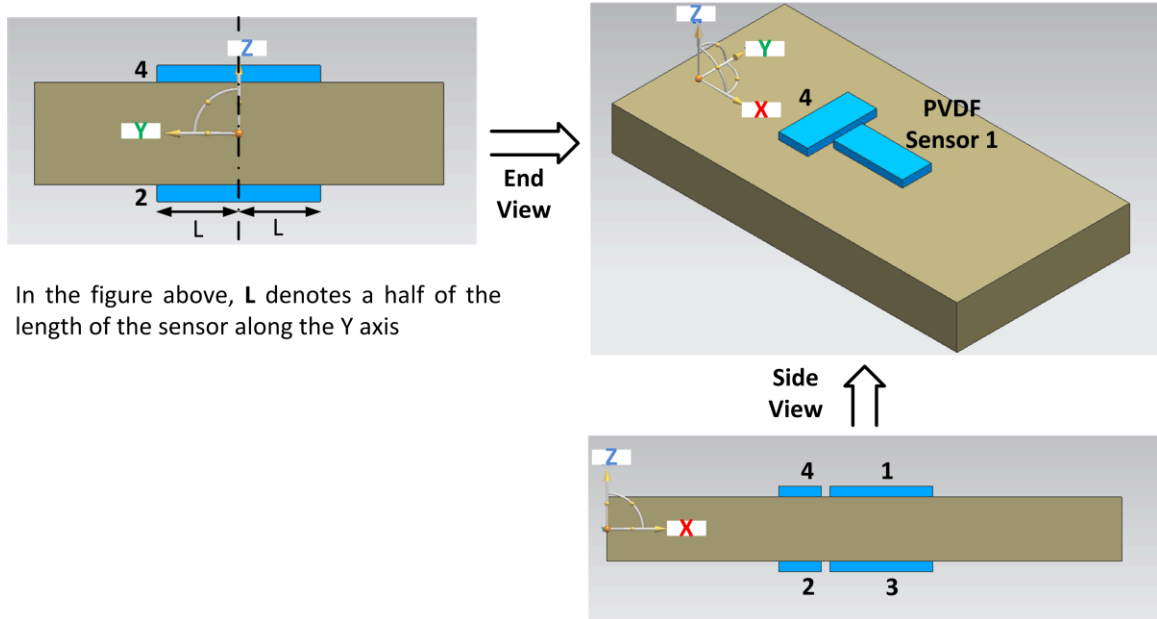


Figure. 24. PVDF sensor rosette for isolation of axial strain.

Substituting Eq. (50) into Eq. (43), we get

$$V = \frac{[d_{31}Y_1(1-\nu_{21}) - d_{32}Y_2(1-\nu_{12})]}{(1-\nu_{21}\nu_{12})C_F} [2\varepsilon_h(1+\nu_h) + 2\Delta T_h(\alpha_{1,h} - \alpha_{2,h})] A_3 \quad (51)$$

Similar to the shear strain isolation described in the previous section, the pyroelectric effect completely vanishes while the thermal strain remains when the host structure is not homogeneous and isotropic. The transverse sensitivity of the PVDF sensor (d_{32}) tends to decrease the overall sensitivity of the rosette to axial strain. Therefore, piezoelectric materials with d_{32} close to d_{31} (such as PZT) should be avoided. It is also noted that the application of the axial strain PVDF rosette is not limited to rectangular bars. As long as

there is symmetry between sensors 1 and 3, and sensors 2 and 4 (e.g. circular bar, cruciform bar), the axial strain rosette is applicable.

Comparison of PVDF rosettes and MFSG rosettes

It should be noted that for each PVDF sensor rosette discussed, there is a traditional MFSG counterpart. When an unbalanced full Wheatstone bridge is used with the MFSGs, the bridge output is approximately proportional to the isolated strain component of interest: (as shown in Figure. 25)

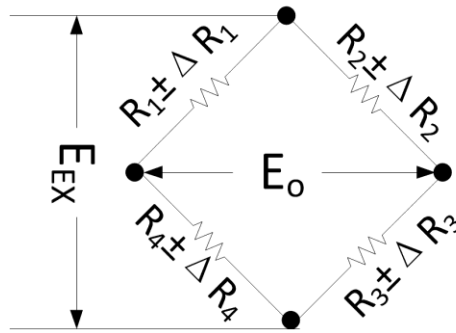


Figure. 25. Schematic of an unbalanced Wheatstone full bridge.

$$E_o = \left(\frac{R_4}{R_1 + R_4} - \frac{R_3}{R_2 + R_3} \right) E_{EX} = f(R_1, R_2, R_3, R_4) E_{EX} \quad (52)$$

In general, E_o is a non-linear function of R_i ($i = 1,2,3,4$) and the change in E_o is a nonlinear function of ΔR_i ($i = 1,2,3,4$). When change in R_i due to strain is small, the change in E_o may be approximated as

$$\partial E_o \approx \frac{\partial f}{\partial R_1} \Delta R_1 + \frac{\partial f}{\partial R_2} \Delta R_2 + \frac{\partial f}{\partial R_3} \Delta R_3 + \frac{\partial f}{\partial R_4} \Delta R_4 \quad (53)$$

where

$$\begin{aligned} \frac{\partial f}{\partial R_1} &= E_{EX} \frac{R_4}{(R_1 + R_4)^2} & \frac{\partial f}{\partial R_2} &= -E_{EX} \frac{R_3}{(R_2 + R_3)^2} \\ \frac{\partial f}{\partial R_3} &= E_{EX} \frac{R_2}{(R_2 + R_3)^2} & \frac{\partial f}{\partial R_4} &= -E_{EX} \frac{R_1}{(R_1 + R_4)^2} \end{aligned} \quad (54)$$

The following key differences between the PVDF sensor rosette and the corresponding MFSG are noted:

1. Sensitivity: the output of a full Wheatstone bridge under small strain is given by

$$E_o \approx GF \times \varepsilon_h \times E_{EX} \quad (55)$$

Assuming a typical gage factor of 2.0 and an excitation voltage of 10V, the voltage output under one micro strain ($\mu\varepsilon$) is $20\mu\text{V}$, which is three orders of magnitude lower than that of a PVDF sensor (typically $10\text{mV}/\mu\varepsilon$) [11]. Even for semiconductor strain gauges whose gage factors are usually on the order of ~ 100 [126], the voltage output per micro strain is only $\sim 1\text{mV}$ under a 10V excitation, which still one order of magnitude lower than that for a PVDF sensor.

2. Because of their low sensitivity, the application of MFSGs almost always requires stringent signal conditioning to maintain an acceptable signal-to-noise ratio (SNR). This is not true for PVDF sensor rosettes because the SNR is inherently much higher due to their higher sensitivity.

3. The output of the Wheatstone bridge given in Eq. (55) is a first order approximation to the nonlinear function in Eq. (53). Taking the axial strain rosette for example, where

$$\begin{aligned}\Delta R_1 / R_1 &= \Delta R_3 / R_3 = K \varepsilon_h \\ \Delta R_2 / R_2 &= \Delta R_4 / R_4 = -\nu_h K \varepsilon_h\end{aligned}\tag{56}$$

and assuming the bridge is initially balanced by ensuring $R_1 = R_2 = R_3 = R_4$, the voltage output due to the strain input in Eq. (56) is found as:

$$\frac{E_o}{E_{EX}} = \frac{K \varepsilon_h (1 + \nu_h)}{2 + K \varepsilon_h (1 - \nu_h)}\tag{57}$$

E_o is approximately linear with respect to ε_h only when (i) the strain is small and (ii) the Wheatstone bridge is initially balanced resistively. On the other hand, the output of a PVDF rosette is linear with respect to the input strain as long as Eq. (31) holds.

Design of general purpose PVDF sensor rosette

PVDF sensor rosette can also be used to identify all three in-plane strain components in a general strain field. In general, to decouple all three strain components, three PVDF rosettes must be used. In Eq. (39), assuming there is no temperature change and the strain field is uniform within the electrode area of the sensor

$$q = K_1 \varepsilon_1 + K_2 \varepsilon_2 \quad (58)$$

where

$$K_1 = \frac{(d_{31}Y_1 + \nu_{12}d_{32}Y_2)A_3}{1 - \nu_{21}\nu_{12}} \quad (59)$$

$$K_2 = \frac{(d_{32}Y_2 + \nu_{21}d_{31}Y_1)A_3}{1 - \nu_{21}\nu_{12}}$$

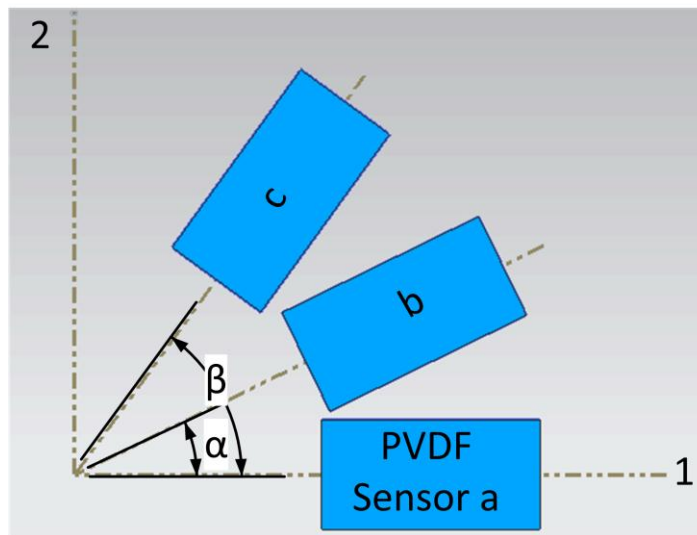


Figure. 26. General purpose PVDF rosette configuration.

With the general PVDF sensor rosette shown in Figure. 26, and using Mohr's strain circle, we can obtain three equations for three unknowns, $\varepsilon_{1,h}$, $\varepsilon_{2,h}$ and $\varepsilon_{6,h}$, which denote the normal strain along axis 1, normal strain along axis 2 and tensorial shear strain in the host structure, respectively. The equations in matrix form are given in Eq. (60).

$$\begin{bmatrix} K_1 & K_2 & 0 \\ \frac{K_1 + K_2}{2} + \frac{K_1 - K_2}{2} \cos 2\alpha & \frac{K_1 + K_2}{2} - \frac{K_1 - K_2}{2} \cos 2\alpha & (K_1 - K_2) \sin 2\alpha \\ \frac{K_1 + K_2}{2} + \frac{K_1 - K_2}{2} \cos 2\beta & \frac{K_1 + K_2}{2} - \frac{K_1 - K_2}{2} \cos 2\beta & (K_1 - K_2) \sin 2\beta \end{bmatrix} \begin{bmatrix} \varepsilon_{1,h} \\ \varepsilon_{2,h} \\ \varepsilon_{6,h} \end{bmatrix} = \begin{bmatrix} q_a \\ q_b \\ q_c \end{bmatrix} \quad (60)$$

Substituting $\kappa = K_1/K_2$, and letting $\beta = 2\alpha$, the condition number of the matrix can be analyzed numerically, as shown in Figure. 27. It can be seen that in the case of the MFSG ($\kappa = 100$) and the PVDF sensor ($\kappa = 10$), the coefficient matrix is well conditioned and the three strain components can be solved by inverting the coefficient matrix when α is in the range of 45° to 80° . With $\alpha = 45^\circ$ or 60° , the coefficient matrix can be significantly simplified. For a PZT sensor ($\kappa \rightarrow 1$), the coefficient matrix is close to singular, hence making it unsuitable for decoupling of the strain components.

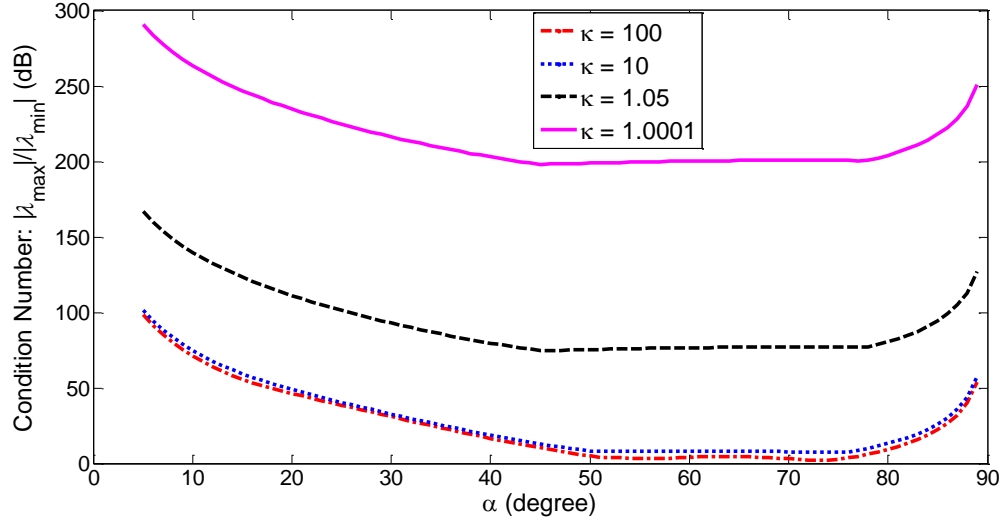


Figure. 27. Condition number of the coefficient matrix.

Experimental Validation

To validate the PVDF rosette designs presented earlier and to compare the performance of the PVDF rosettes with their MFSG equivalents, experiments were performed for all three types of rosettes. An aluminum beam with a rectangular cross section, a circular cross section shaft and a rectangular bar were prepared for the bending strain rosette, shear strain rosette and axial strain rosette, respectively. The host structures were also instrumented with corresponding MFSG rosettes at locations very close to the PVDF rosette. The experimental set-up is shown in Figure. 28.

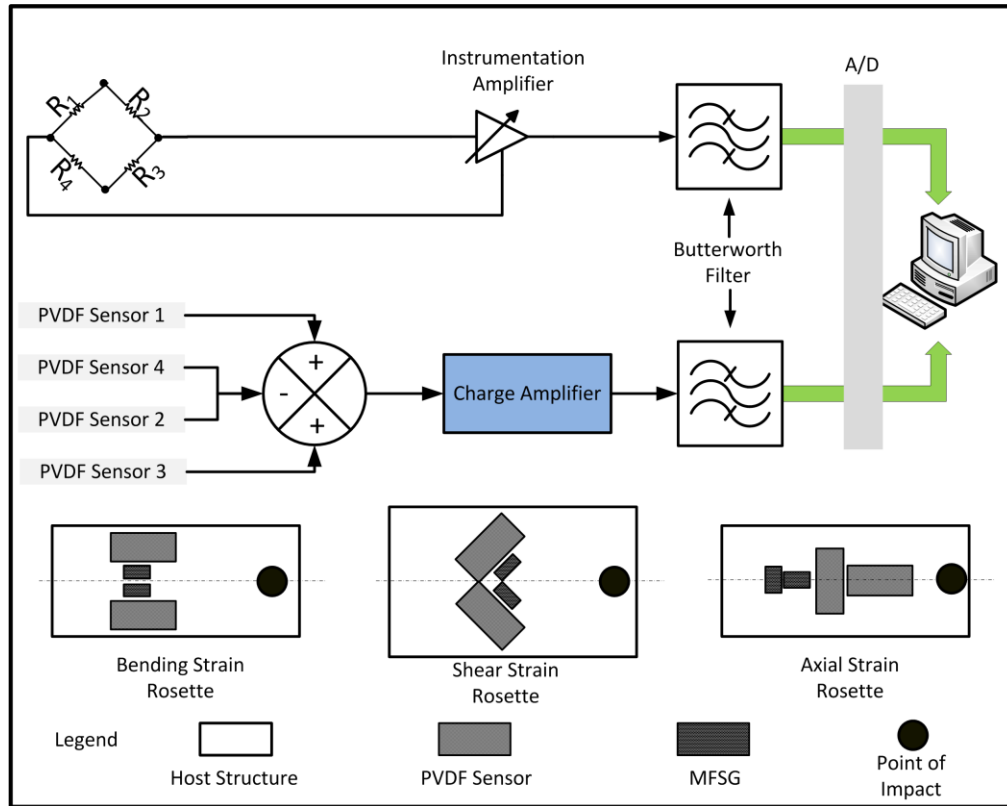


Figure. 28. Experimental setup for PVDF rosette and MFSG rosette.

All PVDF sensors used were 30 mm by 12 mm in size, while the MFSGs used in the bending strain rosette, the torsion strain rosette and the axial strain rosette were 11.4 mm by 8.4 mm, 7 mm by 6.3 mm and 7.1 mm by 7.1 mm in size, respectively. The MFSG signals are amplified by an instrumentation amplifier, while the PVDF sensor signals are sent to a charge amplifier. The low cut-off frequency of the charge amplifier is 0.7Hz^3 . A 5th order Butterworth filter with a cut-off frequency of 5KHz serves as the anti-aliasing filter before the signals are sampled into the discrete domain. The sampling rate was set to 20 KHz to ensure that at least 30dB attenuation is achieved at or above the

³ as given by $1/(2RC_f)$ where R is the feedback resistance of the charge amplifier.

Nyquist frequency (10KHz). Only the dynamic signals are compared for the PVDF and the MFSG rosettes because the PVDF sensor cannot capture static signals due to decay of charges over time.

In all tests, dynamic strain was introduced by hitting the host structure with an impact hammer. The point of contact was changed from test to test to introduce varying loading combinations of the host structure. The MFSG signals are taken as the reference signal. If the output from the PVDF rosette matches the reference signal, the PVDF rosette design and the corresponding model is considered to be valid. The experimental results are shown in Figure. 29, Figure. 30 and Figure. 31.

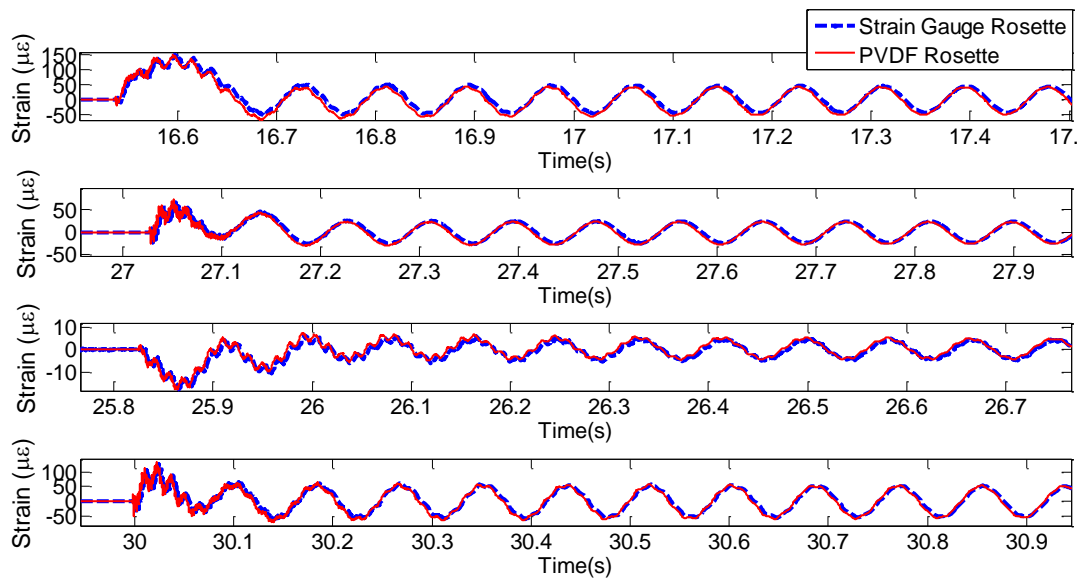


Figure. 29. Bending strain rosette tests.

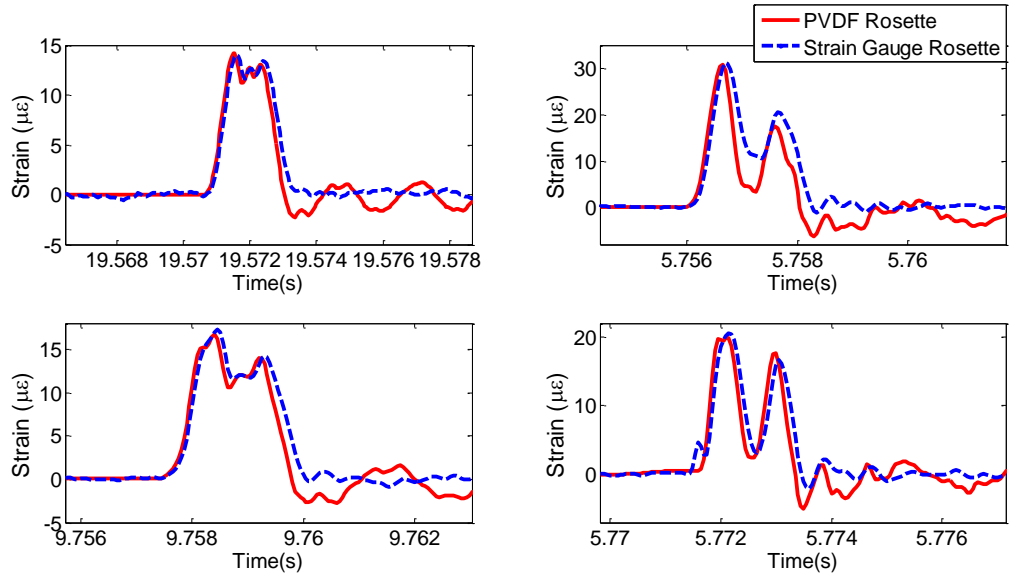


Figure. 30. Shear strain rosette tests.

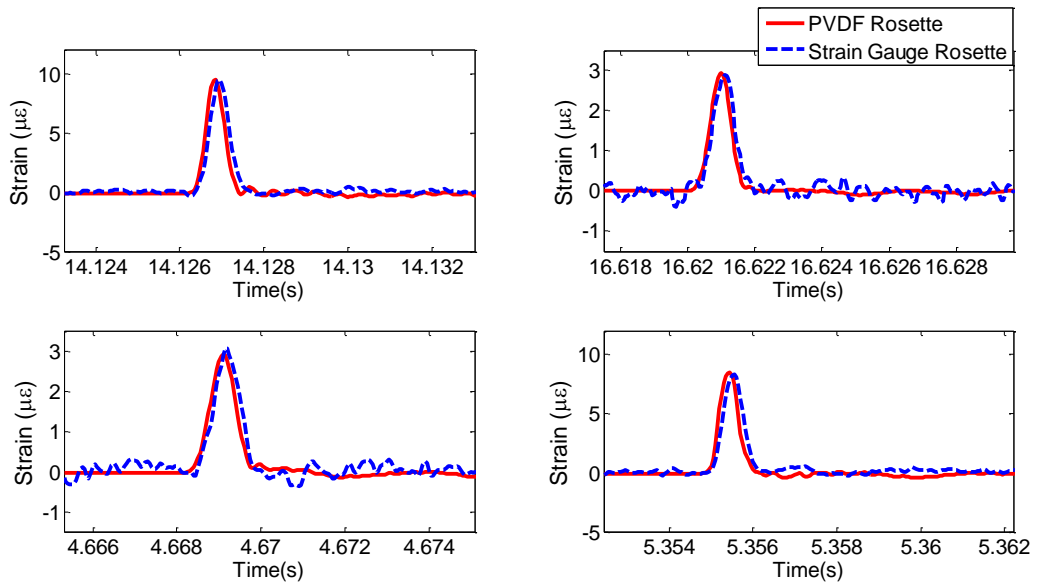


Figure. 31. Axial strain rosette tests.

It can be seen from the results that all three types of PVDF rosette signals agree quite well with the corresponding MFSG rosette signals in the time domain. Note that in all the results shown the PVDF sensor signal has a faster rise time than the MFSG signal.

This is at least partly due to the fact that PVDF sensors are larger in size and are located slightly closer to the point of impact. It is unclear at this point if the PVDF sensors will rise faster than the MFSG sensors if their locations are coincident. Additional tests are needed to answer this question. The periodic nature of the bending strain rosette signal suggests further comparison in the frequency domain, which is shown in Figure. 32. For the other two cases, the time domain PVDF sensor signals and MFSG signals are very close to impulse signals, and their respective spectra are flat within the bandwidth of the impact hammer (sub-1500Hz).

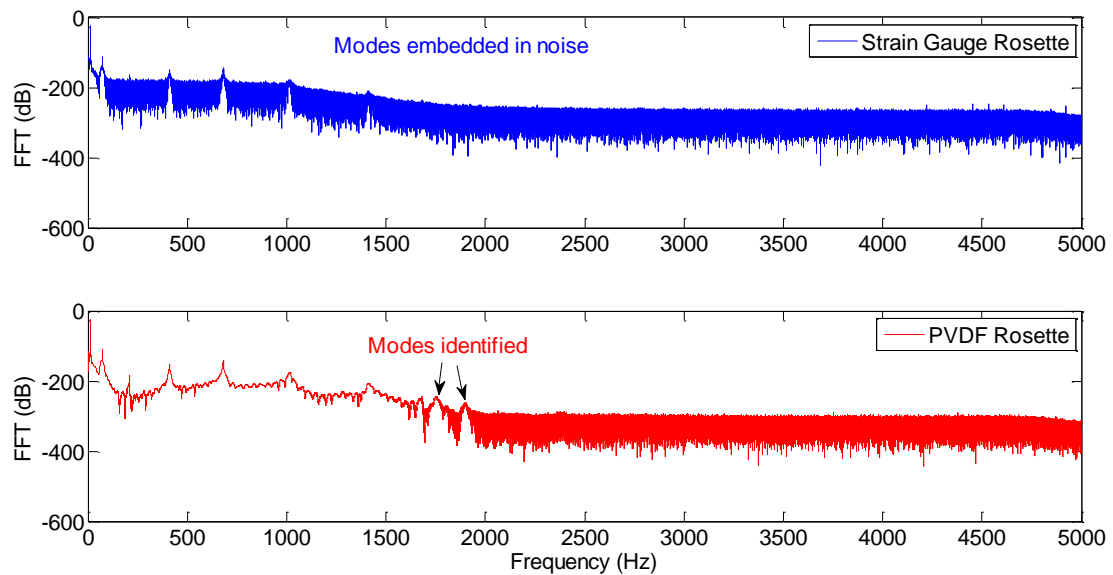


Figure. 32. FFT of a bending rosette test result (corresponding to subplot1 in Figure 12).

It can be seen that the frequency domain comparison again validates the PVDF sensor rosette design. In addition, the superior signal to noise ratio (SNR) of the PVDF sensor is also evident, especially in the sub-2KHz range. This is because the impact hammer could only excite the host structure up to a limited frequency. Due to the SNR

advantage, two additional modes that were masked by noise in the MFSG signal are revealed in the PVDF sensor signal. This suggests that the proposed PVDF rosette could be used in modal testing applications where low SNR is a concern. The close agreement between the PVDF sensor signal and the MFSG signal in both the time and frequency domains serve to validate the PVDF rosette designs and the corresponding models.

Summary

PVDF sensor rosettes for isolation of bending strain, shear strain and axial strain are designed, modeled and experimentally validated. Comparison between the PVDF and the MFSG signals verifies the ability of PVDF strain rosette to isolate a particular strain component of interest and demonstrates its advantage in terms of SNR. Two questions omitted by previous studies are answered in this chapter: 1) how to isolate a strain component of interest with multiple PVDF sensors, and 2) how the thermal strain and pyroelectric effect of the PVDF sensor shape the measured signal. First principles based models derived in this chapter facilitate quantitative evaluation of the elastic strain component of interest, even under changes in ambient temperature. Changes in material constants (e.g., p_3^σ , α , d_{31}) with temperature, which has been shown to be insignificant experimentally [34], are not considered in this study.

The three types of PVDF rosettes can also be combined to measure multiple strain components of interest, e.g., it is possible to measure the bending strain, the shear strain and the axial strain simultaneously on a circular cross section beam. Although limited to geometrically symmetric host structures, the PVDF rosettes proposed in this chapter can still find a wide range of applications in areas such as structural health monitoring and manufacturing process monitoring. Examples include monitoring of wind turbine shaft,

cutting tool condition and machine tool spindle health monitoring. The PVDF rosette also lends itself to the measurement of strain rate, which is a purely dynamic signal.

CHAPTER 5 CHATTER DETECTION AND FREQUENCY ESTIMATION

Introduction

This chapter presents a model-based computationally efficient method for detecting milling chatter in its incipient stages and for chatter frequency estimation by monitoring the cutting force signals. The chatter detection algorithm is an extension of the tool breakage detection algorithm proposed by Altintas [127]. Based on a complex exponentials model for the dynamic chip thickness, the chip regeneration effect is amplified and isolated from the cutting force signal for early chatter detection. The proposed method is independent of the cutting conditions. With the aid of a one tap adaptive filter, it is also found to be able to distinguish between chatter and the dynamic transients in the cutting forces due to sudden changes in workpiece geometry and tool entry/exit. To facilitate chatter suppression once the onset of chatter is detected, a time domain algorithm is proposed so that the dominant chatter frequency can be determined accurately without using computationally expensive frequency domain transforms such as the Fourier Transform. The chatter frequency estimation algorithm originates from the spectrum estimation of a complex exponentials signal embedded in white noise and is shown to be as accurate as and computationally more efficient than Fourier Transform based methods.

In the following sections, the proposed methodology is presented with experimental verification and discussion of the computational complexity and conclusions.

Methodology

Complex exponentials cutting force model

Cutting force is chosen as the source signal for chatter detection because of the availability of well-established mechanistic models for milling. As established in [8], with the absence of runout, the instantaneous tangential force f_j^t and radial force f_j^r acting on tooth j in cut are given by (see Figure. 33)

$$\begin{aligned} f_j^t &= g(\phi_j(t))K_s a [s_t \sin(\phi_j(t) - \pi) + A_j^p \sin(\omega_c t + \psi_j^p) - A_j^c \sin(\omega_c t + \psi_j^c)] \\ f_j^r &= K_r f_j^t \end{aligned} \quad (61)$$

where K_s is the specific cutting force coefficient, a is the axial depth of cut, s_t is the feed per tooth, $\phi_j(t)$ is the instantaneous angular position of tooth j , K_r is the ratio of the radial force to the tangential force, A_j^p and A_j^c are the amplitudes of the chip regeneration waviness in the previous and current tooth passes, respectively, and ψ_j^p and ψ_j^c denote the phases of the chip regeneration waviness in the previous and current tooth pass, respectively, ω_c is the chip regeneration frequency or chatter frequency, and $g(\phi)$ is a rectangular window:

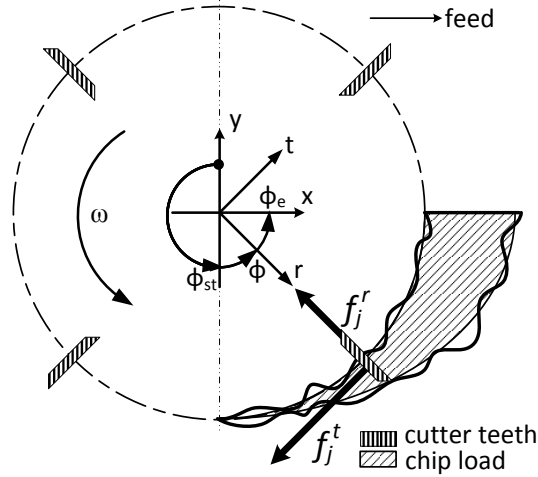


Figure. 33. Chip regeneration in milling.

function that simulates the interrupted cutting behavior and defined as

$$g(\phi) = \begin{cases} 1 & \phi_{st} < \phi < \phi_e \\ 0 & \text{otherwise} \end{cases} \quad (62)$$

where ϕ_{st} and ϕ_e are angular positions of tooth entry and exit, respectively. Please note that the linear mechanistic model given in Eq. (61) assumes that tangential cutting force is proportional to the chip thickness and K_s and K_r are both constants for a certain combination of cutting tool and workpiece materials. This model is only valid under the following assumptions: 1) the undeformed chip thickness is sufficiently larger than the cutting edge radius [128], 2) the workpiece material is homogeneous, and 3) the chip formation occurs primarily through shear deformation. Resolving f_j^t and f_j^r into the workpiece coordinate system (x-y), we have

$$\begin{aligned}
f_j^x &= f_j^t \cos \phi_j + f_j^r \sin \phi_j \\
f_j^y &= f_j^t \sin \phi_j - f_j^r \cos \phi_j
\end{aligned} \tag{63}$$

The total cutting force is simply the summation of the resolved forces over all teeth engaged in cutting:

$$F_x(t) = \sum_{j=1}^z f_j^x \quad F_y(t) = \sum_{j=1}^z f_j^y \tag{64}$$

It can be shown that with no chip regeneration, i.e. $A_j^p = A_j^c = 0$, F_x and F_y are periodic functions with a period of

$$\tau_T = 2\pi / z\omega \tag{65}$$

where z is the number of cutter teeth, ω is the angular speed of the tool (also known as the spindle frequency), τ_T denotes the tooth period, $\tau = z\tau_T$ represents the spindle period and $\omega_T = 2\pi / \tau_T$ is the tooth passing frequency. Due to the periodic rectangular window functions $g(\phi_j)$, the Fourier series expansion of $F(t)$ (which can be $F_x(t)$, $F_y(t)$ or a

functional combination of the two) consists of an infinite number of higher order harmonics of the tooth passing frequency and the chip regeneration frequency [5]:

$$F(t) = \sum_{k=-\infty}^{\infty} F_k e^{jk\omega_r t} + \sum_{k=-\infty}^{\infty} [C_k^+ e^{j(\omega_c+k\omega_r)t} + C_k^- e^{j(-\omega_c-k\omega_r)t}] \quad (66)$$

where ω_c is still the chip regeneration frequency and F_k , C_k^+ and C_k^- denote the complex amplitudes of the corresponding harmonics. Since $F(t)$ is a real signal, it follows

$$F_k = (F_{-k})^* \quad C_k^+ = (C_k^-)^* \quad (67)$$

where $*$ denotes the complex conjugate operator. Since the energy contained in the cutting force signal is finite, only a limited number of the higher order harmonics are significant and the rest of them can be safely dropped. If we consider a measured cutting force signal $\hat{F}(t)$, a random disturbance needs to be added to account for the various random processes also present in the actual process, e.g. material inhomogeneities, noise in the measurement system, etc. In light of the central limit theorem, the aggregation of all these random processes can be modeled as a white Gaussian noise. Therefore, the Fourier series expansion of $\hat{F}(t)$ can be established as:

$$\hat{F}(t) \approx \sum_{k=-N_1}^{N_1} F_k e^{jk\omega_r t} + \sum_{k=-N_2}^{N_2} [C_k^+ e^{j(\omega_c + k\omega_r)t} + C_k^- e^{j(-\omega_c - k\omega_r)t}] + w(t) \quad (68)$$

where $w(t)$ is the additive Gaussian white noise and N_1 and N_2 determine the number of significant harmonics of the tooth passing frequency and the chip regeneration frequency, respectively. The insight provided by Eq. (68) is that $\hat{F}(t)$ consists of three parts: a periodic part due to the rigid body motion of the cutting tool and interrupted cutting, a aperiodic chip regeneration part due to instantaneous deflections of the tool/workpiece and a unknown stochastic disturbance due to material inhomogeneity, measurement system noise, etc. When the cutting process is stable, the cutting force is dominated by the periodic part. During transition from chatter-free cutting to unstable cutting, the chip regeneration part starts to grow and eventually dominates the cutting force signal after chatter is fully developed.

Chatter detection algorithm

The proposed chatter detection algorithm is based on the complex exponentials model given in Eq. (68) and contains four steps aimed at isolating and amplifying the chip regeneration part and compensating for the transients introduced by tool entry/exit, workpiece geometry variations and other non-stationary events that may occur during milling. These four steps are described next.

Differentiation

Since the chip regeneration frequency is usually higher than the tooth passing frequency, the force signal is first differentiated with respect to time to amplify the high

frequency content in the force signal. It is clear from Eq. (68) that differentiation usually causes the chip regeneration frequency content to be amplified by a larger ratio than the tooth passing frequency. Note that after differentiation, the periodic part still has the same period as before. This step is summarized as follows:

$$df(t) = \frac{d}{dt} \hat{F}(t) \quad (69)$$

To prevent the ultra-high frequency content in $\hat{F}(t)$ from being amplified inappropriately by the differentiation, the frequency band above the highest possible chatter frequency is attenuated before differentiation. As suggested in [89], chatter vibrations range in frequencies from 200Hz to as high as 4000 Hz. Therefore, the cut-off frequency of the anti-aliasing filter was set to 5000Hz in this work so that the ultra-high frequencies in the source signal will not present any problem during differentiation.

Since the cutting force signal is almost always discretized, the differentiation operation is approximated by finite order differences. Three finite impulse response (FIR) filters (1st, 2nd and 3rd order) that approximate the ideal differentiator in the least squares sense are designed and their frequency responses are shown in Figure. 34. It can be seen that all three FIR filters are very similar in performance in the 0 to 0.2 Hz range. Beyond 0.2 Hz, the 1st order FIR filter outperforms the others. Therefore, the 1st order FIR filter, which is essentially the first order difference, is used in this study:

$$df(n) = \hat{F}(n) - \hat{F}(n-1) \quad (70)$$

Spindle Period Averaging:

Because the periodic part of the cutting force signal is due to the tooth period, it can be isolated from the chip regeneration content, which is due to the instantaneous deflection of the tool and/or the workpiece. In order to make the chip regeneration part of the signal stand out, the tooth passing frequency and its harmonics need to be removed. It is proposed in [91] to remove each harmonic with a notch filter, which is computationally very expensive. In addition, the number of notch filters needed is hard to determine. In this work, the removal of the periodic content in the measured force signal is achieved in time domain by integrating the measured cutting force signal over its smallest period, which, in theory, is τ_T . However, due to cutter runout, the cutting force

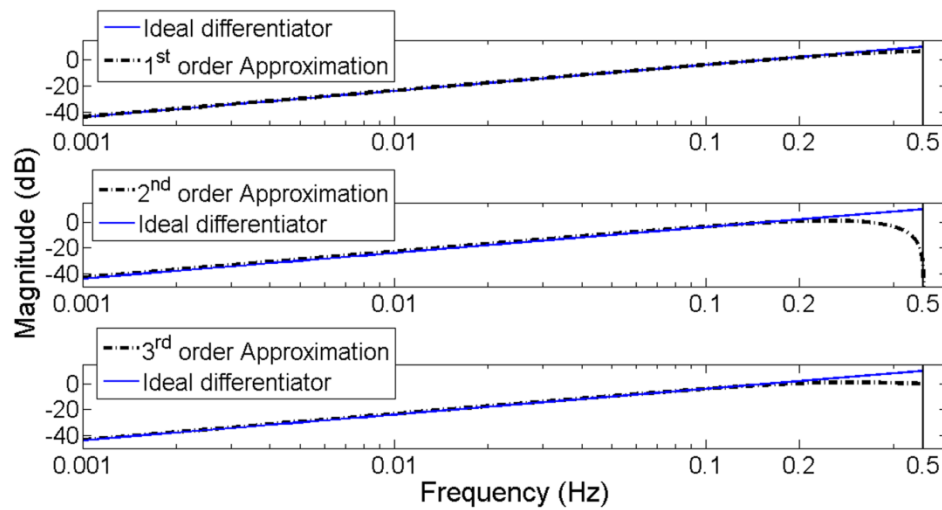


Figure. 34. Ideal Differentiator and its finite order approximations.

signal usually contains the spindle frequency and its harmonics. Accordingly, the smallest period of the periodic part in the cutting force signal is τ . Therefore, $df(t)$ is integrated over the spindle period instead. To magnify the signal-to-noise ratio (SNR), the integration is performed on the second power of $df(t)$ as follows

$$x_k = \int_{k\tau}^{(k+1)\tau} df(t)^2 dt \quad (71)$$

Note that the outcome of this step is a time series x_k corresponding to the spindle period k . In this step, the periodic part in $\hat{F}(t)$ results in a global DC trend in x_k , while the chip regeneration part and the stochastic disturbance may vary slightly from one spindle period to the next, leading to local variations around the DC trend. During stable cutting, the amplitudes of the chip regeneration part and the stochastic disturbance are much smaller than that of the periodic part. Therefore, the local variation in x_k around the DC trend is small in stable cutting.

When dealing with discretized $df(t)$, the integration in Eq. (71) is approximated by summation over the spindle period and can be implemented recursively in time. Per convention, x_k is treated as a time series sampled at unit frequency.

One Tap Adaptive Filtering:

In stable cutting, if the chip load is exactly the same from one spindle period to the next, we expect the DC trend in x_k to be time invariant, or

$$x_{k+1} = x_k + a_k \quad (72)$$

where a_k is a normally and independently distributed (NID) random process that is attributed to the stochastic disturbance and the chip regeneration part from one spindle period to the next. Eq. (72) describes a first order autoregressive (AR) process usually referred to as the random walk process. However, the AR(1) model is not valid when the chip load varies with time, for example, during tool entry/exit or when the tool passes through an existing geometric feature in the workpiece, e.g. a hole [127]. Under these circumstances, the time varying AR(1) model in Eq. (73) is more appropriate

$$a_k = x_{k+1} - \beta_k x_k \quad (73)$$

where β_k is the time varying AR(1) coefficient. In macro and meso-scale milling, the tool feed is small compared to the tool diameter and, in general, the size of pre-existing workpiece geometric features. Therefore, the pre-existing geometric features cause the chip load to vary only slightly from one spindle period to the next and the global DC trend in x_k to vary slowly and smoothly over the time. This global variation is different in behavior from the small local variations in x_k caused by the stochastic disturbance $w(t)$ and the chip regeneration content, as illustrated in Figure. 35.

Eq. (73) can be implemented as a one-step predictor with a time varying tap weight β_k , which can be adaptively updated in each spindle period with the latest data x_{k+1} using the recursive least squares (RLS) algorithm [121]. One recursion of the RLS algorithm is given here for completeness:

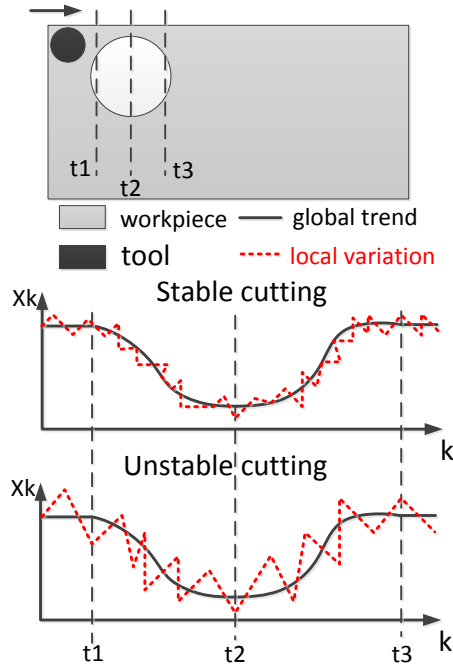


Figure. 35. Global trend and local variation in x_k .

$$\begin{aligned}
 a_k &= x_{k+1} - \beta_k x_k & K &= P_k x_k / (\lambda + x_k P_k x_k) \\
 \beta_{k+1} &= \beta_k + K a_k & P_{k+1} &= (1 - K x_k) P_k / \lambda
 \end{aligned}
 \tag{74}$$

where λ is the forgetting factor controlling how many past data points to take into account for predicting the next sample, P_k is the inverse of the autocorrelation matrix of x_k , and K

is the Kalman gain. Note that a_k is known as the *a priori error* in adaptive filtering literature and the *innovation* in the Kalman filter literature. Since a one tap adaptive filter is adopted here, P_k and K are both scalars. For the sake of implementation, Eq. (74) can be rearranged as follows:

$$\begin{aligned} a_k &= x_{k+1} - \beta_k x_k & K &= P_k x_k / (\lambda + (P_k x_k) x_k) \\ \beta_{k+1} &= \beta_k + K a_k & P_{k+1} &= P_k / (\lambda + (P_k x_k) x_k) \end{aligned} \quad (75)$$

When the cutting process is stable, the RLS filter enables the slow and smooth variation in the global trend in x_k due to the time varying chip load to be effectively captured by the AR(1) model, resulting in a stationary residual signal a_k with small variance. However, when chatter vibration starts to build up, the local variation caused by the chip regeneration content in x_k is no longer negligible and the RLS algorithm can no longer adapt fast enough to capture the rapid changes in x_k , leading to an a_k with increasing variance. In this case, a standard univariate control chart can be implemented to monitor a_k for chatter detection. Chatter is signaled when the amplitude of a_k exceeds the predetermined control limits. The upper control limit (UCL) and lower control limit (LCL) of the control chart can be set as

$$UCL = L\sigma \quad LCL = -L\sigma \quad (76)$$

where σ is the standard deviation estimated from a_k during stable cutting and L is a real, positive number determined from the acceptable false alarm rate α (i.e., the probability of issuing an alarm when chatter does not occur). If a_k can be assumed to follow the Gaussian distribution, L can be determined as

$$Z(z \leq L) = 1 - \frac{\alpha}{2} \quad (77)$$

where $Z(z)$ stands for the cumulative distribution function of the standard Gaussian distribution. During stable cutting, the expected number of successive samples that fall in the control limits before a false alarm is activated, referred to as the average run length (ARL_0), is given by

$$ARL_0 = \frac{1}{\alpha} \quad (78)$$

It is clear from the above discussion that setting up the control limits for the control chart is independent of any cutting conditions; L is chosen based on the acceptable false alarm rate and σ is estimated from a_k at the very beginning of each cut. Therefore, the proposed chatter detection algorithm is expected to work independently of cutting conditions and the tool/ workpiece materials.

Median Filter

The last step in the chatter detection algorithm is to remove any singular peaks in a_k so that the false alarm rate is reduced. Singular peaks may result from a hard spot in the workpiece, tool breakage or chipping, etc. In these cases, a one tap adaptive filter cannot respond fast enough to the sudden large variation in the force signal and a singular out-of-control point may appear in a_k . It is proposed to use a median filter with a window size of three to remove such singular peaks. The operation of the median filter is described as

$$a_k^M = \text{median}(a_{k-1}, a_k, a_{k+1}) \quad (79)$$

where a_k^M is the signal to be used for chatter detection. Note that the median filter delays chatter detection by one spindle period because a_k^M cannot be determined until a_{k+1} becomes available.

Limitations and discussion

It has been pointed out in [7] that chatter frequencies can be integer multiples of the spindle frequency ω when chatter occurs in the form of a flip bifurcation, where the chatter frequencies ω_c are given by:

$$\omega_c = \frac{2k+1}{2} \omega_r = \frac{2k+1}{2} z\omega \quad k = 0, 1, 2, \dots \quad (80)$$

where z is the number of teeth on the cutting tool. Clearly, for an even number of teeth, the chatter frequencies ω_c are integer multiples of ω , which will be completely removed during the spindle period averaging and adaptive filtering steps. Noticing that ω_c can never be an integer multiple of ω_T , it is proposed to use tooth period averaging on $df(t)^2$ instead of spindle period averaging:

$$x_k = \int_{k\tau_T}^{(k+1)\tau_T} df(t)^2 dt \quad (81)$$

While the tooth period averaging approach can potentially detect chatter earlier because a new x_k becomes available every tooth period and a_k^M is checked against the control limits z times per spindle period (instead of once per spindle period in the spindle period averaging approach), tool runout can cause periodic fluctuations in x_k and a_k^M with a period of z (note that x_k and a_k^M are time series sampled at unit frequency). An additional notch filter at the frequency of $1/z$ is then needed to remove the runout induced periodic fluctuations from x_k , thereby increasing the computational cost. Since flip bifurcation usually occurs in high speed and highly interrupted cutting, the spindle period averaging approach is expected to be more frequently used.

Dominant chatter frequency estimation

To facilitate chatter suppression, the dominant chatter frequency needs to be estimated from the cutting force signal once the onset of chatter has been recognized by the control chart. The spindle frequency or one of its harmonics is then matched with the

estimated dominant chatter frequency to suppress chatter [92]. Transform based methods such as Fast Fourier Transform (FFT) may be applied to the cutting force signal collected near the chatter onset point, and the dominant chatter frequency can be identified as the highest peak in the spectrum. However, tradeoff has to be made between the stationarity assumption (i.e. the signal is approximately stationary near the chatter onset point) and the frequency resolution: the greater the number of data samples, the better the frequency resolution is, but the less reasonable the stationarity assumption is. Here, a computationally more efficient algorithm that obviates the above difficulty is proposed.

In the incipient stages of chatter development, the chip regeneration part in the cutting force is still small in magnitude compared to the periodic part. Therefore, the period part needs to be removed from the cutting force signal by applying a first order difference [129]:

$$f(t) = \hat{F}(t) - \hat{F}(t - \tau) \quad (82)$$

Note that if flip bifurcation is expected to occur, τ_f instead of τ will show up in Eq. (82) and a notch filter at $1/z$ will be needed to preprocess $f(t)$. After the first order difference, only the chip regeneration content and the stochastic disturbance remain, and the Fourier series expansion of $f(t)$ has the following form:

$$f(t) \approx \sum_{k=-N_2}^{N_2} [C_k^+ e^{j(\omega_c+k\omega_T)t} + C_k^- e^{j(-\omega_c-k\omega_T)t}] + v(t) \quad (83)$$

where $v(t)$ is the white noise in $f(t)$. Note that $v(t)$ is different from $w(t)$ in Eq. (68) because of the first order difference in Eq. (82). Let $f(n)$ and $v(n)$ be the discretized versions of $f(t)$ and $v(t)$, respectively, and perform a change of notation on Eq. (83) as follows:

$$f(n) = \sum_{k=1}^p A_k e^{j\omega_k n} + v(n) \quad (84)$$

where $p = 4N_2 + 2$ and A_k and ω_k denote the complex amplitude and frequency of the corresponding harmonic, respectively. The estimation of ω_c from $f(n)$ is based on the eigendecomposition of the autocorrelation matrix of $f(n)$, which is defined as:

$$R_f = \begin{bmatrix} R_f(0) & R_f(-1) & R_f(-2) & \dots & R_f(-M+1) \\ R_f(1) & R_f(0) & R_f(-1) & \dots & R_f(-M+2) \\ R_f(2) & R_f(1) & R_f(0) & \dots & R_f(-M+3) \\ \dots & \dots & \dots & \dots & \dots \\ R_f(M-1) & R_f(M-2) & R_f(M-3) & \dots & R_f(0) \end{bmatrix} \quad (85)$$

where $R_f(k) = E[f(n)f^*(n-k)]$ $R_f(-k) = R_f^*(k)$

It can be shown that if the phases of each harmonic (contained in A_k) are statistically independent from each other, R_f can be decomposed into two parts [121]:

$$R_f = \sum_{k=1}^p |A_k|^2 e_k e_k^H + \sigma_v^2 I_{M \times M} \quad (86)$$

where

$$e_k = [1 \quad e^{-j\omega_k} \quad e^{-j2\omega_k} \quad \dots \quad e^{-j(M-1)\omega_k}]^H \quad (87)$$

is known as the signal vector, σ_v^2 is the variance of $v(t)$ and H denotes the Hermitian transpose. The first part in Eq. (86), denoted as R_s , is a M by M matrix of rank p , while the second part, denoted as R_n , is an identity matrix. Performing eigendecomposition on each part, we obtain

$$R_f = \sum_{i=1}^p \lambda_i^s v_i v_i^H + \sum_{i=1}^M \sigma_v^2 v_i v_i^H \quad (88)$$

where v_1, v_2, \dots, v_M is a set of orthonormal eigenvectors for R_s and $\lambda_1^s, \lambda_2^s, \dots, \lambda_p^s$ are the first p non-zero eigenvalues of R_s . The rest of the eigenvalues are zero. Rearranging Eq. (88), we get:

$$R_f = \sum_{i=1}^p (\lambda_i^s + \sigma_v^2) v_i v_i^H + \sum_{i=p+1}^M \sigma_v^2 v_i v_i^H \quad (89)$$

The first p eigenvectors in Eq. (89), v_1, v_2, \dots, v_p , are referred to as the signal eigenvectors and the last $(M-p)$ eigenvectors $v_{p+1}, v_{p+2}, \dots, v_M$ are referred to as the noise eigenvectors. Since R_f is a Hermitian matrix and the eigenvectors corresponding to different eigenvalues are orthogonal to each other [121], the signal eigenvectors corresponding to eigenvalues $(\lambda_i^s + \sigma_v^2)$ are orthogonal to the noise eigenvectors corresponding to eigenvalues σ_v^2 . Accordingly, the space spanned by the signal eigenvectors (known as the signal subspace) is orthogonal to the space spanned by the noise eigenvectors (known as the noise subspace). Since signal vectors e_k also lie in the signal subspace [130], they are orthogonal to any vector v that lies in the noise subspace, or

$$e_k^H v = \sum_{m=0}^{M-1} v(m) e^{-jm\omega_k} = 0 \quad k = 1, 2, \dots, p \quad (90)$$

Eq. (90) essentially means that the discrete time Fourier transform of v has p zeros at $\omega_1, \omega_2, \dots, \omega_p$. Or equivalently, $V(z)$, the z -transform of v , has p zeros on the unit circle in the z -plane, with the phase angle of each zero given by $\omega_k/2\pi$.

Although v can be an arbitrary vector in the noise space, it has been suggested in [131] to always use the *minimum norm vector* in the noise subspace, which is given by:

$$v_{\min} = \frac{V_n V_n^H u_1}{u_1^H V_n V_n^H u_1} \quad (91)$$

where $V_n = [v_{p+1} \ v_{p+2} \ \dots \ v_M]$ and $u_1 = [1 \ 0 \ \dots \ 0]^T$.

The algorithm for determining the dominant chatter frequency among all p complex exponentials in Eq. (84) can now be established as follows:

1. Compute the $M \times M$ autocorrelation matrix R_f according to Eq. (85). Since R_f is both Hermitian and Toeplitz, only the M independent elements in R_f need to be computed. In practice, the expectation operator E is approximated by the sample average. Note that since $f(n)$ is a time-varying signal, its autocorrelation matrix is time varying too. Therefore, at any time instant the autocorrelation matrix is computed using only the latest N data points. At time n , the estimated time dependent autocorrelation coefficient at lag k , $\hat{R}_f^n(k)$, is computed as

$$\hat{R}_f^n(k) = \frac{1}{N} \sum_{i=n-N+1}^n f(i) f^*(i-k) \quad k = 0, 1, \dots, M-1 \quad (92)$$

Since only the noise eigenvectors of R_f are of interest, the normalization by N is unnecessary and can be dropped for all elements in R_f :

$$\hat{R}_f^n(k) = \sum_{i=n-N+1}^n f(i)f^*(i-k) \quad (93)$$

It is straightforward to show that

$$\hat{R}_f^n(k) = \hat{R}_f^{n-1}(k) + f(n)f^*(n-k) - f(n-N)f^*(n-N-k) \quad (94)$$

which provides a way to evaluate the autocorrelation matrix recursively in time.

2. Perform the eigendecomposition on R_f , find its $(M-p)$ noise eigenvectors: $v_{p+1} v_{p+2} \dots v_M$ and the minimum norm vector v_{min} according to Eq. (91). Since we are dealing with a real signal $f(n)$, R_f is always real and symmetric, which can reduce the computation complexity significantly when computing its eigenvalues and eigenvectors [130].

3. Compute the roots of the $(M-1)^{\text{th}}$ order polynomial $V_{min}(z)$, the z-transform of v_{min} . The roots are found by computing the eigenvalues of the companion matrix which is $(M-1)$ by $(M-1)$ in size.

4. Sort all $(M-1)$ roots obtained in Step 3 to determine the root that is closest to the unit circle in the z -plane (i.e. the root whose magnitude is closest to unity), calculate its phase angle θ (in radians) and determine the dominant chatter frequency ω_c (in radians/second) from it

$$\omega_c = \theta F_s \quad (95)$$

where F_s is the sampling frequency (in Hz).

An example illustrating the relationship between the pole locations in the z -plane and the spectrum of the signal is given in Figure. 36. In the z -plane, the phase angle θ is simply the angle made between the positive direction of the horizontal axis and the line connecting the pole and the center of the unit circle. In this example, $(M-1) = 8$. Note that the pair of poles (p_2, p_2^*) closest to the unit circle corresponds to the strongest harmonics in the signal, i.e., the dominant chatter frequency, while the pair of poles close to the center of the unit circle (p_4, p_4^*) have little impact on the spectrum.

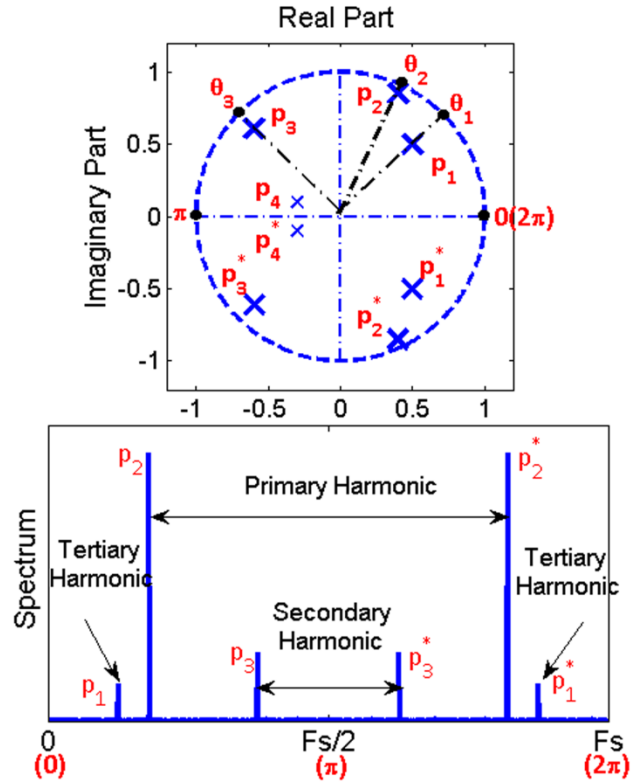


Figure. 36. Relationship between the pole location and the spectrum of the signal.

Since in most cases only the dominant chatter frequency is of interest, it is reasonable to set $p = 2$, i.e., it is assumed that there exist only two complex exponentials in $f(n)$: ω_c and $-\omega_c$. The dimension of R_f , M , needs to be larger than p .

The chatter detection and chatter frequency estimation algorithm is summarized block-diagrammatically in Figure. 37.

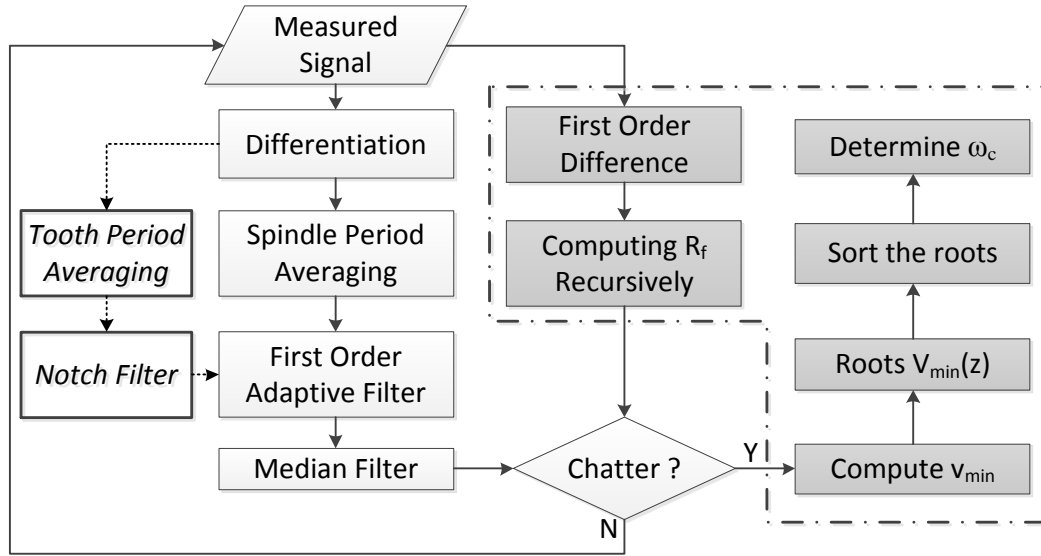


Figure. 37. Flow chart of the chatter detection and chatter frequency estimation method.

Experiments and Results

A set of end milling experiments was performed to verify the proposed methodology. The tests were designed such that the tool encounters different types of geometric features (holes with different diameters, slots, curvilinear tool paths, etc.) along the tool path. Cutting force signals were collected using a table-type force dynamometer (Kistler 9257B) at 10 KHz. Since the direction of tool motion with respect to the workpiece coordinate system may change along the tool path, the source signal is defined as follows to make it as directionally independent as possible:

$$df(t) = \sqrt{\left[\frac{dF_x(t)}{dt}\right]^2 + \left[\frac{dF_y(t)}{dt}\right]^2} \quad (96)$$

Chatter detection

The first two tests examine the capability of the chatter detection algorithm to recognize chatter when chatter is actually occurring, while the following three tests investigate if the proposed algorithm can distinguish between chatter and workpiece geometry-induced transients in the cutting forces. The control limits in all control charts are set as $L = 6$, which corresponds to a false alarm rate (α) of $2E-9$ and an ARL_0 of $5E8$. In other words, only one false alarm is expected after $5E8$ spindle revolutions according to the univariate control chart theory.

Test 1: In this test, chatter developed during a linear cut where the axial depth of cut increased linearly from 2.54 mm. The inputs (the two in-plane cutting forces) and outputs of the four-step chatter detection algorithm are shown in Figure. 38 and Figure. 39. A gentle linear trend is observed in F_x and F_y due to the increasing axial immersion. At the beginning of the cut, x_k is characterized by small local variations superimposed on a time varying global trend. The one tap adaptive filter then successfully removes the global trend and leads to zero-mean residuals a_k and a_k^M . As the chip regeneration part in the cutting force signal gradually builds up, the amplitude of the local variations in x_k also grows, resulting in residuals with increased variance. Eventually, chatter was detected around the 1322th spindle period, about 130 spindle periods earlier than the appearance of chatter marks on the workpiece. In this work, no optical evidence of the chatter marks was collected during the experiments. In future work, optical evidence of chatter marks, especially at the instant when the algorithm reports chatter alarm, may help further verify the capability of the algorithm to detect chatter.

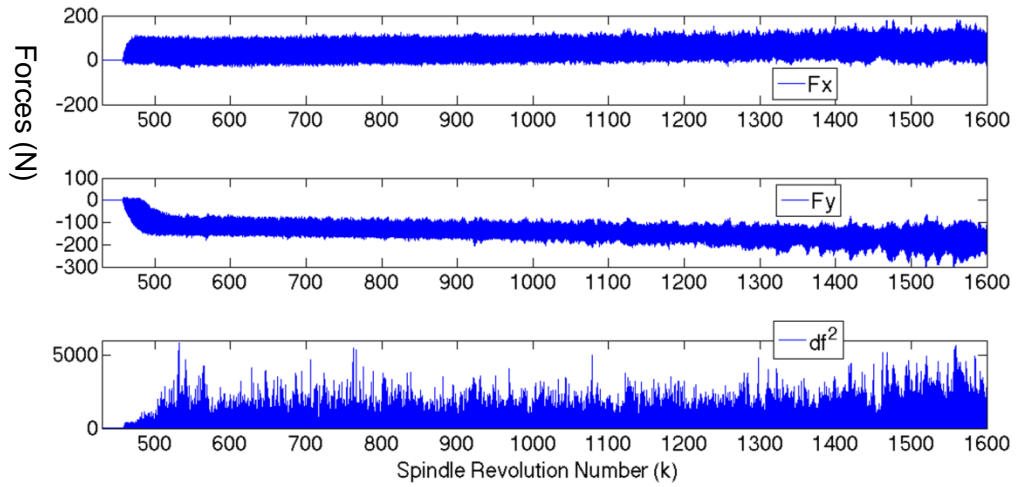


Figure. 38. Inputs and outputs of the chatter detection algorithms for test 1 (a) (Cutting conditions: four flute 6.35mm carbide tool, 1018 steel workpiece, 3400 RPM, 0.0254 mm feed/tooth, 50% radial immersion, 2.54 mm depth of cut at beginning).

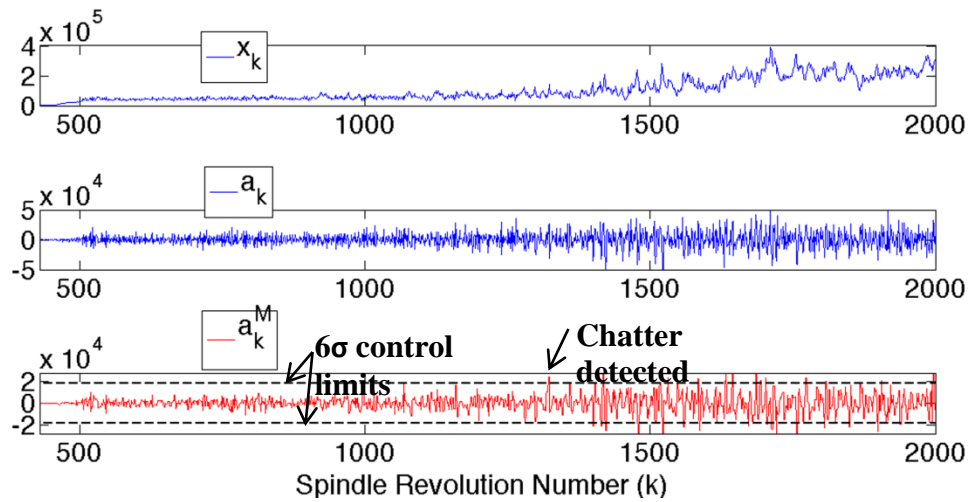


Figure. 39. Inputs and outputs of the chatter detection algorithms for test 1 (b).

Test 2: In this test, chatter developed during a linear cut with constant axial and radial depths of cut. The inputs and outcomes of the individual steps in the algorithm are

shown in Figure. 40 and Figure. 41. It can be seen that in the first 100 spindle revolutions after start of cutting ($\sim 350^{\text{th}}$ spindle revolution), the cutting forces are stable, x_k has a constant DC trend with small local variations and the residuals have very small variance. When chatter starts to build up, large variations appear in x_k , a_k and a_k^M . Chatter is detected around the 460^{th} spindle period, about 30 spindle periods ahead of the appearance of chatter marks on the workpiece.

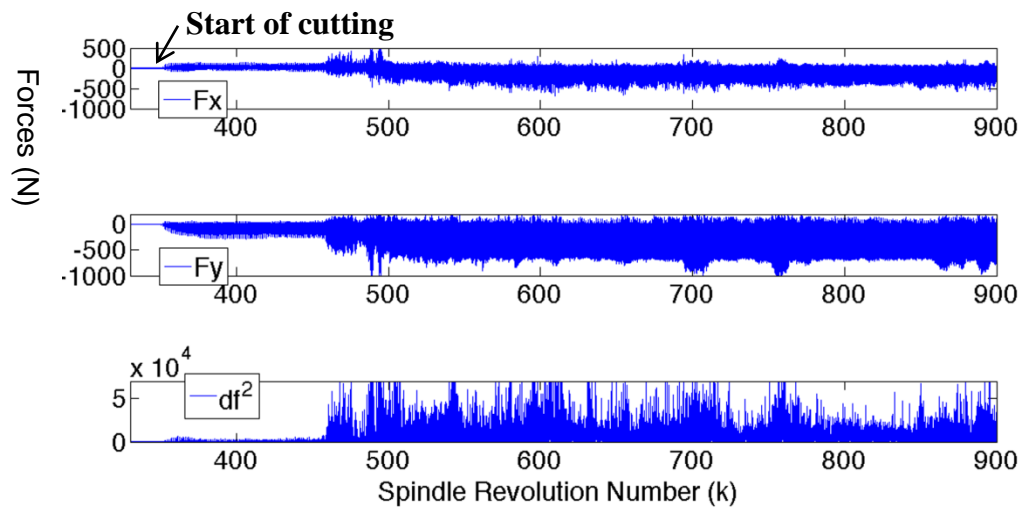


Figure. 40. Inputs and outputs of the chatter detection algorithms for test 2 (a) (two flute 25.4 mm carbide tool, 1018 steel workpiece, 1200 RPM, 0.0381mm feed/tooth, 25% radial immersion, 2.54 mm axial depth of cut).

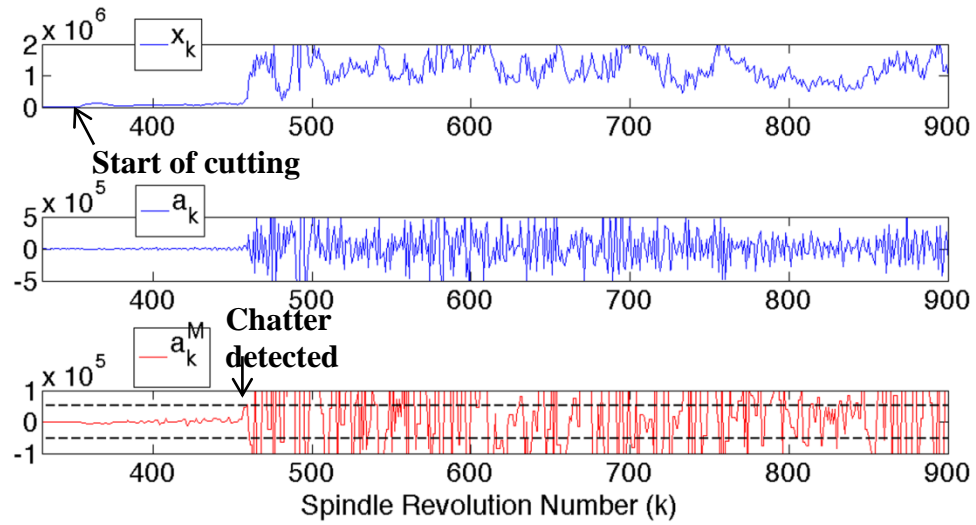


Figure. 41. Inputs and outputs of the chatter detection algorithms for test 2 (b).

In the previous two tests, chatter was successfully recognized by the proposed algorithm ahead of fully developed chatter, i.e. before chatter marks are observed on the workpiece. The workpiece is not damaged when the chatter alarm is issued, which means that corrective measures can still be taken to suppress chatter. The following three cutting tests examine the capability of the proposed algorithm to distinguish between chatter and various types of transients (e.g. tool entry/exit, sudden changes in workpiece geometry). Due to these transients, the cutting force signals become non-stationary and cannot be directly used in chatter detection.

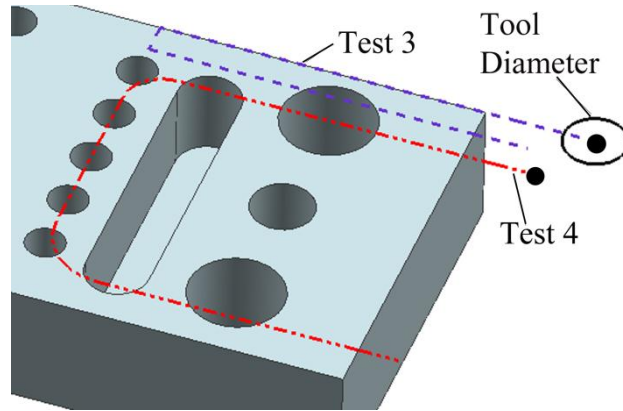


Figure. 42. Workpiece geometries and toolpaths for cutting tests 3 and 4.

Test 3: The workpiece geometry for this test is illustrated in Figure. 42. The beginning of the tool path is indicated with a black dot. The tool intersects an existing hole on the first leg of the tool path, makes two 90-degree turns, crosses a slot and temporarily jumps out of cut on the second leg. The cutting force signals shown in Figure. 43 are clearly non-stationary, which leads to a time varying global trend in x_k . The one tap adaptive filter removes the trend in x_k and produces a zero-mean residual a_k^M to be used for chatter detection. No chatter was observed in this test (i.e. no chatter marks), and a_k^M lies within the control limits throughout the cutting test as shown in Figure. 44.

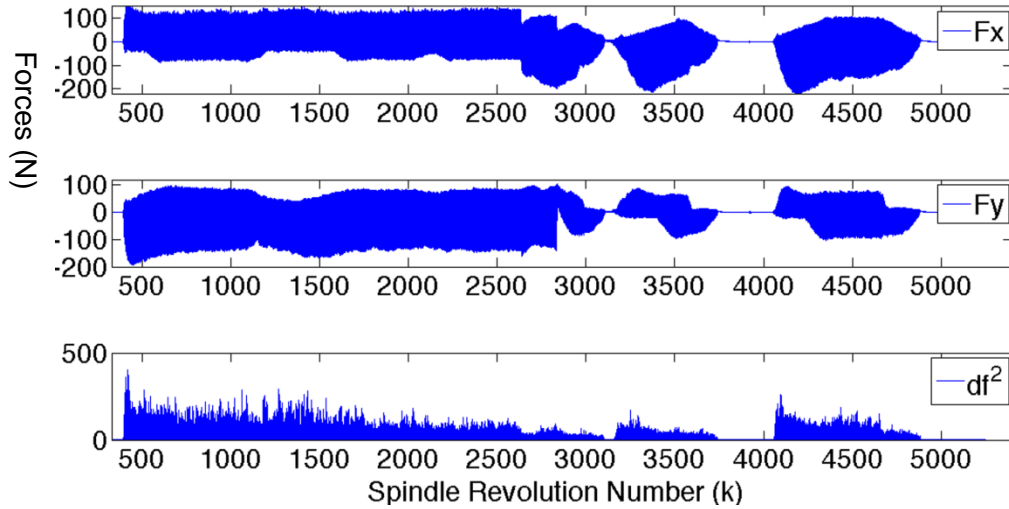


Figure. 43. Inputs and outputs of the chatter detection algorithms for test 3 (a) (two flute 12.7mm carbide tool, aluminum 7050 workpiece, 2400 RPM, 50%-100% radial immersion, 2.54 mm axial depth of cut, 0.016 mm feed/tooth).

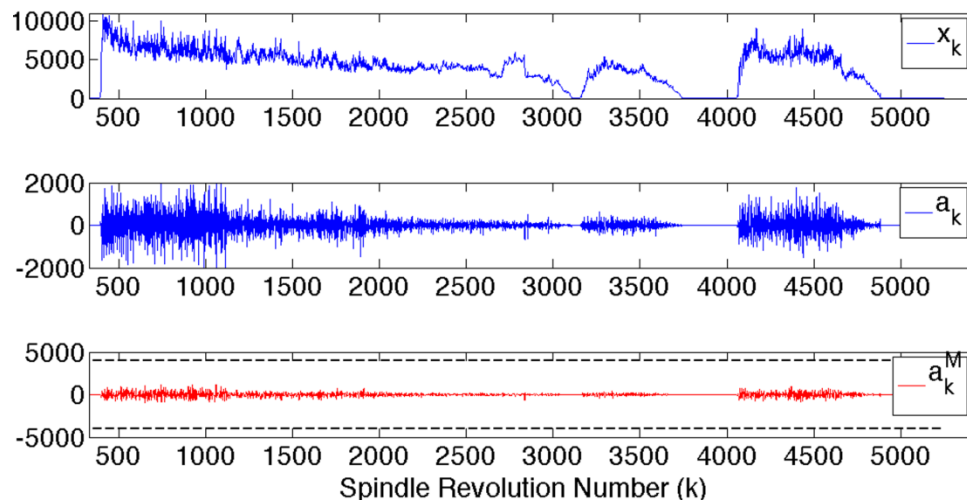


Figure. 44. Inputs and outputs of the chatter detection algorithms for test 3 (b).

Test 4: The workpiece geometry for this test is also shown in Figure. 42 and the beginning of the tool path is indicated with a black dot. In this test, the tool intersects a series of existing holes and slots along a curvilinear toolpath. Similar to Test 3, the time-varying trend in x_k due to non-stationary cutting forces are removed by the adaptive filter,

resulting in a zero-mean residual signal to be used for chatter prediction. No violation of the control limits is observed in Figure. 46, which suggests that no chatter occurred during the cutting operation. This is consistent with observing the workpiece surface.

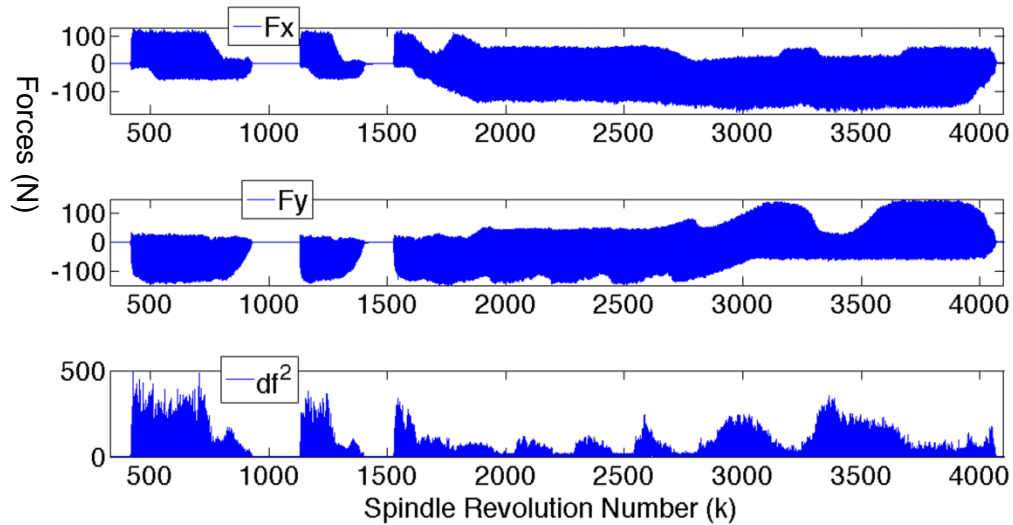


Figure. 45. Inputs and outputs of the chatter detection algorithms for test 4 (a) (two flute 12.7mm carbide tool, aluminum 7050 workpiece, 2400 RPM, 50%-100% radial immersion, 1.905 mm axial depth of cut, 0.0254 mm feed/tooth).

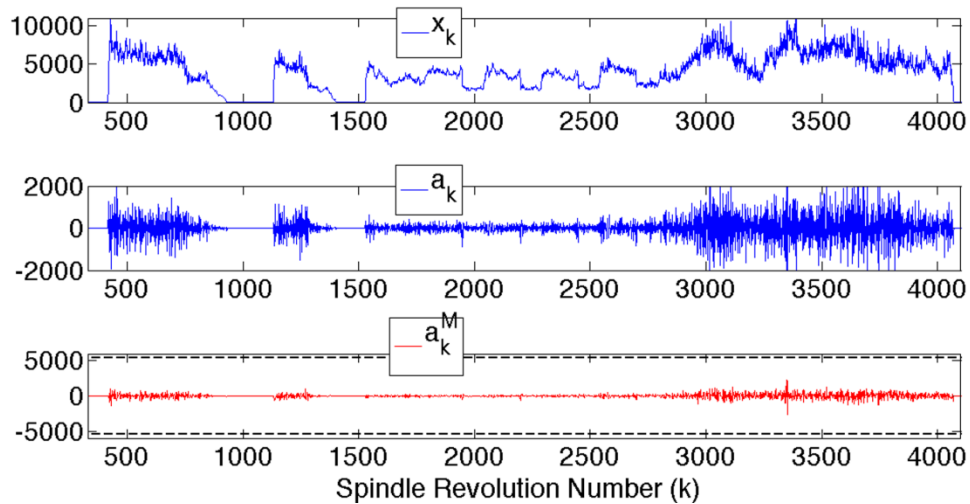


Figure. 46. Inputs and outputs of the chatter detection algorithms for test 4 (b).

Test 5: The workpiece geometry for this test is shown in Figure. 47, where the axial depth of cut increases in five steps along a straight line. The steps in the axial depth of cut are also evident in the cutting force signals. Again the time varying trend in x_k due to time varying chip load is effectively removed, resulting in a zero-mean stationary residual

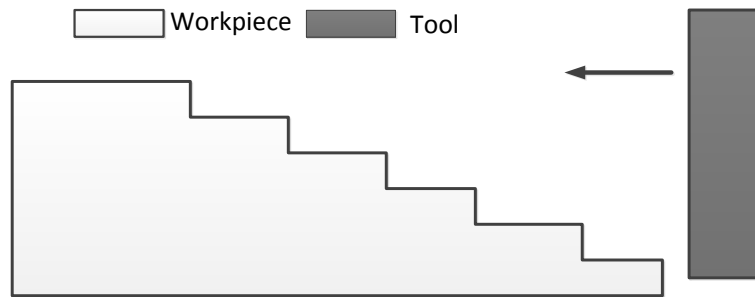


Figure. 47. Workpiece geometry and toolpath for cutting test 5.

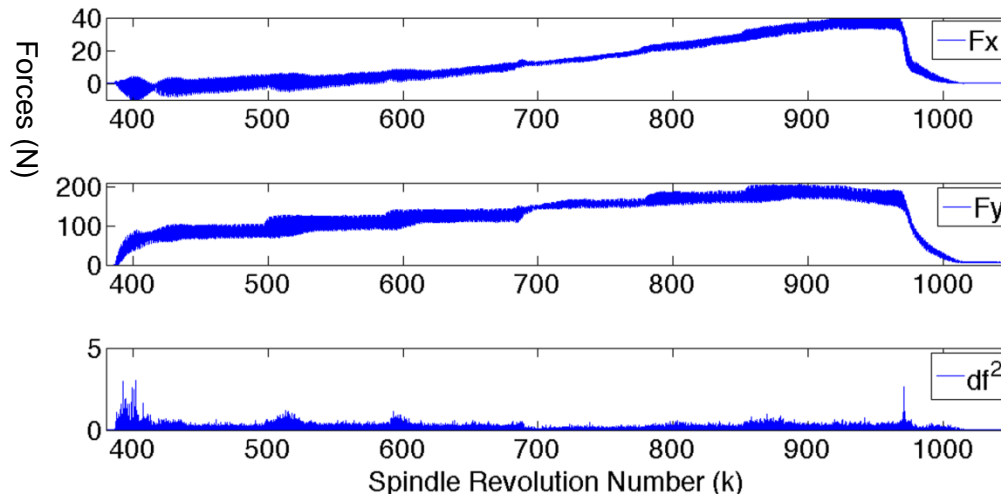


Figure. 48. Inputs and outputs of the chatter detection algorithms for test 5 (a) (four flute 6.35 mm High Speed Steel tool, aluminum 7050 workpiece, 2400 RPM, 50% radial immersion, 3.81 mm – 11.43 mm axial depth of cut, 0.0381 mm feed/tooth).

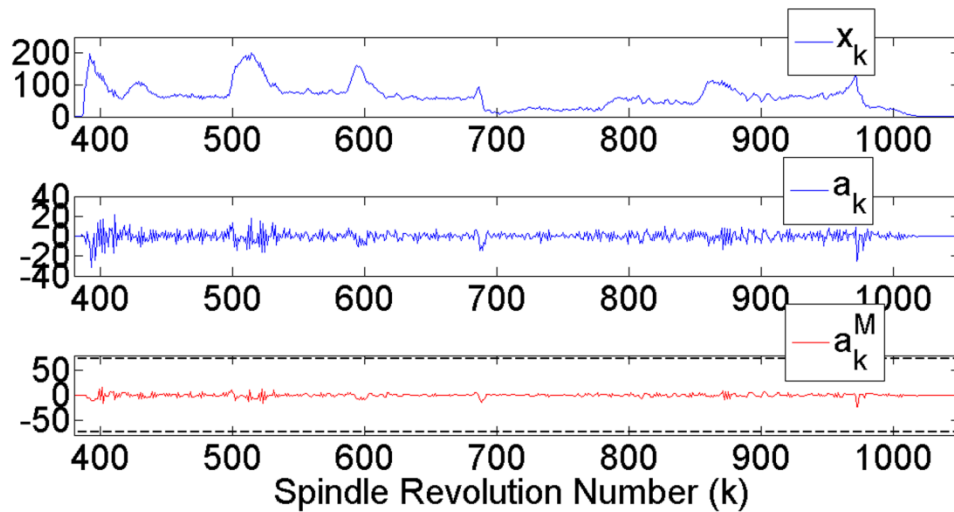


Figure. 49. Inputs and outputs of the chatter detection algorithms for test 5 (b).

signal that lies in the 6σ control limits. No chatter alarm is signaled by the control chart in

Figure. 49, which is in agreement with actual observations during the test.

In Tests 3-5, the proposed algorithm successfully reduces the non-stationary cutting force signals into zero-mean residual signals for chatter detection. No false chatter alarm is issued due to geometry-induced transients in the cutting force, which proves that the proposed algorithm is capable of distinguishing between chatter vibrations and transient dynamics due to changing workpiece geometry.

Chatter frequency estimation

The performance of the proposed chatter frequency estimation algorithm is investigated in this section and compared with FFT. The data used for estimation are the force signals collected during the three spindle revolutions immediately before chatter is signaled by the control chart. It is assumed that during these three spindle periods the cutting force signal is stationary so that FFT can be computed. For the proposed chatter estimation algorithm, $M = 8$, $p = 2$.

First of all, the spectra of $F(t)$ and $f(t)$ are compared in Figure. 50. For illustration purposes, all the FFTs and spectra shown are normalized by their maximum amplitude. In Figure. 50 it can be seen that when chatter is just indicated by the control chart, the amplitude of the chip regeneration content is still small compared to the spindle rotation frequencies in $F(t)$. After a first order difference is performed (as described in Eq. (82)), the spindle rotation frequencies vanish, which facilitates the estimation of the dominant chatter frequency.

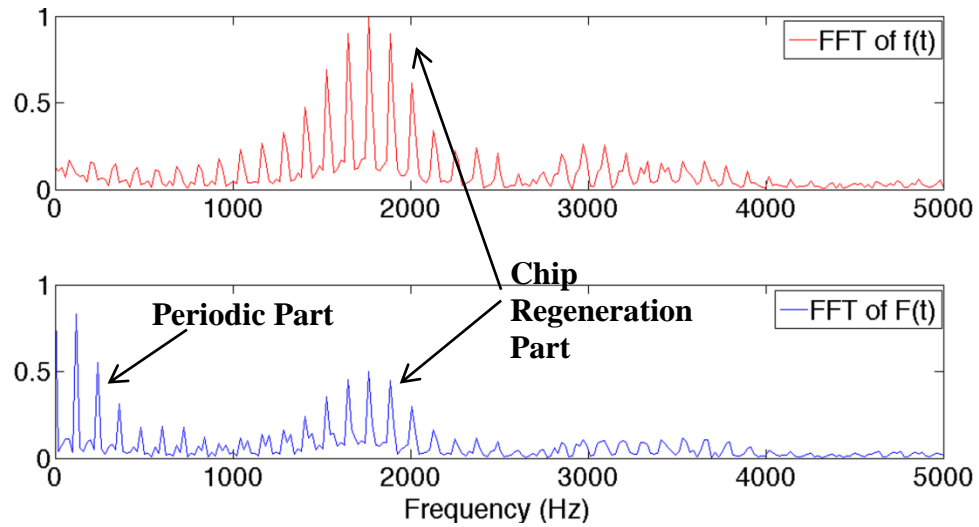


Figure. 50. Comparison of the FFT of $f(t)$ (top) and $F(t)$ (bottom).

The dominant chatter frequencies estimated by the proposed algorithm are compared with the ones estimated using FFT in Figure. 51 and Figure. 52. Note that for the sake of illustration, the spectrum of $f(t)$ estimated using the proposed algorithm is presented and the dominant chatter frequency is identified as a singular peak in the spectrum. In practice, since only the dominant chatter frequency is of interest, it is unnecessary to compute the whole spectrum. In both cases, the chatter frequency estimated using the complex exponentials model agree very well with the highest peak in the corresponding FFTs, which validates the proposed algorithm. It will be shown in the next section that the proposed algorithm is computationally more efficient.

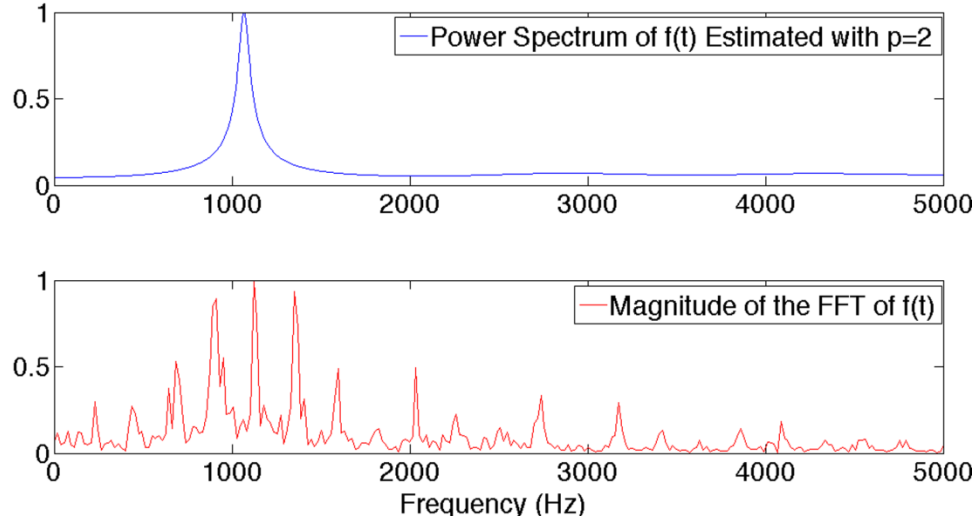


Figure. 51. Dominant chatter frequency estimated by proposed algorithm (top) and FFT (bottom) (data is from test 1).

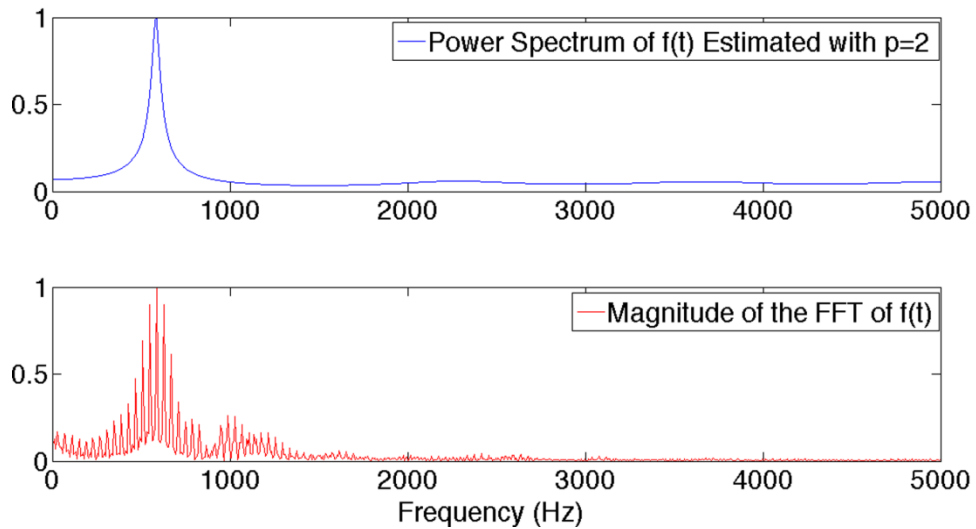


Figure. 52. Dominant chatter frequency estimated by proposed algorithm (top) and FFT (bottom) (data is from test 2).

Computational Complexity Analysis

The computational cost of the proposed chatter detection algorithm and the dominant chatter frequency estimation algorithm are detailed in Table 1. It is clear that

the number of computations needed for the proposed chatter detection algorithm is linear with the number of data available in a spindle period (i.e. the sampling rate). This is comparable with the computational cost of the wavelet transform ($O(N)$) and more efficient than FFT $O(N\log(N))$.

It is interesting to note that the computational cost of the proposed chatter frequency estimation algorithm is only a function of M , the size of the autocorrelation matrix R_f , and is independent of the data size N . On the other hand, the computational cost of the FFT is a function of the data size N . After chatter is signaled by the control chart, the number of real multiplications needs to arrive at the dominant chatter frequency using the proposed algorithm is approximately $M^3 + (M-1)^3 + M(M-p) + 1$. On the other hand, if a radix-2 FFT is adopted, the number of multiplications needed is approximately $N\log_2(N)$. As long as the following holds

$$M^3 + (M - 1)^3 + M(M - p) + 1 < N\log_2(N) \quad (97)$$

the proposed algorithm will have an advantage in computational cost. Since N is typically chosen to be a large number to achieve adequate frequency resolution in FFT, Eq. (97) is usually true. In addition, if FFT is used, $(N-1)$ comparisons are needed to locate the peak frequency in the spectrum, while for the proposed algorithm only $(M-2)$ comparisons are needed to sort all the roots. If we select $p = 2$, $M = 8$ and the number of data to be used for chatter frequency estimation is $N = 1024$, the proposed method saves approximately

9336 in the number of multiplications and 1017 in the number of comparisons. The savings in computation buys more time for taking corrective actions to suppress chatter.

Another advantage of the proposed chatter frequency estimation algorithm is the savings in memory usage. For the proposed algorithm, only the $F(t)$ sampled in the latest spindle period needs to be stored in memory for computing $f(t)$ and all the past $f(t)$ are compressed into the M independent elements in R_f . For FFT, however, not only the $F(t)$ in the latest spindle period needs to be saved for computing $f(t)$, but a buffer needs to be allocated in the memory to hold the latest N number of $f(t)$ for chatter frequency estimation.

Table 3. Computational complexity analysis of the proposed algorithm.

	Operations	Computational Costs
Chatter Detection	Differentiation (Eq. (70))	1 addition ^a per $F(t)$ sample
	Spindle period averaging (Eq. (71))	1 multiplication and addition per $F(t)$ sample
	One tap adaptive filtering (Eq. (75))	6 multiplications, 3 additions and 1 division per spindle period [121]
	Median filter (Eq. (79))	3 comparisons per spindle period
Chatter Frequency Estimation	First order difference Eq. (82)	1 addition per $F(t)$ sample
	Computation of R_f (Eq. (94))	$2M$ additions and multiplications per $F(t)$ sample when implemented recursively in time
	Eigendecomposition of R_f	$\sim M^3$ additions and multiplications
	Computation of v_{\min} (Eq. (91))	$M(M-p)$ multiplications, $M(M-p-1)$ additions, and 1 division
	Rooting a $(M-1)$ order polynomial Eq. (90)	$\sim (M-1)^3$ additions and multiplications
	Determine the dominant chatter frequency (Eq.(95))	$(M-2)$ comparisons, one multiplication

^a All computations are real.

Summary

A novel model-based and computationally efficient algorithm for incipient detection of milling chatter and estimation of the dominant chatter frequency based on the cutting force signal is presented and experimentally validated. The proposed method is shown to be capable of detecting chatter and accurately estimating the chatter frequency before chatter is fully developed. It was also found to be capable of distinguishing between chatter and transients in the cutting force caused by changes in workpiece geometry and/or tool entry/exit. The algorithm is cheaper in terms of computational cost and memory usage than frequency domain transform based methods such as FFT and can be implemented in low cost microcontrollers for on-line detection and suppression of chatter. Although the method is derived based on cutting force models, the intimate relationship between force and other types of signals suggest that it may also be applied to cutting torque and acceleration signals. Cutting torque signal is of special interest because of its directional independence with respect to tool movement. Future work will include evaluating the performance of the algorithm with tool direction-independent signals and under different cutting conditions.

CHAPTER 6 PVDF SENSOR BASED CUTTING TORQUE MEASUREMENT AND CHATTER DETECTION

Introduction

Cutting torque signal is sometimes preferred over the cutting force signal in certain milling process monitoring applications such as chatter detection along a curvilinear toolpath because of its close relationship to cutting power and its directional independency. This chapter investigates the use of the PVDF torque rosette developed in Chapter 4 to measure the dynamic component of the cutting torque in milling. The signals obtained from the PVDF torque sensor are validated torque signals acquired by a piezoelectric platform-type force dynamometer. In addition, the ability to detect chatter using the PVDF torque sensor is experimentally compared with the performance of three other sensors - piezoelectric dynamometer, accelerometer, and acoustic microphone - that are popular for chatter detection in milling. However, it must be noted that the purpose of comparison is to benchmark the PVDF torque sensor only. The comparison of other types of sensors has already been performed in prior work [49, 89].

Theory and Approach

The prototype of the PVDF torque sensor system is shown in Figure. 53. The differences between the torque sensor prototype and the prototype for in-plane cutting force measurement shown in Figure. 2 (Chapter 3) include the arrangement of the PVDF sensors and the associated signal conditioning electronics. In this prototype, four PVDF sensors are attached to the cutting tool shank and arranged according to the pattern given

in Figure. 23. The dynamic shear strain produced in the cutting tool by the milling torque is sensed by the PVDF rosette and, if needed, the milling torque can be back calculated using Eq. (49). The signal flow inside the cutting torque measurement system is the same as that shown in Figure. 3. The schematic of the signal conditioning circuit for the PVDF torque rosette is given in Figure. 28, Chapter 4.

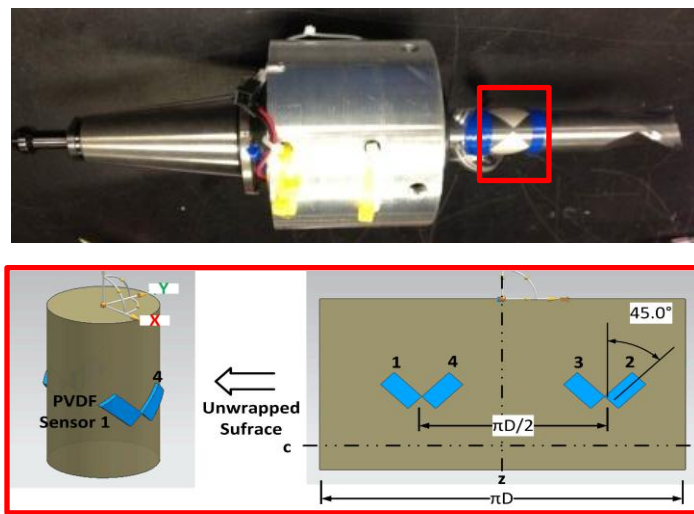


Figure. 53. PVDF sensor based cutting torque measurement prototype.

Experimental Validation

To validate the PVDF torque sensor and the associated theories, it is necessary to experimentally compare the signals acquired from the PVDF torque sensor with reliable measurements of the cutting torque. Since a milling torque dynamometer is currently not available in the Precision Machining Lab at Georgia Tech, it is proposed to compute a reference cutting torque signal from the in-plane cutting force signals measured from a platform type dynamometer (Kistler 9257B), against which the signal measured using the

PVDF torque sensor is compared. The way that the reference signal is computed is detailed in the following section.

Computation of the reference signal from in-plane force signals

As shown in Figure. 54, when only one tooth of a straight flute end mill is engaged in cutting, the forces seen by the dynamometer during the cutting process in the workpiece coordinate system (X-Y) can be resolved into the tool coordinate system (R-T). The tangential force F_t applied to the workpiece by the engaging tooth is given by

$$F_t = F_x \sin \theta - F_y \cos \theta \quad (98)$$

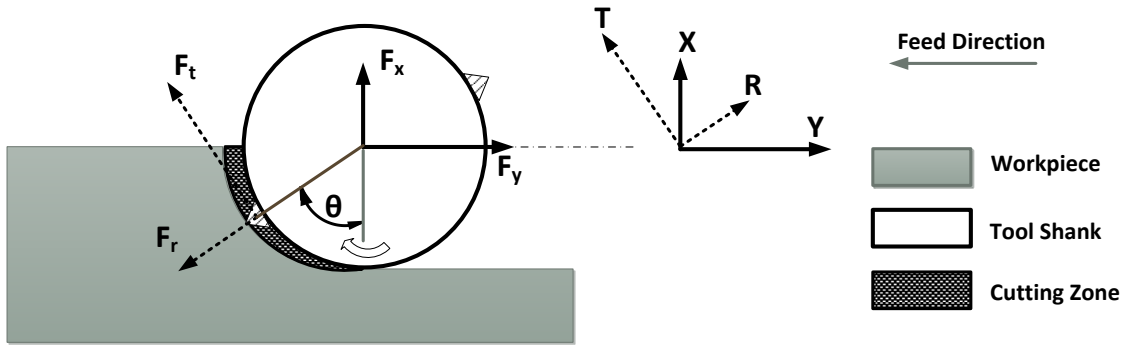


Figure. 54. Cutting forces in workpiece coordinate system and tool coordinate system.

where θ denotes the angular position of the cutting tool in the workpiece coordinate system (X-Y). Since F_x and F_y are measured by the dynamometer, the tangential cutting force F_t can be determined as long as θ is known for each discrete sample of the dynamometer force signal. To find θ , we notice that the transverse cutting force F_x can be represented in terms of the tangential cutting force F_t and the radial force F_r as

$$F_x = F_t \sin \theta - F_r \cos \theta \quad (99)$$

According to linear mechanistic models for cutting force, [8], assuming negligible tool runout, we have

$$\begin{aligned} F_t &= K_c s_t \sin \theta \\ F_r &= \eta F_t \end{aligned} \quad (100)$$

where K_c is the specific cutting pressure, s_t is the feed per tooth and η is the ratio between the radial force and the tangential cutting force and can be assumed to be constant for a specific combination of workpiece and tool materials under a particular cutting condition. The linear model given in Eq. (100) is only valid under certain assumptions and a more detailed explanation has been given in the Methodology section of Chapter 5. Substituting Eq. (100) into Eq. (99):

$$F_x = K_c s_t \sin \theta (\sin \theta - \eta \cos \theta) \quad (101)$$

Clearly F_x is a monotonically increasing function of θ in the range of 0° to 90° because $\sin \theta$ and $\cos \theta$ monotonically increase and decrease with θ between 0° to 90° , respectively. In peripheral milling with a radial immersion of less than 50%, the

maximum possible θ in any tooth period is less than 90° and is reached only when the engaging tooth exits the workpiece. Therefore, during each tooth period the transverse force F_x reaches its maximum when θ reaches the tooth exit angle. Since the tooth exit angle θ_{EX} can be easily determined from the radial depth of cut r and the cutting tool diameter R as

$$\theta_{EX} = \cos^{-1}\left(\frac{R-r}{R}\right) \quad (102)$$

the angular positions of all other sampling points that are adjacent to the maximum transverse force point can be calculated accordingly with the knowledge of the sampling frequency and the nominal spindle rotation speed. The tangential cutting force F_t can then be computed using Eq. (98) and the cutting torque is simply the tangential cutting force multiplied by the radius of the cutting tool.

Note that in actual cutting experiments, a helical end mill is used instead of a straight flute end mill and the maximum transverse force does not occur exactly at the tooth exit angle. Instead, the maximum transverse force point is expected to be slightly ahead of the tooth exit point by an angle of λ , where λ is given by

$$\lambda = a \tan \phi / R \quad (103)$$

where is R the cutting tool radius, a is the axial immersion and ϕ is the helix angle. To reduce the effect of the helix angle, the axial immersion in all cutting experiments is set to be less than or equal to 30% of the tool radius. It is also worth mentioning that the tool exit angle can be affected by the cutter radial runout [132].

Comparison of the PVDF sensor signal with the reference signal

A set of peripheral end milling experiments was performed to experimentally validate the proposed cutting torque measurement system. A Kistler 9257B dynamometer was used to independently collect the in-plane cutting force signals in all experiments. The cutting tool used was a two flute solid carbide end mill of 25.4mm diameter. All other cutting conditions are tabulated in Table 4. The PVDF torque sensor is sampled at a frequency of 12KHz and the Kistler dynamometer was sampled at 10KHz. For validation purposes, the unknown material and geometric constants in Eq. (49) are combined into a single sensitivity coefficient K_s . In Eq.(49), the shear strain γ can be related to the torque by

$$\gamma = \frac{TR}{GI_p} \quad (104)$$

where T is the torque applied on the cutting tool, R is the radius of the cutting tool, G is the shear modulus of the cutting tool material and I_p is the polar moment of inertia of the cross section of the cutting tool at the location where the sensors are attached. Ignoring

the possible residual thermal strains in Eq. (49) and substituting Eq. (104) into Eq. (49),

K_s can be defined as

$$K_s = \frac{[d_{31}Y_1(1-\nu_{21}) - d_{32}Y_2(1-\nu_{12})] DA_3}{(1-\nu_{21}\nu_{12})C_F} \frac{1}{GI_p} \quad (105)$$

so that the PVDF sensor rosette output V can be related to the cutting torque T as

$$V = K_s T \quad (106)$$

In this work, the sensitivity coefficient K_s is determined to be 2.386 mV/N•m in the first cutting test and used in all following tests.

Table 4. Cutting conditions for cutting torque measurement.

Test No.	Spindle Speed (rpm)	Immersion Ratio	Depth of Cut (mm)	Feed per Tooth (mm)	Workpiece Material
1	1500	50%	1.905	0.0254	AL 7050 ^a
2	1800	50%	1.905	0.0254	AL 7050
3	2100	50%	1.905	0.0254	AL 7050
4	1500	25%	2.540	0.0254	AL 7050
5	1800	25%	2.540	0.0254	AL 7050
6	2100	25%	2.540	0.0254	AL 7050
7	2400	25%	2.540	0.0254	AL 7050
8	1800	34%	2.540	0.0254	AL 7050
9	1800	25%	1.905	0.0254	AL 7050
10	2100	25%	1.905	0.0254	AL 7050
11	2400	25%	1.905	0.0254	AL 7050
12	1200	25%	3.810	0.0254	ST 1018
13	1500	25%	3.810	0.0254	ST 1018

a AL 7050 denotes Aluminum 7050 and ST 1018 denotes 1018 Steel.

Representative results for the different cutting conditions and workpiece materials are given in Figures. 54-58. Backward comparison is used to compare the PVDF sensor signal and the reference signal. Details of how backward comparison is performed can be found in Chapter 3. Note that only the dynamic component of the cutting torque is involved in the backward comparison. It can be seen from Figure. 55 to Figure. 59 that reasonably good agreement is achieved between the two signals in terms of the general trends across different cutting conditions and workpiece materials. This validates the PVDF torque sensor rosette design, the associated quantitative models for the PVDF sensors, and the sensor prototype.

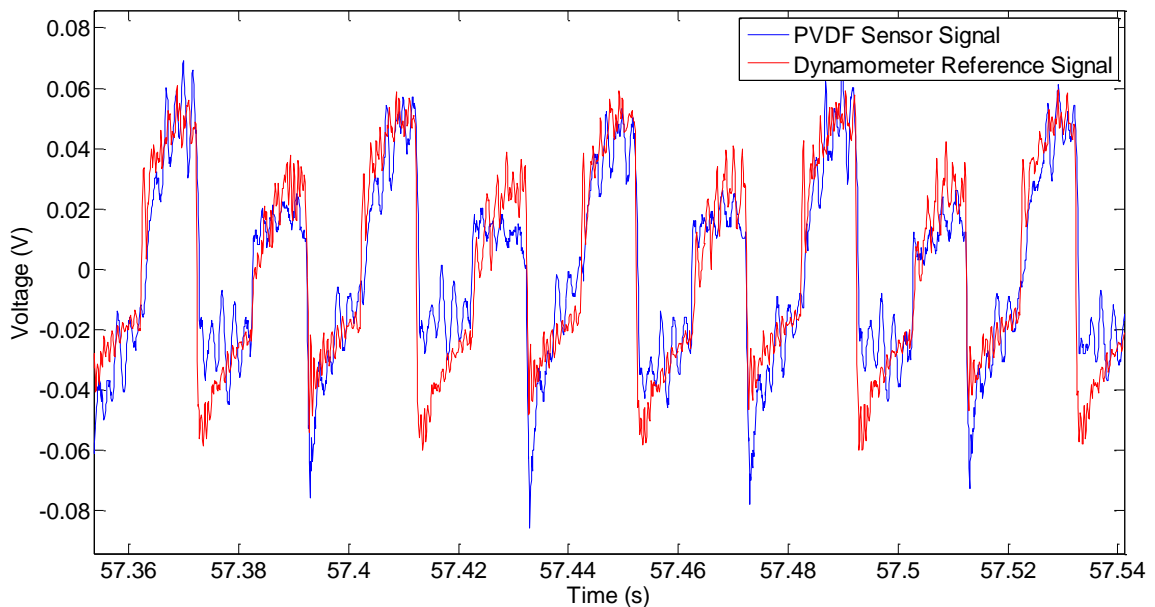


Figure. 55. Backward comparison of PVDF sensor signal with reference signal (cutting conditions: two flute 25.4 mm carbide tool, Aluminum 7050 workpiece, 1500 RPM, 0.0254 mm feed/tooth, 50% radial immersion, 1.905 mm depth of cut).

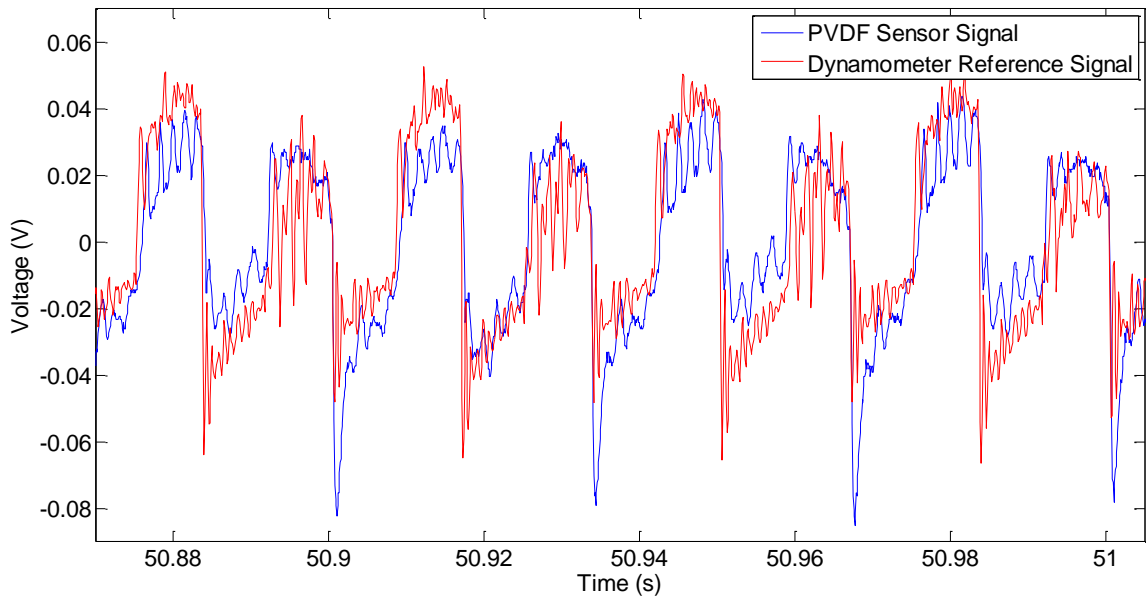


Figure. 56. Backward comparison of PVDF sensor signal with reference signal (cutting conditions: two flute 25.4 mm carbide tool, Aluminum 7050 workpiece, 1800 RPM, 0.0254 mm feed/tooth, 50% radial immersion, 1.905 mm depth of cut).

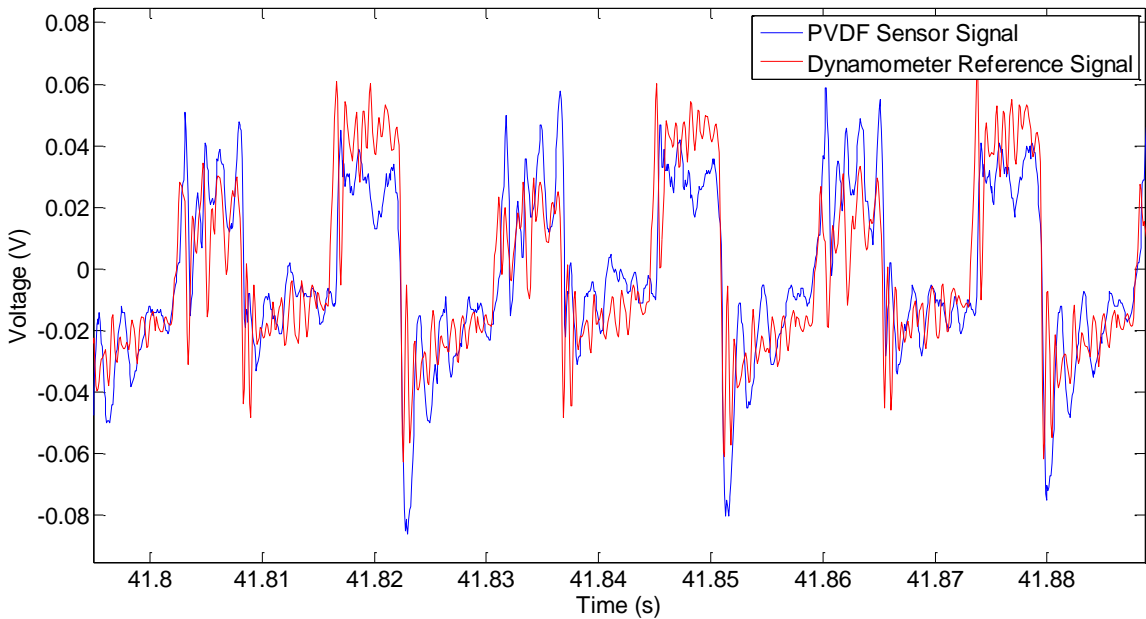


Figure. 57. Backward comparison of PVDF sensor signal with reference signal (cutting conditions: two flute 25.4 mm carbide tool, Aluminum 7050 workpiece, 2100 RPM, 0.0254 mm feed/tooth, 50% radial immersion, 1.905 mm depth of cut).

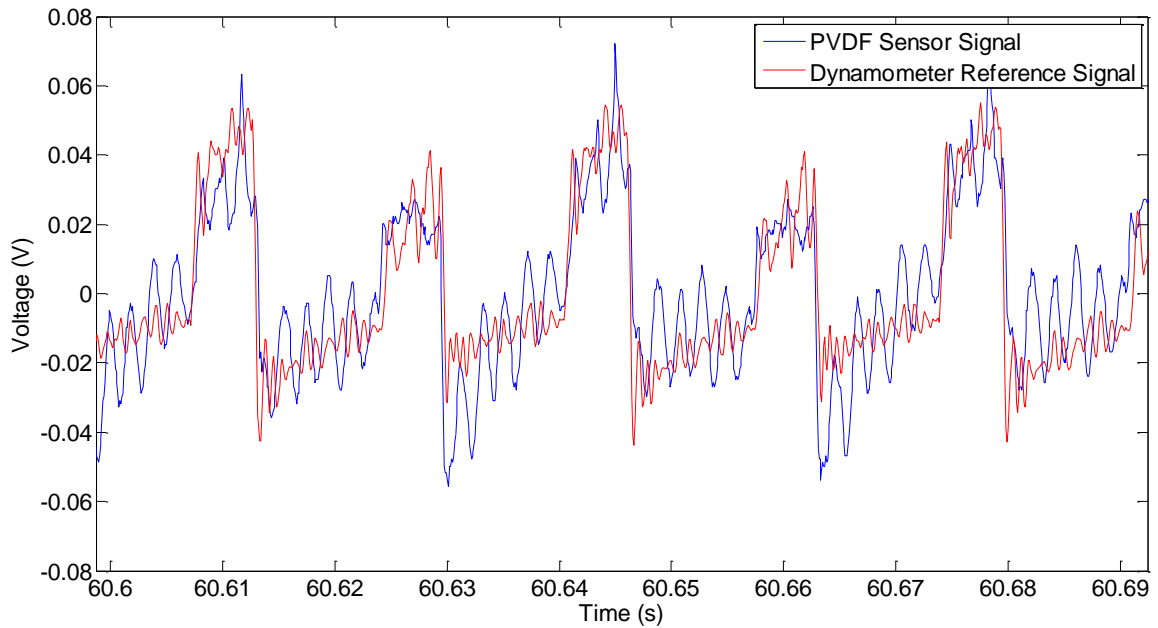


Figure. 58. Backward comparison of PVDF sensor signal with reference signal (cutting conditions: two flute 25.4 mm carbide tool, Aluminum 7050 workpiece, 1800 RPM, 0.0254 mm feed/tooth, 25% radial immersion, 2.540 mm depth of cut).

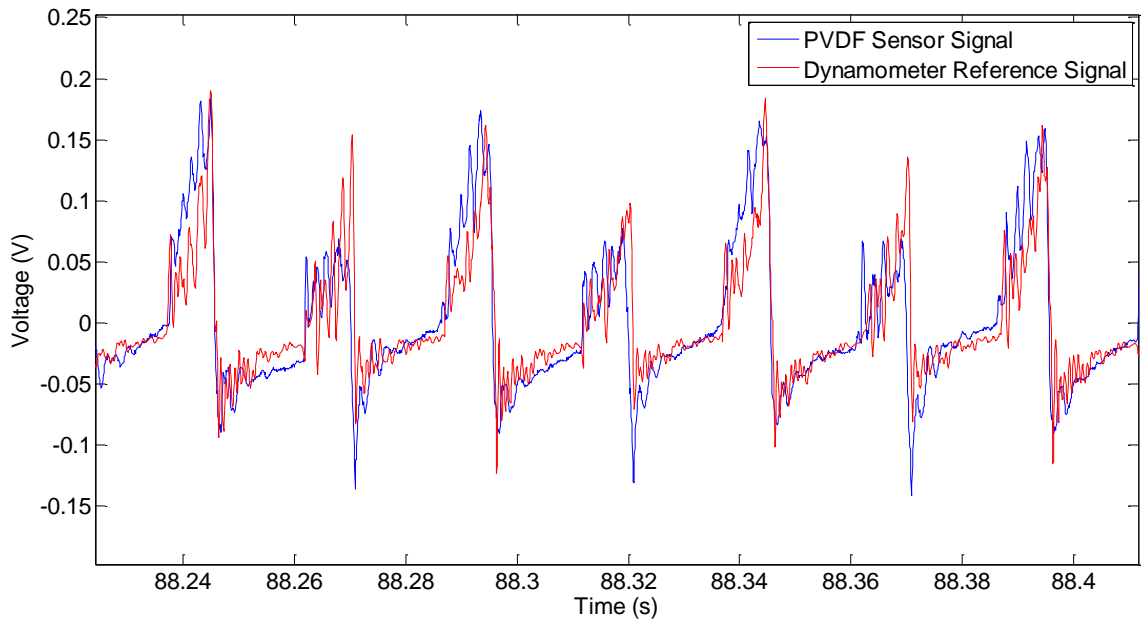


Figure. 59. Backward comparison of PVDF sensor signal with reference signal (cutting conditions: two flute 25.4 mm carbide tool, 1018 Steel workpiece, 1200 RPM, 0.0254 mm feed/tooth, 25% radial immersion, 3.81 mm depth of cut).

Discussion on the discrepancy

While the agreement between the PVDF torque sensor signals and the reference cutting torque signals is reasonable, it is not as good as the agreement between the as-measured PVDF sensor signals and the cutting force signals presented in Chapter 3. The discrepancy between the two can be attributed to two sources: 1) from the reference signal side, inaccuracies in the estimated angular positions of the engaging tooth due to the helix angle of the tool, the cutter radial runout and the noise and transients in the measured dynamometer signals, and 2) from the PVDF sensor signal side, imperfect positioning of the PVDF sensors on the cutting tool shank that leads to the incomplete cancellation of the bending strains, axial strains and thermal strains. These residual strains will result in spurious oscillations in the PVDF sensor signal, especially when no cutting tooth is engaged with the workpiece. An additional contribution to the discrepancy includes the variation of material properties of the four PVDF sensors in the rosette due to manufacturing process uncertainties. It is expected that better agreement between the two signals can be achieved by positioning the four PVDF sensors in a more precise way.

Characterization of Different Sensors for Chatter Detection

As the first step in comparing the PVDF torque sensor with other sensors, the frequency response functions (FRF) of the three sensors, i.e. the acoustic microphone, the piezoelectric dynamometer and the piezoelectric accelerometer, are first studied.

Acoustic microphone

A Knowles piezoelectric microphone is used in this work because it provides a flat frequency response from 20Hz to 10KHz, whereas the more common electret condenser microphone is typically only usable above 100Hz. The microphone sensor assembly is shown in Figure. 60 and the signal conditioning circuit is shown in Figure. 61. The whole sensor assembly is mounted on a tripod with adjustable height.

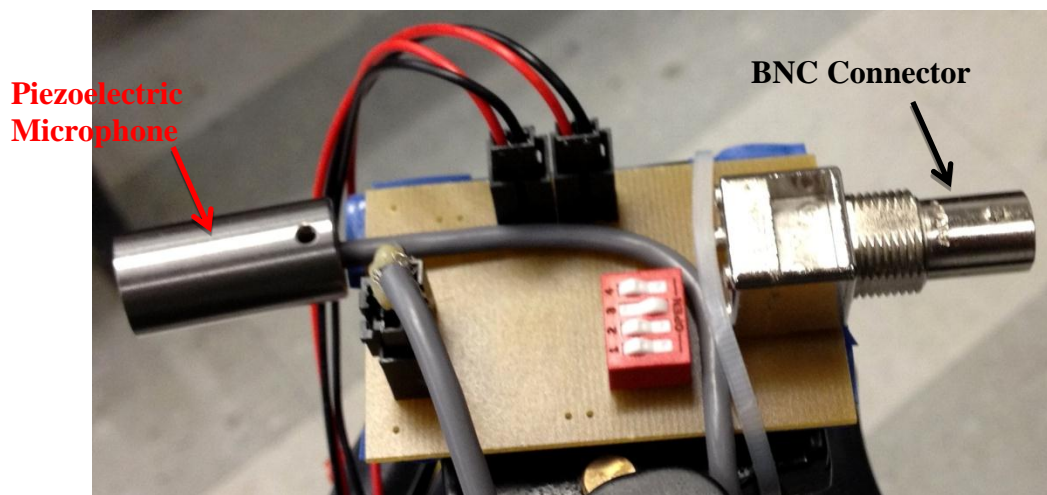


Figure. 60. Experimental set-up of the piezoelectric microphone.

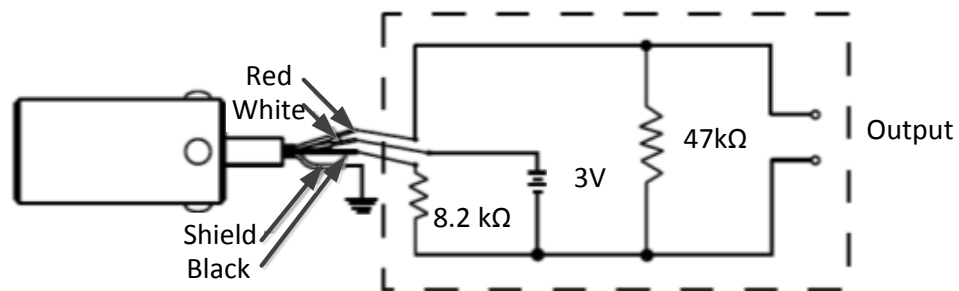


Figure. 61. Schematic of the signal conditioning circuit for the microphone.

The FRF of the piezoelectric microphone from the manufacturer datasheet is given in Figure. 62. Due to the low sensitivity of the piezoelectric microphone (3.5 mV/Pa at 1000 Hz), the signal from the piezoelectric microphone is amplified 100 times using an instrumentation amplifier before it is sampled by the data acquisition system.

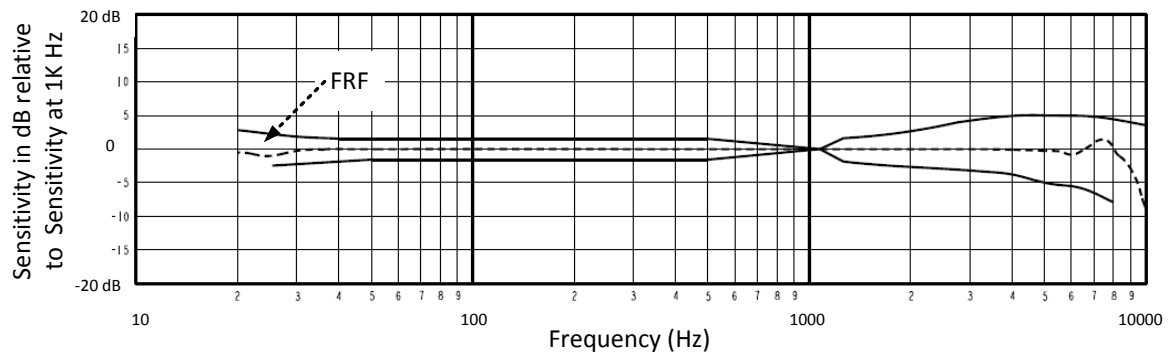


Figure. 62. Frequency response function of the piezoelectric microphone [133].

Piezoelectric dynamometer

The set-up of the piezoelectric dynamometer (Kistler 9257B) with the workpiece mounted is shown in Figure. 63. Experimental modal analysis was performed to determine the FRF of this system. An impact hammer was used to excite the structure in the X/Y direction and the response of the piezoelectric dynamometer in the X/Y direction was recorded, from which the FRF in the X/Y direction can be determined. The point of impact is also indicated in Figure. 63. A total of 25 tests were performed and recorded for each direction and a least squares method [114] was used to find the FRFs of the system, as shown in Figure. 64. It can be seen that the first modes in the X and Y directions are at

1250 Hz and 900Hz, respectively. The useable bandwidth for measurement in the X and Y directions is about 900 Hz and 500 Hz, respectively. Note that during the milling process, material is removed from the workpiece in the form of chips and the FRF of the workpiece mounted dynamometer system may vary over time. Also, the point where the cutting force is applied during the milling process is time varying and is, in general, different from the point of impact in the experimental modal test.

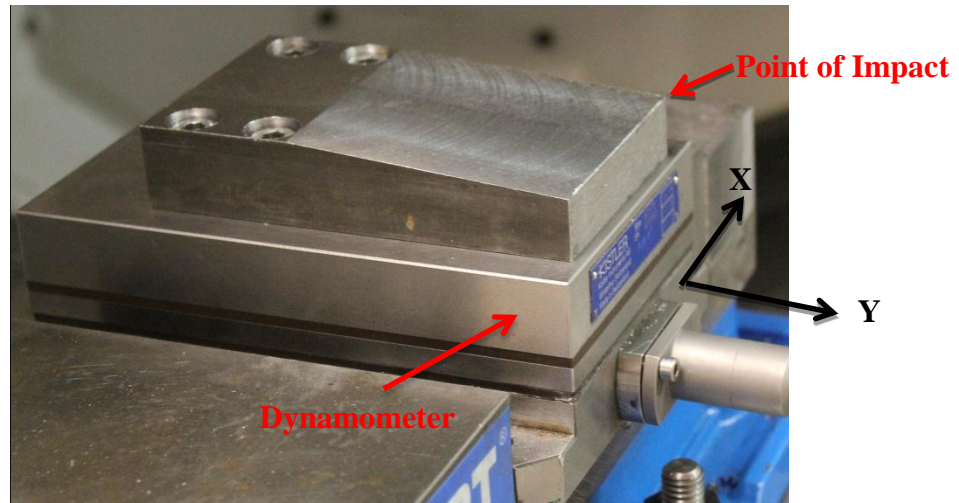


Figure. 63. Experimental set-up of the piezoelectric dynamometer.

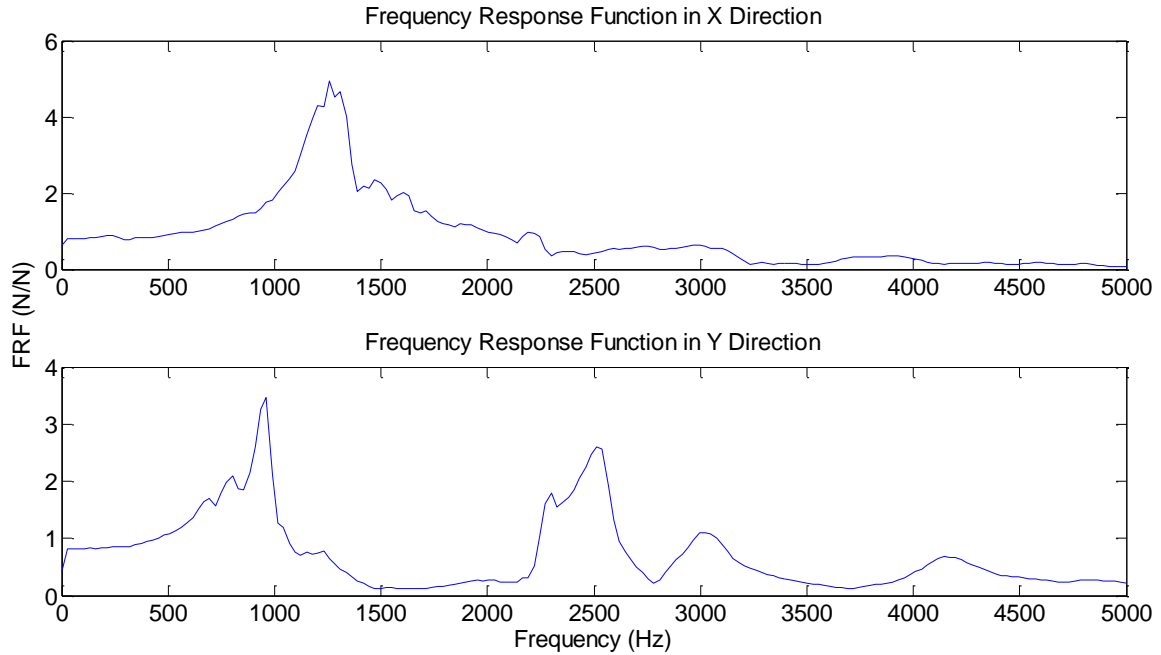


Figure. 64. Frequency Response Functions of the workpiece-mounted dynamometer in the X and Y directions.

Accelerometer

In this work, two uniaxial piezoelectric accelerometers (Kistler 8636C50) were mounted on the piezoelectric dynamometer to measure the vibration produced during the cutting process in two orthogonal directions, as shown in Figure. 65. The accelerometers were mounted on the dynamometer system instead of the workpiece to 1) avoid overloading the accelerometers and to 2) minimize variations in the positions of the accelerometers when different workpiece samples are used. Since the accelerometer itself has a much wider bandwidth compared to the structure on which it is mounted, the FRF obtained from the experimental modal test simply reflects the structural dynamics of the workpiece-dynamometer-workpiece holder-machine tool structure system.

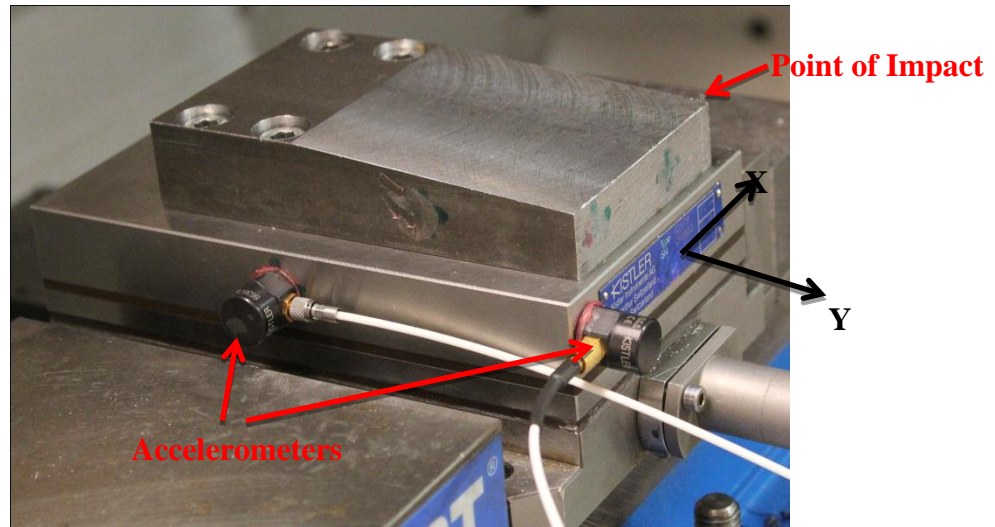


Figure. 65. Experimental set-up of workpiece mounted accelerometers.

Similar to the piezoelectric dynamometer, an impact hammer was used to excite the structure in X/Y directions and the response of the accelerometers in the X/Y directions was measured, from which the FRF in the X/Y directions were determined. The obtained FRFs are given in Figure. 66. The first natural mode in the X and Y directions is about 1200 Hz and 700 Hz, respectively. Note that during milling the point where the cutting force is applied is time varying and is, in general, different from the point of impact in the experimental modal test.

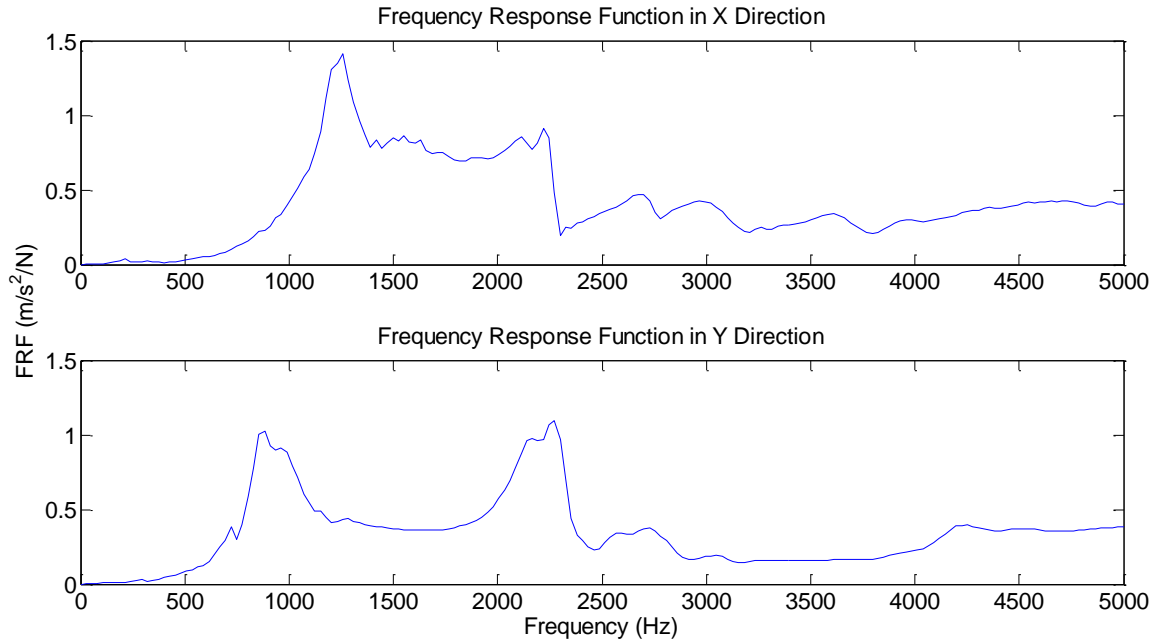


Figure. 66. Frequency response functions of the workpiece-mounted accelerometer in the X and Y directions.

Chatter Experiments and Results

A set of milling experiments is performed to compare the performance of the PVDF torque sensor and three other sensors - piezoelectric dynamometer, accelerometer and acoustic microphone - for chatter detection in milling. During the experiments, the PVDF sensor is sampled at 12KHz and all the other sensors are sampled at 20KHz. The cutting tool is a 25.4 mm diameter two flute solid carbide end mill and the workpiece material is 1018 steel. All other cutting conditions are tabulated in Table 5

Table 5. Cutting conditions for chatter test with PVDF sensor.

Test No.	Spindle Speed (RPM)	Radial Immersion	Feed per Tooth (mm)	Axial Depth of Cut (mm)
1	1200	25%	0.0381	Increasing linearly from 0 to 5.95
2	1200	50%	0.0381	Increasing linearly from 0 to 5.95
3	1200	50%	0.0381	Increasing in steps from 1.27 to 6.35 to 11.43

Spurious Peaks

In the PVDF torque sensor prototype, four individual PVDF sensors need to be attached to the tool shank in a predetermined pattern to form the torque rosette. Since the commercially available PVDF sensors used in this study were too large to fit onto a 25.4 mm diameter cutting tool, their size was reduced by cutting away part of the sensors. Consequently, both the sensor material and the electrodes are exposed and deformed along the line of cutting and possible shorting of the two electrodes can occur. The capacitance and resistance between the two electrodes of the cut sensors can be measured to check if any short between the electrodes exists right after they are cut. However, it turns out that after the cut sensors are attached to the cutting tool shank, compressive bending stress produced by the cutting force at the location of the sensors can still cause the exposed electrodes to temporarily contact each other, thus resulting in randomly distributed spurious peaks in the measured PVDF sensor signal. One example of the PVDF sensor signal with spurious peaks is shown in Figure. 67.

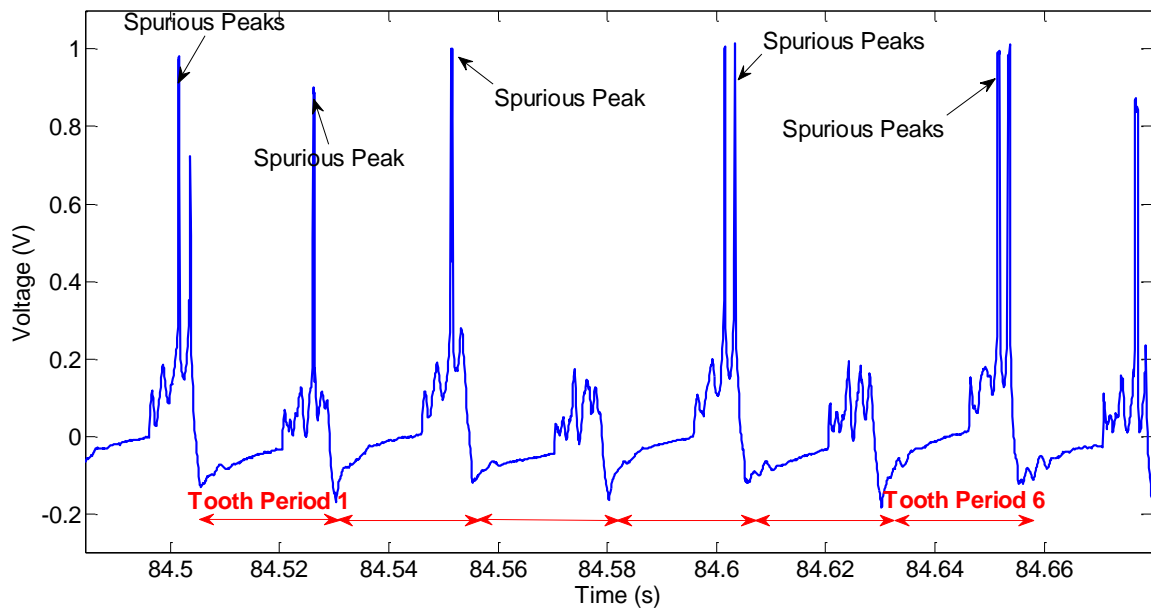


Figure. 67. Spurious peaks in the PVDF sensor torque signal.

It can be seen in Figure. 67 that the number of spurious peaks in one tooth period ranges from 0 to 2. If the chatter detection algorithm developed in Chapter 5 is applied to the measured PVDF sensor signal, the random variation in the number of spurious peaks per tooth period will result in large oscillations in the spindle period averaged signal, thus leading to false alarms. Therefore, to detect chatter with the PVDF torque sensor using the algorithm developed in this work, it is critical to have well packaged PVDF sensors of customizable size that can fit on regular size cutting tools.

Comparison of the performance of different sensors

Due to the spurious peaks in the PVDF torque sensor signal, it is not feasible to compare the PVDF sensor against the other sensors using the chatter detection algorithm developed in this work. Instead, the four sensors will be compared using the fundamental signal processing method: the Fourier Transform. While Fourier Transform cannot

identify the point where chatter occurred because the eigenfunctions used to decompose the signal have infinite time support, it can indicate the presence of chatter vibration, if any, in a time averaged sense. In other words, it measures how chatter vibration is captured by the sensors relative to other frequency contents.

Test 1: The frequency spectrums of the signals obtained from all four types of sensors used in Test 1 are given in Figures. 67-70. For comparison, all the spectrums are normalized by the amplitude of the maximum frequency peak seen in the spectrum in question. This convention is followed in all results that follow.

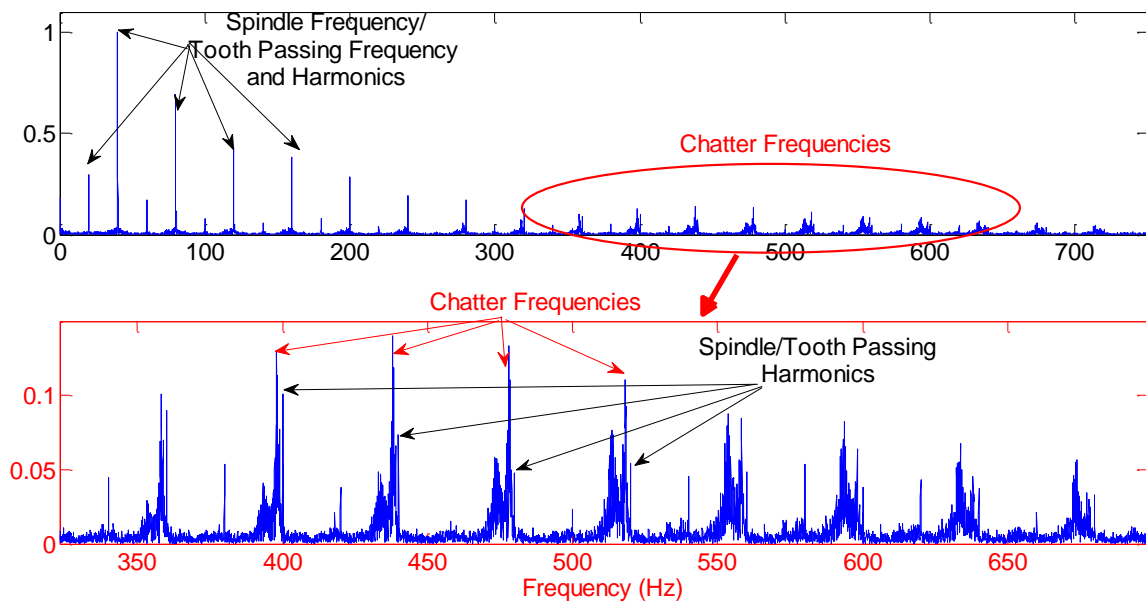


Figure. 68. Frequency decomposition of the PVDF sensor signal (Test 1).

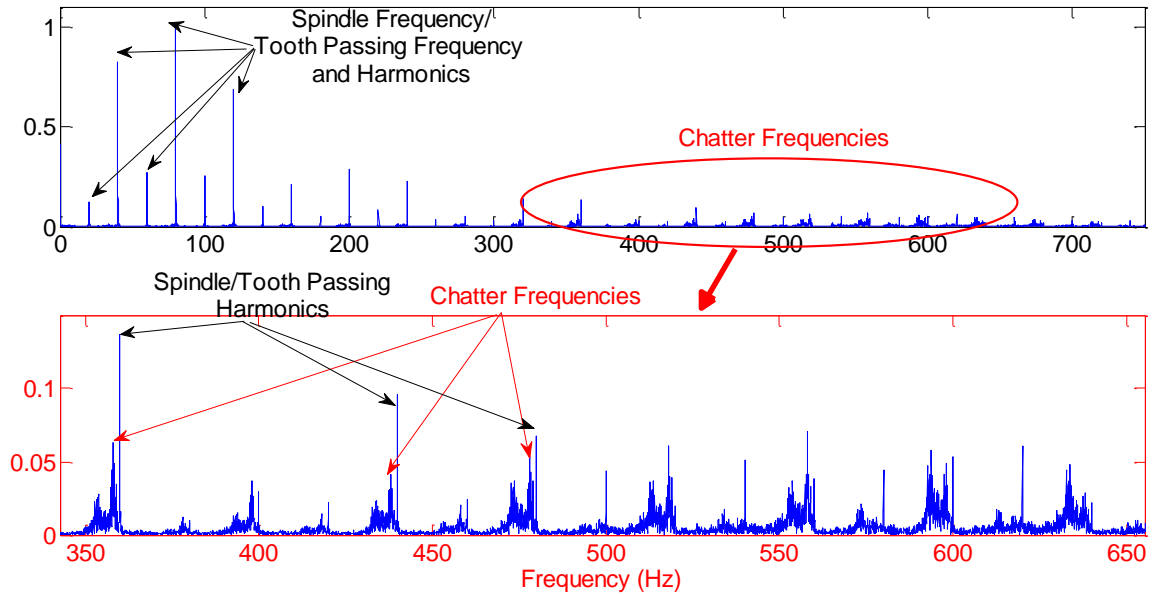


Figure. 69. Frequency decomposition of the dynamometer force signal (Test1, force in X direction).

It can be seen from Figure. 68 and Figure. 69 that the spectrum of the PVDF sensor signal is similar to that of the dynamometer force signal, especially at the spindle frequency, tooth passing frequencies and their harmonics. This similarity is expected because during the periodic engagement of the cutting tool with the workpiece, the forced vibration at the spindle speed related frequencies will directly impact both sensors (by causing dynamic strain in the cutting tool where the PVDF sensors are attached and by introducing periodic displacement in the quartz crystal inside the dynamometer), resulting in strong peaks at those frequencies. Also, this similarity explains why reasonably good agreement is achieved between the PVDF torque sensor signal and the reference cutting torque signal under stable cutting conditions in the first section of this chapter. However, it is also noticed that the PVDF sensor picks up the chatter frequency peaks slightly better than the dynamometer. The amplitude of the strongest chatter frequency peak is 14% of the strongest peak in the PVDF sensor signal, while for the

dynamometer signal this ratio is about 6%. In addition, the chatter peaks in the PVDF signal compare favorably with their neighboring harmonics of the spindle frequencies and tooth passing frequencies, whereas in the dynamometer signal the chatter peaks are overshadowed by adjacent harmonics. The likely reason for this is that after the cutting tool exits the workpiece in one tooth period, the free vibration of the tool and workpiece will continue to impact the responses of the PVDF sensor and the dynamometer. However, since in end milling the cutting tool tends to be the most flexible link in the cutting tool-workpiece-dynamometer-machine tool system, the response of the PVDF sensor is stronger. The difference between the two sensors in picking up the chatter frequencies is expected to be significant for low radial immersion cuts and insignificant in high radial immersion cuts.

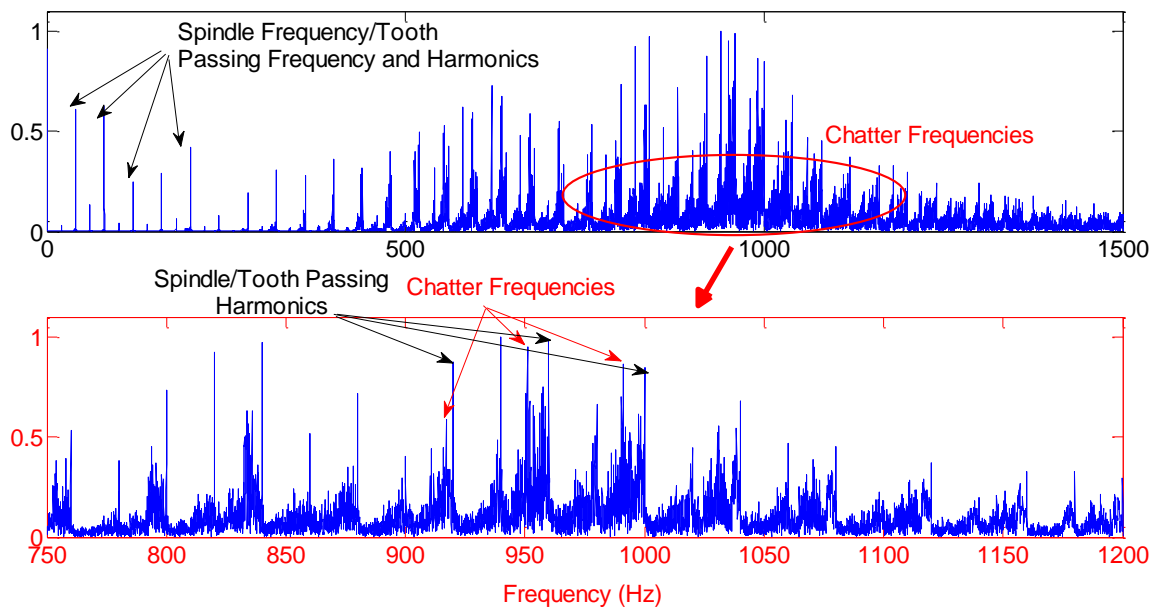


Figure. 70. Frequency decomposition of the accelerometer signal (Test1, the acceleration in X direction).

The spectrum of the accelerometer signal agrees well with the experimentally obtained FRF shown in Figure. 66, i.e., the frequency contents between 500 Hz and 1200 Hz are amplified by the first mode. Due to this amplification, the amplitude of the maximum chatter frequency peak is 80% of the amplitude of the maximum peak, which, instead of being the tooth passing frequency, is a harmonic of the tooth passing frequency that falls around the first mode of the FRF of the accelerometer.

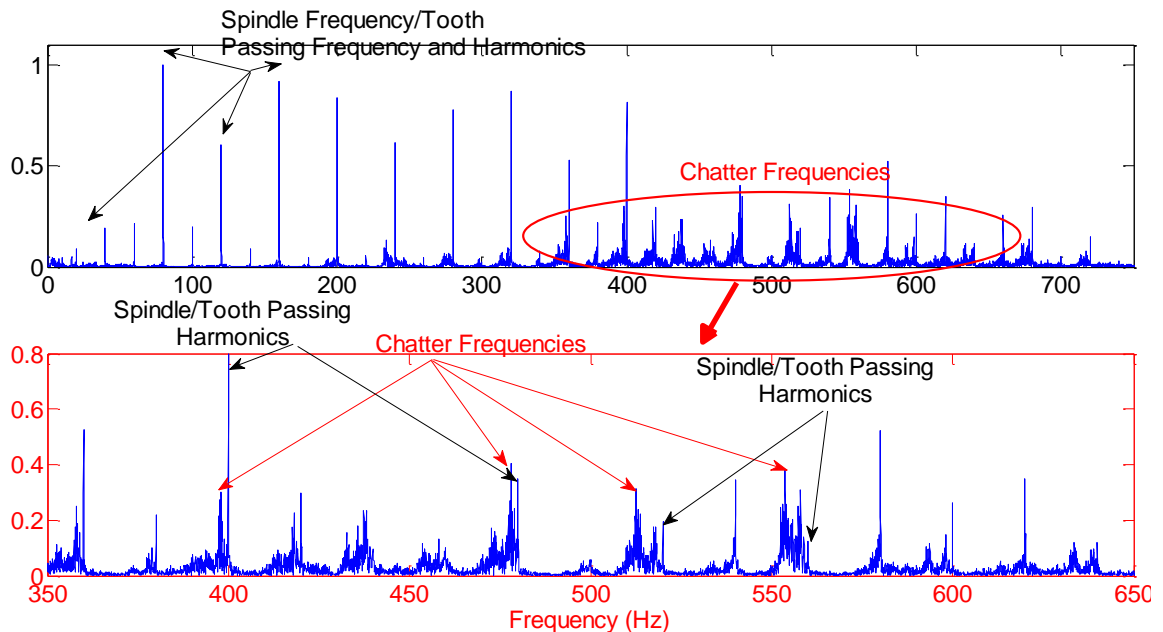


Figure. 71. Frequency decomposition of the microphone signal (Test1).

The microphone sensor faithfully reflects the sound pressure received by the sensor between 20Hz-10,000Hz because of its relatively flat frequency response. The maximum chatter frequency peak reaches 40% of the amplitude of the maximum frequency seen in the signal. One noticeable difference between the microphone signal and the accelerometer signal is that the noise level around the maximum chatter peak in

the accelerometer signal is much higher than that in the microphone signal, largely because the noise is also amplified by the first mode of the accelerometer system.

Test 2 The spectra of the PVDF sensor signal and the dynamometer force signal collected during Test 2 are shown in Figure. 72 and Figure. 73, respectively. Similar to the observations from Test 1, the PVDF sensor signal and the dynamometer force signal are very similar in capturing the frequency content at the spindle frequency, tooth passing frequency and their harmonics. In terms of the chatter frequencies, the strongest chatter peak in the PVDF sensor signal is about 3% of the strongest peak in the signal, and the ratio for the dynamometer signal is 2%. Also, the ratio between the chatter frequency peaks and their neighboring spindle speed related harmonics are also very similar for the two signals, which is probably due to the increased radial immersion compared to Test 1.

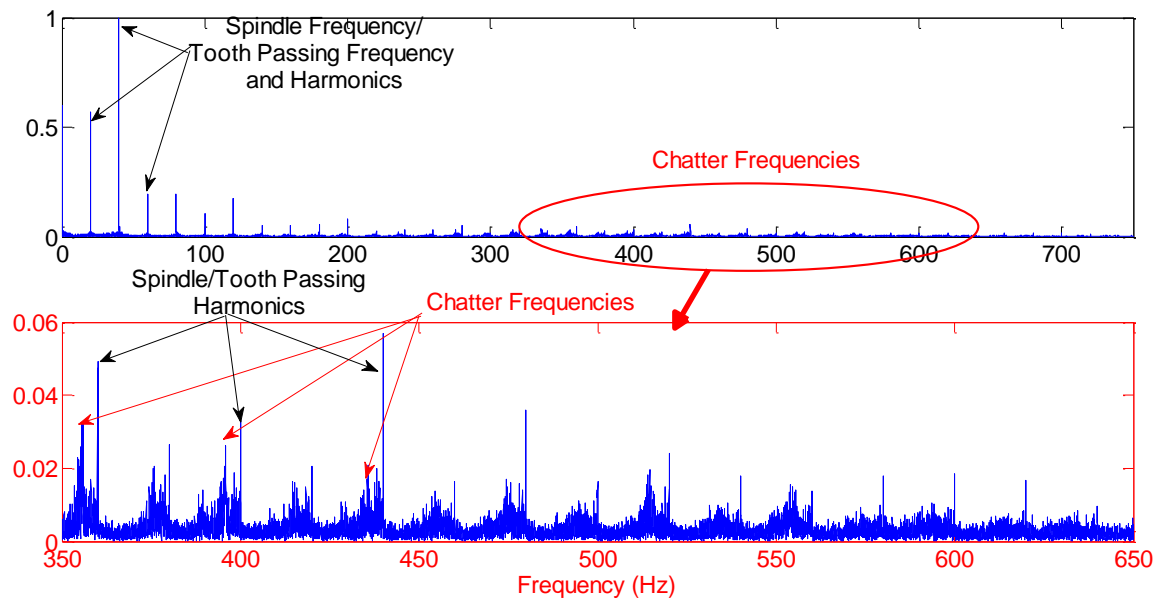


Figure. 72. Frequency decomposition of the PVDF sensor signal (Test 2).

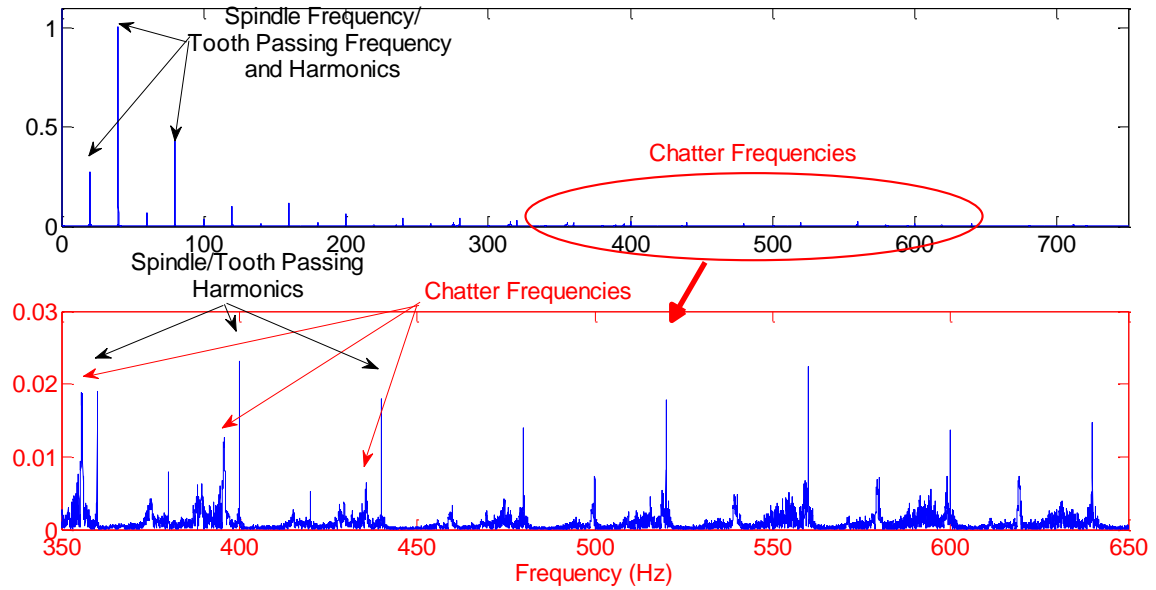


Figure. 73. Frequency decomposition of the dynamometer force signal (Test 2, the force in X direction).

The Fourier transforms of the accelerometer signal and the microphone signal collected during Test 2 are shown in Figure. 74 and Figure. 75, respectively. Similar to the observations from Test 1, very strong chatter peaks are observed in transforms of the two sensor signals, which are up to 40% of the strongest peak in the accelerometer signal and 60% of the strongest peak in the microphone signal. Again, a higher noise floor is observed around the maximum chatter frequency peak in the accelerometer signal.

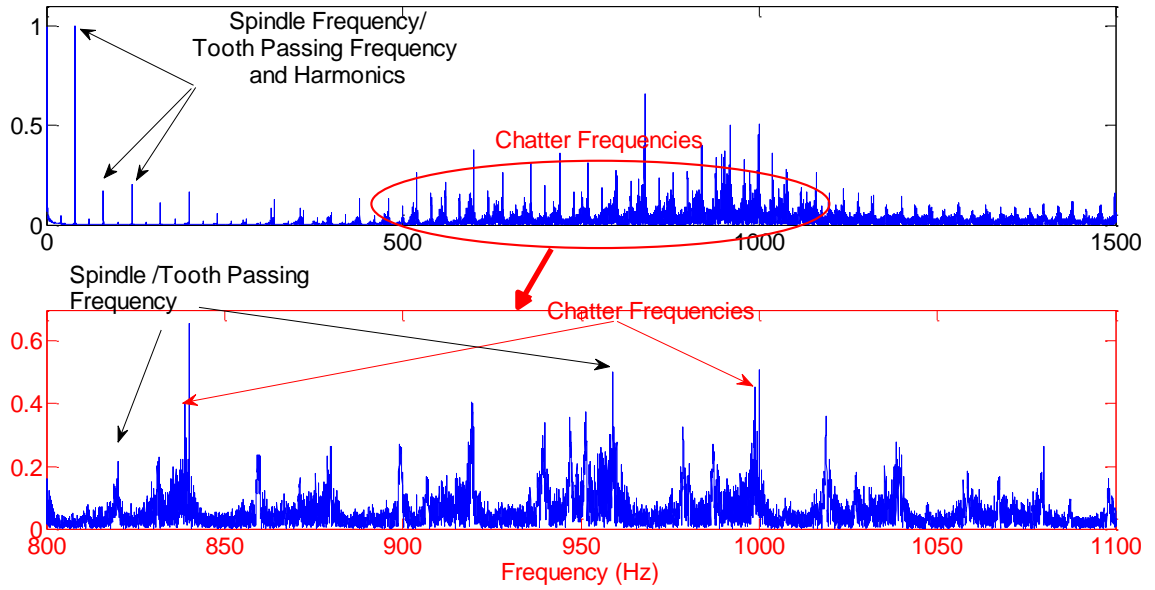


Figure. 74. Frequency decomposition of the accelerometer signal (Test 2, the acceleration in the X direction).

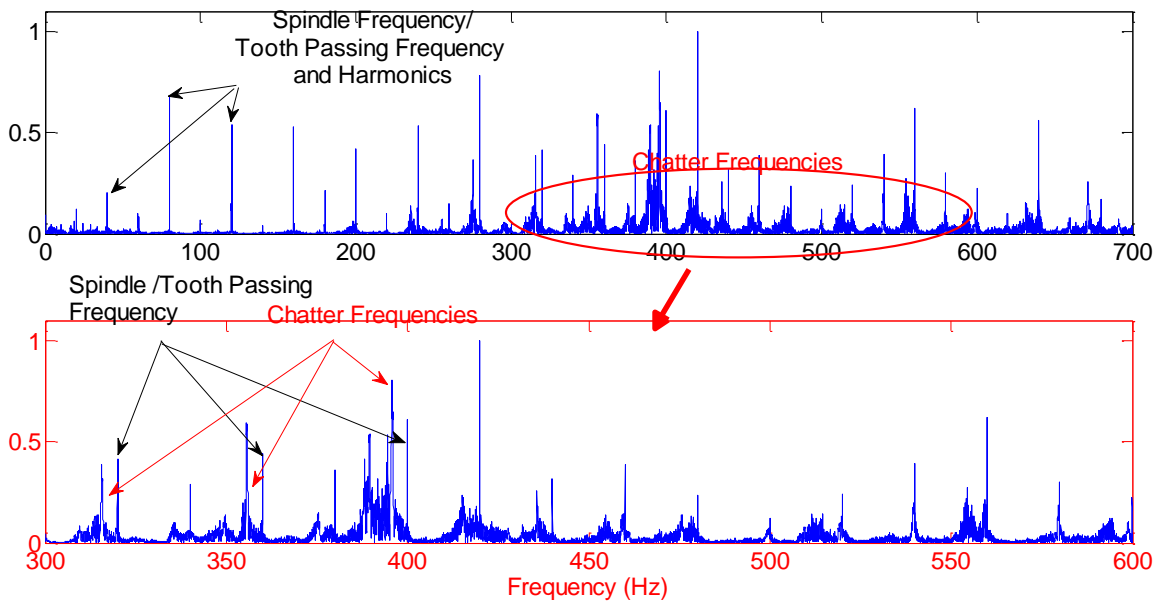


Figure. 75. Frequency decomposition of the microphone signal (Test 2).

Test 3 The spectra of all four sensor signals collected in Test 3 are shown in Figures. 75-78. Since Test 3 has the same radial immersion as Test 2, the observations from the two tests are also similar. The chatter peaks in the PVDF sensor signal and the dynamometer signal overshadow their neighboring harmonics of spindle speed related frequencies. However, the PVDF sensor outperforms the dynamometer in terms of the normalized amplitude of the chatter peak. The accelerometer and the microphone continue to deliver superior performance in capturing the chatter frequency peaks, as evident in Figure. 78 and Figure. 79. Also, very high signal to noise ratio is achieved in the microphone signal, especially when compared to the accelerometer signal.

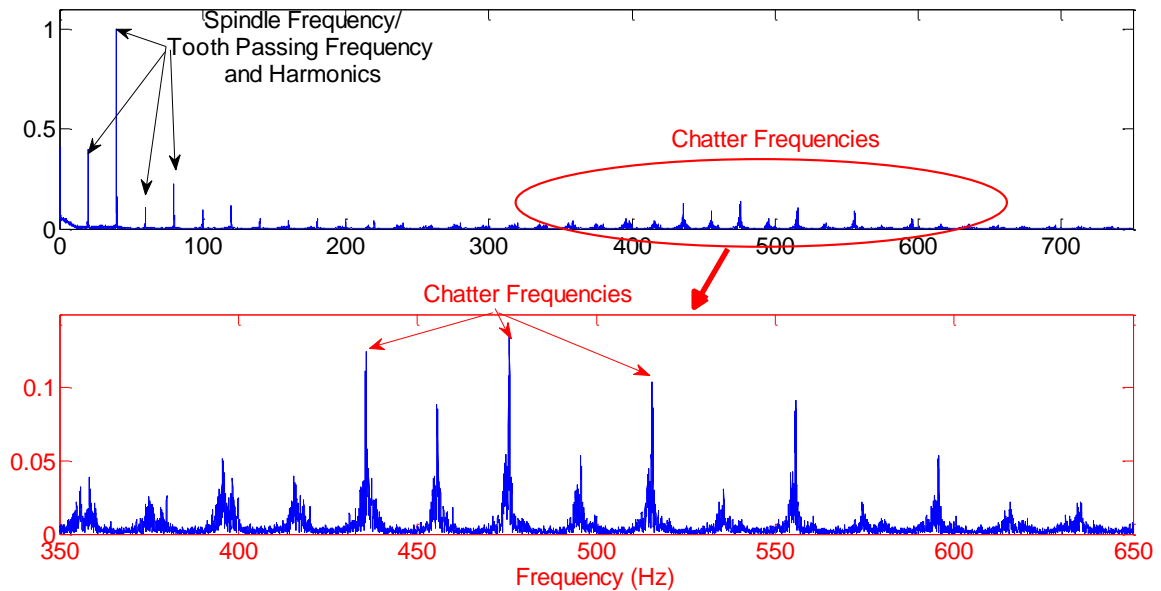


Figure. 76. Frequency decomposition of the PVDF sensor signal (Test 3).

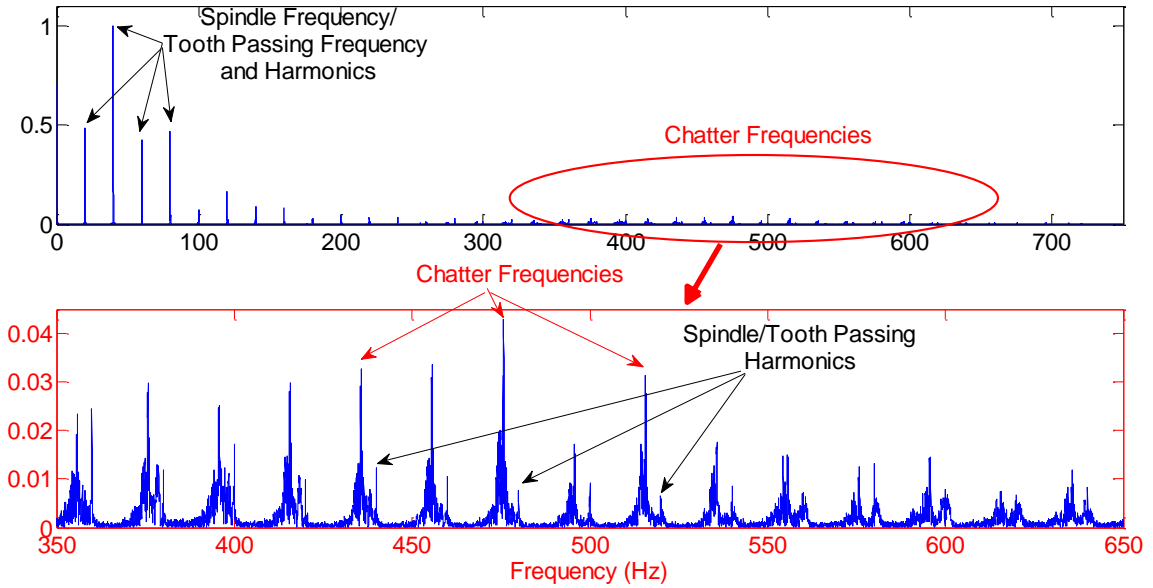


Figure. 77. Frequency decomposition of the dynamometer force signal (Test 3, the force in the X direction).

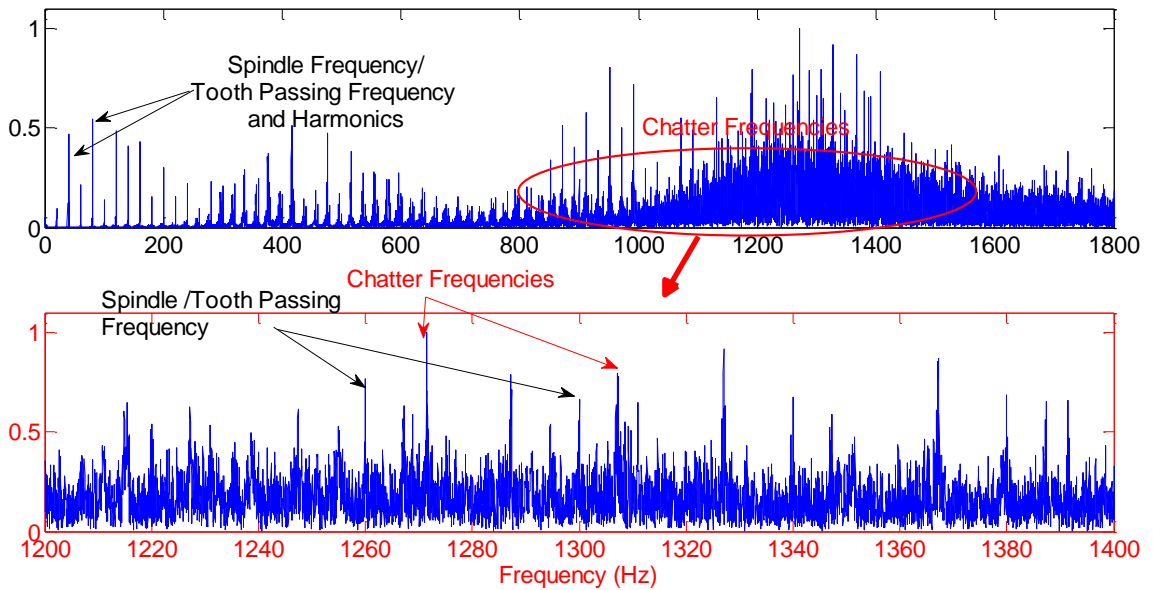


Figure. 78. Frequency decomposition of the accelerometer signal (Test 3, the acceleration in the X direction).

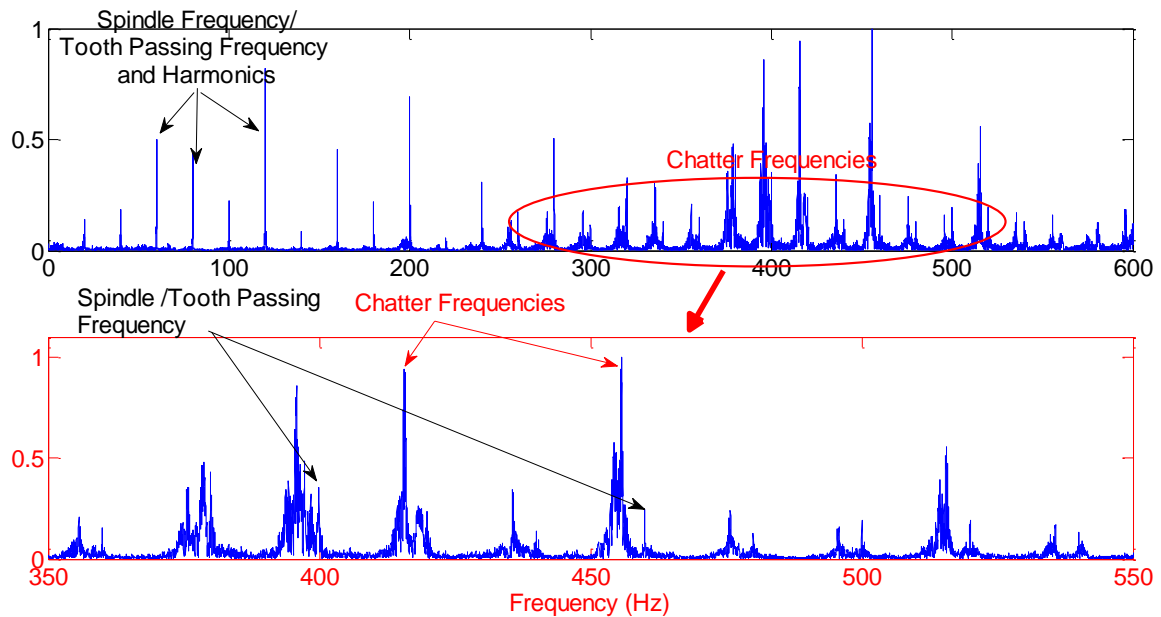


Figure. 79. Frequency decomposition of the microphone signal (Test 3).

Summarizing the aforementioned observations, the PVDF sensor and the dynamometer outperform the microphone and accelerometer in measuring the cutting resistance (i.e., cutting force, cutting torque) because the forced vibration caused by the cutting resistance is directly imprinted in the responses of these two sensors. The PVDF sensor can pick up the chatter frequencies better than the dynamometer, especially under low immersion cutting, largely because the PVDF sensor produces a larger response to the free vibrations due to the relatively low mechanical stiffness of the cutting tool. For monitoring applications, especially for chatter monitoring, the microphone and accelerometer demonstrate superior performance as measured by the normalized amplitude of the chatter frequency peaks. The microphone is probably preferred because of its flat frequency response and higher signal to noise ratio compared to the accelerometer.

Summary

A PVDF torque sensor was prototyped and experimentally validated. Reasonably good agreement was achieved between the reference cutting torque signal computed from the as-measured dynamometer force signals and the as-measured PVDF sensor signal. The agreement between the two signals can be further improved by adopting a more reliable cutting torque signal or by more precise positioning of the PVDF sensors on the host structure. In addition, the PVDF torque sensor is qualitatively compared with three popular sensors for chatter detection: piezoelectric dynamometer, accelerometer and acoustic microphone. Due to the spurious peaks seen in the PVDF sensor during chatter experiments, it could not be compared with the four sensors using the chatter detection algorithm developed in this work. Instead, all the sensors signals were compared using the traditional Fourier Transform. It is observed that for chatter monitoring applications, the microphone and the accelerometer outperform the dynamometer and the PVDF torque sensor in terms of the normalized amplitude of the chatter frequency peaks. However, it is also observed that both the PVDF torque sensor and the dynamometer can capture the periodic force vibration much better and, at the same time, the PVDF torque sensor can pick up the chatter frequencies slightly better than the dynamometer, especially in low radial immersion cutting.

CHAPTER 7 CONCLUSIONS AND RECOMMENDATIONS

This chapter summarizes the original contributions and main conclusions of this thesis and suggests possible areas for future studies.

Original Contributions

A set of innovative methods and algorithms for wireless monitoring of milling process has been presented in this thesis, including the PVDF sensor based measurement of in-plane cutting forces and cutting torque in milling process and a computationally efficient algorithm for on-line chatter detection and dominant chatter frequency estimation in milling. In addition, three novel PVDF rosettes and one general purpose PVDF rosette have been developed to maximize the sensitivity of the sensor to a particular strain component of interest and to minimize its sensitivity to noise and irrelevant strain components. The originality of this research lies in the design of the PVDF sensor rosettes, physics based modeling of the cutting forces/torque measurement system, the computationally efficient signal processing scheme used to isolate the chatter regeneration frequency content from the source signal, the cutting condition independent index for chatter detection and the complex exponentials model based time domain algorithm for dominant chatter frequency estimation. The proposed methods in this thesis represent lower cost alternatives to the current industry standard for cutting force/torque measurement, i.e., piezoelectric dynamometers.

Main Conclusions

The conclusions for each part of this research are summarized below.

PVDF sensor based in-plane cutting force measurement in milling

- PVDF sensor based in-plane cutting force measurement system was designed, analyzed, prototyped and experimentally validated for end milling. Very good agreement was achieved between the PVDF sensor signal and the piezoelectric dynamometer force signal.
- Quantitative, physics based models were established to relate the measured PVDF sensor signals to cutting forces. The model was shown to be independent of workpiece material and cutting conditions.
- A least squares FIR filter was shown to flatten the frequency response of the measurement system with reasonable success.

Generic PVDF sensor rosette design and validation

- PVDF sensor rosettes for measuring the bending strain, shear strain and axial strain have been designed and experimentally validated against their metal foil strain gauge counterparts, respectively. Very good agreement between the measurements from the PVDF sensor rosettes and those from the metal foil strain gauge rosettes has been achieved.
- Quantitative models for the PVDF sensor measurements were developed for the three proposed PVDF sensor rosettes. Thermal strains and the pyroelectric effect, which were not considered in prior work on PVDF sensor applications, were taken into account in the models.
- The PVDF sensor rosettes demonstrate a much higher signal to noise ratio than their metal foil strain gauge counterparts, which is expected because the

sensitivity of the PVDF sensor to strain is about three orders of magnitude higher.

Algorithms for chatter detection and chatter frequency estimation in milling

- The chatter detection method, which consists of a four-step signal processing scheme followed by a univariate control chart, is shown to be able to recognize chatter before chatter marks appear on the workpiece and is independent of cutting geometry variations, cutting conditions and tool/workpiece materials.
- The complex exponentials model based chatter frequency estimation algorithm is shown to capture the dominant chatter frequency with the same accuracy as the traditional Fourier Transform.
- Both the chatter detection and chatter frequency algorithms are computationally more efficient than traditional Fourier Transform. The computational cost of the chatter detection algorithm is linear with the size of the data, while the chatter frequency estimation algorithm can be 10 times faster than FFT with properly chosen parameters.

PVDF sensor based milling torque measurement and chatter detection

- The PVDF torque rosette was implemented on the cutting tool to measure the milling torque. Reasonable agreement between the PVDF sensor signal and a reference signal computed from the dynamometer force signals was achieved.
- The PVDF torque sensor was experimentally compared with three popular sensors for chatter detection: piezoelectric dynamometers, accelerometers and

acoustic microphones. It was observed that the PVDF torque sensor and piezoelectric dynamometers outperform the accelerometer and microphone in measurement applications, while the accelerometers and microphones demonstrate superior performance in chatter monitoring

- Compared with piezoelectric dynamometers, the PVDF torque sensor picks up the chatter vibration slightly better, largely because of the large response of the PVDF sensor to free vibrations of the slender cutting tool.

Future Work and Recommendations

All the methods and algorithms developed in this thesis can potentially be applied in shop floor applications or in the development of a new machining process without significantly increasing the production cost. These sensing technologies are especially useful when the machine tool structures involved are not sufficiently rigid. One application of special interest is robotic arm based milling or drilling process. A robotic arm features higher versatility, higher programmability and lower capital cost when compared to traditional machine tools. However, only limited mechanical stiffness is offered by the robot arm structure, leading to poor dimensional accuracy and repeatability during machining. High bandwidth feedback using the sensing technologies developed in this work may help the robotic arm achieve the desired accuracy and repeatability. The reliability and fault diagnosis of the cutting force/torque measurement system itself, especially the signal conditioning and radio frequency transmitting electronics, when rotating at high speed may also be an interesting topic.

To commercialize the methods introduced in this thesis, better packaging of the sensors and associated electronics is needed to protect the sensors and electronics from

coolant and chips. The establishment of the error maps of the PVDF sensor based measurement systems via extensive cutting experiments is also needed to better characterize the performance of the system under different cutting conditions. It is suggested that all the electronics be manufactured on flexible printed circuit boards so that they can be non-intrusively attached to the cutting tool-tool holder system. More precise positioning of individual PVDF sensors is necessary to fully take advantage of the benefits offered by the rosette design. Material property variations of the PVDF sensor can be minimized by implementing tighter statistical process control. Dynamic balancing of the measurement system is also critical, especially for high speed machining.

REFERENCES

- [1] Kline, W. A., Devor, R. E., and Shareef, I. A., 1982, "The Prediction of Surface Accuracy in End Milling," *Journal of Engineering for Industry*, 104(3), pp. 272-278.
- [2] Kline, W. A., Devor, R. E., and Lindberg, J. R., 1982, "The Prediction of Cutting Forces in End Milling with Application to Cornering Cuts," *International Journal of Machine Tool Design and Research*, 22(1), pp. 7-22.
- [3] Sutherland, J. W., and Babin, T. S., 1986, "An Improved Method for Cutting Force and Surface Error Prediction in Flexible End Milling Systems," *Journal of Engineering for Industry*, 108(4), pp. 269-279.
- [4] Kline, W. A., and Devor, R. E., 1983, "The Effect of Runout on Cutting Geometry and Forces in End Milling," *International Journal of Machine Tool Design and Research*, 23(2-3), pp. 123-140.
- [5] Insperger, T., Stépán, G., Bayly, P. V., and Mann, B. P., 2003, "Multiple Chatter Frequencies in Milling Processes," *Journal of Sound and Vibration*, 262(2), pp. 333-345.
- [6] Davies, M. A., Pratt, J. R., Dutterer, B., and Burns, T. J., 2002, "Stability Prediction for Low Radial Immersion Milling," *Journal of Manufacturing Science and Engineering*, 124(2), pp. 217-225.
- [7] Insperger, T., and Stepan, G., 2004, "Vibration Frequencies in High-Speed Milling Processes or a Positive Answer to Davies, Pratt, Dutterer and Burns," *Journal of Manufacturing Science and Engineering*, 126(3), pp. 481-487.
- [8] Altintas, Y., Stepan, G., Merdol, D., and Dombovari, Z., 2008, "Chatter Stability of Milling in Frequency and Discrete Time Domain," *CIRP Journal of Manufacturing Science and Technology*, 1(1), pp. 35-44.
- [9] Stepan, G., Dombovari, Z., and Muña, J., 2011, "Identification of Cutting Force Characteristics Based on Chatter Experiments," *CIRP Annals - Manufacturing Technology*, 60(1), pp. 113-116.

- [10] Lei, J., 1997, "Advances in Thin Film Sensor Technologies for Engine Applications," Technical Report No.
- [11] Meas, 2009, Sdt Shielded Piezo Sensors, March 15th, 2011, http://www.meas-spec.com/downloads/SDT_Series.pdf
- [12] Gu, H., Zhao, Y., and Wang, M. L., 2005, "A Wireless Smart PvdF Sensor for Structural Health Monitoring," *Structural Control and Health Monitoring*, 12(3), pp. 329-343.
- [13] Matsumoto, E., Biwa, S., Katsumi, K., Omoto, Y., Iguchi, K., and Shibata, T., 2004, "Surface Strain Sensing with Polymer Piezoelectric Film," *NDT&E International*, 37(1), pp. 57-64.
- [14] Liang, S. Y., Hecker, R. L., and Landers, R. G., 2004, "Machining Process Monitoring and Control: The State-of-the-Art," *Journal of Manufacturing Science and Engineering*, 126(2), pp. 297-310.
- [15] Byrne, G., Dornfeld, D., Inasaki, I., Ketteler, G., Koniq, W., and Teti, R., 1995, "Tool Condition Monitoring (Tcm) - the Status of Research and Industrial Application," *CIRP Annals - Manufacturing Technology*, 44(2), pp. 541-567.
- [16] Teti, R., Jemielniak, K., O'donnell, G., and Dornfeld, D., 2010, "Advanced Monitoring of Machining Operations," *CIRP Annals - Manufacturing Technology*, 59(2), pp. 717-739.
- [17] Bischoff, B., Ramalingam, S., and Robbins, W. P., 1987, "Toolbit Mounted Thin Film Zinc Oxide Sensors for Process Control in Lathe and Milling Machine Applications," eds., pp. 605-610.
- [18] Robbins, W. P., Bischoff, B., and Ramalingam, S., 1988, "Insert-Mounted Thin Film Sensors for Real-Time Monitoring of Tool Conditions," *Thin Solid Films*, 166(1), pp. 387-395.
- [19] Dornfeld, D. A., Lee, Y., and Chang, A., 2003, "Monitoring of Ultraprecision Machining Processes," *International Journal of Advanced Manufacturing Technology*, 21(8), pp. 571-578.

- [20] Yoshioka, H., Hashizume, H., and Shinno, H., 2004, "In-Process Microsensor for Ultraprecision Machining," IEE Proceedings: Science, Measurement and Technology, 151(2), pp. 121-125.
- [21] Choi, H., and Li, X., 2008, "Experimental Investigations of Laser Micromachining of Nickel Using Thin Film Micro Thermocouples," Journal of Manufacturing Science and Engineering, 130(2), pp. 021002-1-8.
- [22] Cheng, X., and Li, X., 2008, "Development of Metal Embedded Microsensors by Diffusion Bonding and Testing in Milling Process," Journal of Manufacturing Science and Engineering, 130(6), pp. 061010.
- [23] Wright, P. K., Dornfeld, D., Hillaire, R. G., and Ota, N. K., 2006, "A Wireless Sensor for Tool Temperature Measurement and Its Integration within a Manufacturing System," Transactions of NAMRI/SME, 34(1), pp. 63-70.
- [24] Wright, P. K., Dornfeld, D., and Ota, N., 2008, "Condition Monitoring in End-Milling Using Wireless Sensor Networks (Wsns)," Transactions of NAMRI/SME, 36(1), pp. 177-183.
- [25] Suprock, C. A., Hassan, R. Z., Jerard, R. B., and Fussell, B. K., 2008, "Predicting Endmill Tool Chatter with a Wireless Tool Tip Vibration Sensor," eds., Gaithersburg, MD, USA, pp. 1-13.
- [26] Suprock, C. A., Jerard, R. B., and Fussell, B. K., 2009, "In Situ Chatter Frequency Prediction Using Torque Data from a Wireless Sensor Integrated Tool Holder," eds., West Lafayette, IN, USA, pp. 84357.
- [27] Suprock, C. A., and Nichols, J. S., 2009, "A Low Cost Wireless High Bandwidth Transmitter for Sensor-Integrated Metal Cutting Tools and Process Monitoring," International Journal of Mechatronics and Manufacturing Systems, 2(4), pp. 441-454.
- [28] Jerard, R. B., Fussell, B. K., Suprock, C. A., Cui, Y., Nichols, J., Hassan, R. Z., and Esterling, D., 2009, "Integration of Wireless Sensors and Models for a Smart Machining System," eds., West Lafayette, Indiana, USA, pp. 84354.
- [29] Guha, A., Li, X., and Werschmoeller, D., 2010, "Wireless Acquisition of Temperature Data from Pcbn Embedded Thin-Film Sensors," eds., Erie, PA, USA, pp. 34177.

- [30] Werschmoeller, D., Ehmann, K., and Li, X., 2011, "Tool Embedded Thin Film Microsensors for Monitoring Thermal Phenomena at Tool-Workpiece Interface During Machining," *Journal of Manufacturing Science and Engineering*, 133(2), pp. 021007.
- [31] Zhang, Y., 2006, "In Situ Fatigue Crack Detection Using Piezoelectric Paint Sensor," *Journal of Intelligent Material Systems and Structures*, 17(10), pp. 843-852.
- [32] Samuel, P. D., and Pines, D. J., 1997, "Health Monitoring and Damage Detection of a Rotorcraft Planetary Geartrain System Using Piezoelectric Sensors," *Proc. SPIE* 3041, pp. 44-53.
- [33] Zhang, H., Galea, S. C., Chiu, W. K., and Lam, Y. C., 1993, "An Investigation of Thin PvdF Films as Fluctuating-Strain-Measuring and Damage-Monitoring Devices," *Smart Materials and Structures*, 2(4), pp. 208-216.
- [34] Sirohi, J., and Chopra, I., 2000, "Fundamental Understanding of Piezoelectric Strain Sensors," *Journal of Intelligent Material Systems and Structures*, 11(4), pp. 246-257.
- [35] Campbell, J. F., Vanderheiden, E. G., and I.A., M., 1992, "A Multi-Purpose Sensor for Composite Laminates Based on a Piezoelectric Film," *Journal of Composite Materials*, 26(3), pp. 334-349.
- [36] Ma, L., Melkote, S., Morehouse, J., Castle, J., and Fonda, J., 2010, "On-Line Monitoring of End Milling Forces Using a Thin Film Based Wireless Sensor Module," eds., Erie, PA, USA, pp. 34272.
- [37] Payo, I., and Haleb, J. M., 2010, "Dynamic Characterization of Piezoelectric Paint Sensors under Biaxial Strain," *Sensors and Actuators A: Physical*, 163(1), pp. 150-158.
- [38] Tlustý, J., and Andrews, G. C., 1983, "A Critical Review of Sensors for Unmanned Machining," *CIRP Annals - Manufacturing Technology*, 32(2), pp. 563-572.
- [39] Jun, M. B., Burak Ozdoganlar, O., Devor, R. E., Kapoor, S. G., Kirchheim, A., and Schaffner, G., 2002, "Evaluation of a Spindle-Based Force Sensor for Monitoring and Fault Diagnosis of Machining Operations," *International Journal of Machine Tools and Manufacture*, 42(6), pp. 741-751.

- [40] Park, S. S., and Altintas, Y., 2004, "Dynamic Compensation of Spindle Integrated Force Sensors with Kalman Filter," *Journal of Dynamic Systems, Measurement, and Control*, 126(3), pp. 443-452.
- [41] Albrecht, A., Park, S. S., Altintas, Y., and Pritschow, G., 2005, "High Frequency Bandwidth Cutting Force Measurement in Milling Using Capacitance Displacement Sensors," *International Journal of Machine Tools and Manufacture*, 45(9), pp. 993-1008.
- [42] Hoffmann, P., Scheer, C., Zurich, E., Kirchheim, A., and Shaffner, G., 1999, "Spindle-Integrated Force Sensors for Monitoring Drilling and Milling Processes," eds., Nurnberg, Germany, pp. 1-7.
- [43] Auchet, S., Chevrier, P., Lacour, M., and Lipinski, P., 2004, "A New Method of Cutting Force Measurement Based on Command Voltages of Active Electro-Magnetic Bearings," *International Journal of Machine Tools and Manufacture*, 44(14), pp. 1441-1449.
- [44] Jeong, Y.-H., and Cho, D.-W., 2002, "Estimating Cutting Force from Rotating and Stationary Feed Motor Currents on a Milling Machine," *International Journal of Machine Tools and Manufacture*, 42(14), pp. 1559-1566.
- [45] Spiewak, S. A., 1995, "Acceleration Based Indirect Force Measurement in Metal Cutting Processes," *International Journal of Machine Tools and Manufacture*, 35(1), pp. 1-17.
- [46] Yaldiz, S., Ünsaçar, F., Saglam, H., and Isik, H., 2007, "Design, Development and Testing of a Four-Component Milling Dynamometer for the Measurement of Cutting Force and Torque," *Mechanical Systems and Signal Processing*, 21(3), pp. 1499-1511.
- [47] Totis, G., Wirtz, G., Sortino, M., Veselovac, D., Kuljanic, E., and Klocke, F., 2010, "Development of a Dynamometer for Measuring Individual Cutting Edge Forces in Face Milling," *Mechanical Systems and Signal Processing*, 24(6), pp. 1844-1857.
- [48] Smith, D. A., Smith, S., and Tlustý, J., 1998, "High Performance Milling Torque Sensor," *Journal of Manufacturing Science and Engineering*, 120(2), pp. 504-514.

- [49] Kuljanic, E., Sortino, M., and Totis, G., 2008, "Multisensor Approaches for Chatter Detection in Milling," *Journal of Sound and Vibration*, 312(4-5), pp. 672-693.
- [50] Al-Regib, E., and Ni, J., 2010, "Chatter Detection in Machining Using Nonlinear Energy Operator," *Journal of Dynamic Systems, Measurement, and Control*, 132(3), pp. 0345021 - 0345024.
- [51] Berger, B., Belai, C., and Anand, D., 2003, "Chatter Identification with Mutual Information," *Journal of Sound and Vibration*, 267(1), pp. 178-186.
- [52] Berger, B. S., Manzari, J. A., Anand, D. K., and Belai, C., 2001, "Auto-Regressive Svd Algorithms and Cutting State Identification," *Journal of Sound and Vibration*, 248(2), pp. 351-370.
- [53] Berger, B. S., Minis, I., Harley, J., Rokni, M., and Papadopoulos, M., 1998, "Wavelet Based Cutting State Identification," *Journal of Sound and Vibration*, 213(5), pp. 813-827.
- [54] Berger, B. S., Minis, I., Rokni, M., Papadopoulos, M., Deng, K., and Chavalli, A., 1997, "Cutting State Identification," *Journal of Sound and Vibration*, 200(1), pp. 15-29.
- [55] Cho, D. W., and Eman, K. F., 1988, "Pattern Recognition for on-Line Chatter Detection," *Mechanical Systems and Signal Processing*, 2(3), pp. 279-290.
- [56] Li, X. Q., Wong, Y. S., and Nee, A. Y. C., 1997, "Tool Wear and Chatter Detection Using the Coherence Function of Two Crossed Accelerations," *International Journal of Machine Tools and Manufacture*, 37(4), pp. 425-435.
- [57] Wang, L., and Liang, M., 2009, "Chatter Detection Based on Probability Distribution of Wavelet Modulus Maxima," *Robotics and Computer-Integrated Manufacturing*, 25(6), pp. 989-998.
- [58] Yao, Z., Mei, D., and Chen, Z., 2010, "On-Line Chatter Detection and Identification Based on Wavelet and Support Vector Machine," *Journal of Materials Processing Technology*, 201(5), pp. 713-719.
- [59] Dijk, N. J. M. V., Doppenberg, E. J. J., Faassen, R. P. H., Wouw, N. V. D., Oosterling, J. a. J., and H.Nijimeijer, 2010, "Automatic in-Process Chatter

Avoidance in the High-Speed Milling Process," *Journal of Dynamic Systems, Measurement, and Control*, 132(3), pp. 03100601-03100614.

- [60] Dong, W., Joe Au, Y. H., and Mardapittas, A., 1992, "Machine Tool Chatter Monitoring by Coherence Analysis," *International Journal of Production Research*, 30(8), pp. 1901.
- [61] Higuchi, M., and Doi, M., 1986, "A Study on the Estimation of the Chatter Commencing in Turning Process," *Journal of the Japan Society of Precision Engineering (in Japanese)*, 50(7), pp. 1697.
- [62] Gu, S., Ni, J., and Yuan, J., 2002, "Non-Stationary Signal Analysis and Transient Machining Process Condition Monitoring," *International Journal of Machine Tools and Manufacture*, 42(1), pp. 41-51.
- [63] Li, X. Q., Wong, Y. S., and Nee, A. Y. C., 1998, "A Comprehensive Identification of Tool Failure and Chatter Using a Parallel Multi-Art2 Neural Network," *Journal of Manufacturing Science and Engineering*, 120(2), pp. 433-442.
- [64] Tansel, I. N., Wang, X., Chen, P., Yenilmez, A., and Ozcelik, B., 2006, "Transformations in Machining. Part 2. Evaluation of Machining Quality and Detection of Chatter in Turning by Using S-Transformation," *International Journal of Machine Tools and Manufacture*, 46(1), pp. 43-50.
- [65] Braun, S., 1975, "Signal Processing for the Determination of Chatter Threshold," *CIRP Annals - Manufacturing Technology*, 24(1), pp. 315-320.
- [66] Jiang, Y. T., and Zhang, C. L., 2006, "Hybrid Hmm/Svm Method for Predicting of Cutting Chatter," *Proceedings of SPIE--the international society for optical engineering*, 6280, pp. Q1 - Q8.
- [67] Eman, K., and Wu, S. M., 1980, "A Feasibility Study of on-Line Identification of Chatter in Turning Operations," *Journal of Engineering for Industry*, 102(4), pp. 315-321.
- [68] Faassen, R., Doppenberg, E. J. J., Wouw, N. V. D., Oosterling, J. a. J., and Nijmeijer, H., 2006, "Online Detection of the Onset and Occurrence of Machine Tool Chatter in the Milling Process," eds., Vancouver, Canada, pp.

- [69] Wang, M., and Fei, R., 2001, "On-Line Chatter Detection and Control in Boring Based on an Electrorheological Fluid," *Mechatronics*, 11(7), pp. 779-792.
- [70] Du, R., Elbestawi, M. A., and Ullagaddi, B. C., 1992, "Chatter Detection in Milling Based on the Probability Distribution of Cutting Force Signal," *Mechanical Systems and Signal Processing*, 6(4), pp. 345-362.
- [71] Matsubara, T., and Yamamoto, H., 1984, "Study on Regenerative Chatter Vibration with Dynamic Cutting Force," *Journal of the Japan Society of Precision Engineering (in Japanese)*, 50(7), pp. 1079.
- [72] Mitsubishi, M., Nagao, T., Hatamura, Y., and Warisawa, S., 1992, "Real-Time Machining State Detection Using Multiaxis Force Sensing," *CIRP Annals - Manufacturing Technology*, 41(1), pp. 505-508.
- [73] Tarng, Y. S., and Li, T. C., 1994, "The Change of Spindle Speed for the Avoidance of Chatter in End Milling," *Journal of Materials Processing Technology*, 41(2), pp. 227-236.
- [74] Yoon, M. C., and Chin, D. H., 2005, "Cutting Force Monitoring in the Endmilling Operation for Chatter Detection," *Proceedings of the Institution of Mechanical Engineers, Part B: Journal of Engineering Manufacture*, 219(6), pp. 455-465.
- [75] Grabec, I., Gradisek, J., and Govekar, E., 1999, "A New Method for Chatter Detection in Turning," *CIRP Annals - Manufacturing Technology*, 48(1), pp. 29-32.
- [76] Gradisek, J., Govekar, E., and Grabec, I., 1998, "Time Series Analysis in Metal Cutting Chatter Versus Chatter-Free Cutting," *Mechanical Systems and Signal Processing*, 12(6), pp. 839-854.
- [77] Choi, T., and Shin, Y. C., 2003, "On-Line Chatter Detection Using Wavelet-Based Parameter Estimation," *Journal of Manufacturing Science and Engineering*, 125(1), pp. 21-28.
- [78] Bao, S., Zhang, W., Yu, J., Qiao, S., and Yang, F., 1994, "A New Approach to the Early Prediction of Turning Chatter," *Journal of Vibration and Acoustics*, 116(4), pp. 485-488.

- [79] Bickraj, K., Kaya, B., Yapici, A., Li, M., Tansel, I. N., and Ozcelik, B., 2007, "Inspection of Chatter Damage in End Milling Operations by Using Wavelet Transformations," eds., Tampico, México, pp.
- [80] Chen, Y., Li, X., and Orady, E., 1996, "Chatter Detection in Milling Process Via Time-Frequency Distributions," eds., Minneapolis, MN, 1, pp. 59-64.
- [81] Ota, H., and Kawai, T., 1991, "Monitoring of Cutting Conditions by Means of Vibration Analysis " Transactions of Japan Society of Mechanical Engineering (in Japanese), 57(540), pp. 2752.
- [82] Pongsathornwiwat, N., and Tangjitsitcharoen, S., 2010, "Intelligent Monitoring and Detection of Chatter in Ball-End Milling Process on Cnc Machining Center " eds., pp. 1-6.
- [83] Tangjitsitcharoen, S., 2009, "In-Process Monitoring and Detection of Chip Formation and Chatter for Cnc Turning," Journal of Materials Processing Technology, 209(10), pp. 4682-4688.
- [84] Altintas, Y., and Chan, P. K., 1992, "In-Process Detection and Suppression of Chatter in Milling," International Journal of Machine Tools and Manufacture, 32(3), pp. 329-347.
- [85] Tarng, Y. S., Li, T. C., and Chen, M. C., 1994, "On-Line Drilling Chatter Recognition and Avoidance Using an Artificial Neural Network," International Journal of Machine Tools and Manufacture, 34(7), pp. 949-957.
- [86] Govekar, E., Gradisek, J., and Grabec, I., 2000, "Analysis of Acoustic Emission Signals and Monitoring of Machining Processes," Ultrasonics, 38(1-8), pp. 598-603.
- [87] Tarng, Y. S., and Li, T. C., 1995, "Adaptive Pattern Recognition of Drilling Chatter," Journal of Materials Processing Technology, 48(1-4), pp. 247-253.
- [88] Ding, S., Izamshah, R. a. R., Mo, J., and Zhu, Y., 2011, "Chatter Detection in High Speed Machining of Titanium Alloys," Key Engineering Materials, 458(1), pp. 289-294.

- [89] Delio, T., Tlustý, J., and Smith, S., 1992, "Use of Audio Signals for Chatter Detection and Control," *Journal of Engineering for Industry*, 114(2), pp. 146-157.
- [90] Nair, U., Krishna, B. M., and Namboothiri, V. N. N., 2010, "Permutation Entropy Based Real-Time Chatter Detection Using Audio Signal in Turning Process," *International Journal of Advanced Manufacturing Technology*, 46(1), pp. 61-68.
- [91] Bediaga, I., Muñoa, J., Hernández, J., and López De Lacalle, L. N., 2009, "An Automatic Spindle Speed Selection Strategy to Obtain Stability in High-Speed Milling," *International Journal of Machine Tools and Manufacture*, 49(5), pp. 384-394.
- [92] Smith, S., and Delio, T., 1992, "Sensor-Based Chatter Detection and Avoidance by Spindle Speed Selection," *Journal of Dynamic Systems, Measurement, and Control*, 114(1), pp. 486-492.
- [93] Smith, S., and Tlustý, J., 1992, "Stabilizing Chatter by Automatic Spindle Speed Regulation," *CIRP Annals - Manufacturing Technology*, 41(1), pp. 433-436.
- [94] Schmitz, T. L., 2003, "Chatter Recognition by a Statistical Evaluation of the Synchronously Sampled Audio Signal," *Journal of Sound and Vibration*, 262(3), pp. 721-730.
- [95] Tansel, I. N., Li, M., Demetgul, M., and Bickraj, K., 2010, "Detecting Chatter and Estimating Wear from the Torque of End Milling Signals by Using Index Based Reasoner (Ibr)," *International Journal of Advanced Manufacturing Technology*, pp. 1-10.
- [96] Messaoud, A., Weihs, C., and Hering, F., 2007, "Detection of Chatter Vibration in a Drilling Process Using Multivariate Control Charts," *Computational Statistics & Data Analysis*, 52(6), pp. 3208-3219.
- [97] Messaoud, A., and Weihs, C., 2009, "Monitoring a Deep Hole Drilling Process by Nonlinear Time Series Modeling," *Journal of Sound and Vibration*, 321(3-5), pp. 620-630.
- [98] Weck, M., Verhaag, E., and Gathier, M., 1975, "Adaptive Control for Face Milling Operations with Strategies for Avoiding Chatter Vibrations and Automatic Cut Distribution," *CIRP Annals - Manufacturing Technology*, 24(1), pp. 405-409.

- [99] González-Brambila, O., Rubio, E., Jáuregui, J. C., and Herrera-Ruiz, G., 2006, "Chattering Detection in Cylindrical Grinding Processes Using the Wavelet Transform," *International Journal of Machine Tools and Manufacture*, 46(15), pp. 1934-1938.
- [100] Kwak, J.-S., and Song, J.-B., 2001, "Trouble Diagnosis of the Grinding Process by Using Acoustic Emission Signals," *International Journal of Machine Tools and Manufacture*, 41(6), pp. 899-913.
- [101] Griffin, J. M., and Chen, X., 2009, "Multiple Classification of the Acoustic Emission Signals Extracted During Burn and Chatter Anomalies Using Genetic Programming," *International Journal of Advanced Manufacturing Technology*, 45(11), pp. 1152-1168.
- [102] Kwak, J. S., and Ha, M. K., 2004, "Intelligent Diagnostic Technique of Machining State for Grinding," *The International Journal of Advanced Manufacturing Technology*, 23(5), pp. 436-443.
- [103] Abu-Zahra, N. H., and Lange, J. H., 2002, "Tool Chatter Monitoring in Turning Operations Using Wavelet Analysis of Ultrasound Waves," *International Journal of Advanced Manufacturing Technology*, 20(4), pp. 248-254.
- [104] Soliman, E., and Ismail, F., 1997, "Chatter Detection by Monitoring Spindle Drive Current," *International Journal of Advanced Manufacturing Technology*, 13(1), pp. 27-34.
- [105] Kondo, E., Ota, H., and Kawai, T., 1997, "A New Method to Detect Regenerative Chatter Using Spectral Analysis, Part 1: Basic Study on Criteria for Detection of Chatter," *Journal of Manufacturing Science and Engineering*, 119(4a), pp. 461-466.
- [106] Khalifa, O. O., and Densibali, A., 2006, "Image Processing for Chatter Identification in Machining Processes," *International Journal of Advanced Manufacturing Technology*, 31(5), pp. 443-449.
- [107] Tlustý, J., and Ismail, F., 1983, "Special Aspects of Chatter in Milling," *Journal of Vibration, Acoustics, Stress and Reliability in Design*, 105(1), pp. 24-32.
- [108] Rahman, M., 1988, "In-Process Detection of Chatter Threshold," *Journal of Engineering for Industry*, 110(1), pp. 44-50.

- [109] Kuljanic, E., Totis, G., and Sortino, M., 2009, "Development of an Intelligent Multisensor Chatter Detection System in Milling," *Mechanical Systems and Signal Processing*, 23(5), pp. 1704-1718.
- [110] Tansel, I. N., Wagiman, A., and Tziranis, A., 1991, "Recognition of Chatter with Neural Networks," *International Journal of Machine Tools and Manufacture*, 31(4), pp. 539-552.
- [111] Mei, D. Q., Li, X., and Chen, Z. C., 2007, "Prediction of Cutting Chatter Based on Hidden Markov Model," *Key Engineering Materials*, 353-358(1), pp. 2712-2715.
- [112] Oppenheim, A. V., Schafer, R. W., and Buck, J. R., 1999, *Discrete-Time Signal Processing*, *Discrete-Time Signal Processing*, Prentice Hall, Upper Saddle River, NJ.
- [113] Ma, L., Melkote, S., Morehouse, J., Castle, J., Fonda, J., and Johnson, M., 2012, "Thin-Film PvdF Sensor Based Monitoring of Cutting Forces in Peripheral End Milling," *Journal of Dynamic Systems, Measurement and Control*, 134(5), pp. 051014.
- [114] 2001, Frequency Response Function Measurements, March 15th, 2011, http://www.sdrl.uc.edu/academic-course-info/docs/ucme663/v3_5.pdf
- [115] Gagnol, V., Bouzgarrou, B. C., Ray, P., and Barra, C., 2007, "Model-Based Chatter Stability Prediction for High-Speed Spindles," *International Journal of Machine Tools and Manufacture*, 47(7-8), pp. 1176-1186.
- [116] Bending Frequencies of Beams, Rods and Pipes, 2/3, <http://www.vibrationdata.com/tutorials2/beam.pdf>
- [117] 1988, "Ieee Standard on Piezoelectricity," ANSI/IEEE Std 176-1987, pp. 0_1.
- [118] Material: Tungsten Carbide (Wc), Bulk, February 2nd, www.memsnets.org/material/tungstencarbidewcbulk/
- [119] 2005, PvdF (Kynar) Detailed Properties, Jan 22nd, 2010, <http://www.texcal.us/coaxialwire/pvdfproperties.html>

- [120] Karki, J., 2000, Signal Conditioning Piezoelectric Sensors, 3/15/2010, <http://focus.ti.com/lit/an/sloa033a/sloa033a.pdf>
- [121] Hayes, M. H., 1996, *Statistical Digital Signal Processing and Modeling*, John Wiley & Sons,
- [122] Ma, L., Melkote, S., Morehouse, J., Castle, J., Fonda, J., and Johnson, M., 2012, "Design of Thin-Film PvdF Sensor Rosettes for Isolation of Various Strain Components," *Journal of Intelligent Material Systems and Structures*, 23(9), pp. 1119-1130.
- [123] Nye, J. F., 1979, *Physical Properties of Crystals : Their Representation by Tensors and Matrices* Clarendon Press, Oxford.
- [124] Karki, J., 2000, Signal Conditioning Piezoelectric Sensors, 3/15, <http://focus.ti.com/lit/an/sloa033a/sloa033a.pdf>
- [125] Doebelin, E. O., 1990, *Measurement Systems: Application and Design*, McGraw-Hill, New York.
- [126] Potma, T., 1967, *Strain Gauges: Theory and Application*, Centrex, Eindhoven.
- [127] Altintas, Y., 1988, "In-Process Detection of Tool Breakages Using Time Series Monitoring of Cutting Forces," *International Journal of Machine Tools and Manufacture*, 28(2), pp. 157-172.
- [128] Sabberwal, A. J. P., and Koenigsberger, F., 1961, "Chip Section and Cutting Force During the Milling Operation," *Annals of the CIRP*, 10(1), pp.
- [129] Altintas, Y., 2000, *Manufacturing Automation*, Cambridge University Press,
- [130] Moon, T. K., and Stirling, W. C., 2000, *Mathematical Methods and Algorithms for Signal Processing*, Prentice Hall, Upper Saddle River, N.J.
- [131] Kumaresan, R., and Tufts, D. W., 1983, "Estimating the Angles of Arrival of Multiple Plane Waves," *IEEE Transactions on Aerospace and Electrical Systems*, AES-19(1), pp. 134-139.

- [132] Wang, J.-J. J., and Liang, S. Y., 1996, "Chip Load Kinematics in Milling with Radial Cutter Runout," *Journal of Engineering for Industry*, 118(1), pp. 111-116.
- [133] 2006, BL-21994-000, 08/01/2012, http://www.knowles.com/search/prods_pdf/BL-21994-000.pdf